Sapienza
Università di Roma

Nonlinear geometric control of partially-coupled underactuated floating vehicles

Department of Computer, Control and Management Engineering "Antonio Ruberti"
Master of Science in Control Engineering

Simone Orelli
ID number 1749732

Advisor
Prof. Antonio Franchi

External advisor
Mirko Mizzoni, MSc

Academic Year 2024/2025

Thesis defended on 18 July 2025
in front of a Board of Examiners composed by:

Prof. Alessandro De Luca (chairman)
Prof. Andrea Cristofaro
Prof. Leonardo Lanari
Prof. Domenico Lembo
Prof. Francesco Liberati
Prof. Mattia Mattioni
Prof. Marilena Vendittelli

Nonlinear geometric control of partially-coupled underactuated floating vehicles
Master's Thesis. Sapienza University of Rome

This thesis has been typeset by LaTeX and the Sapthesis class.

Author's email: simoneorelli@icloud.com

To my beloved
grandparents.

Abstract

This thesis investigates the problem of achieving static hovering for generically tilted multirotor platforms (GTMs), with particular attention to partially coupled underactuated vehicles. Static hovering—the ability to maintain a fixed position and orientation—is essential for safe aerial operations, especially under reduced control authority, such as in the event of rotor failures. Starting from an existing dynamic model for GTMs defined on the configuration space $\mathbf{SE}(3)$—which accommodates arbitrary propeller positions and tilt angles—this work analyzes the stability of the closed-loop error dynamics resulting from a geometric control law originally proposed by Michieletto et al. The adopted control law enables static hovering for all platforms described by the considered model that are statically hoverable, with a focus on the challenging case of partially coupled underactuated vehicles. The main contribution of this work is a rigorous Lyapunov-based proof of local exponential stability for the closed-loop error dynamics under the geometric controller. While previous work provided experimental validation, a formal stability proof was missing. The analysis involves tools from nonlinear control theory and differential geometry, offering a unified, coordinate-free framework. Theoretical findings are supported by high-fidelity simulations, which confirm the predicted stability and robustness.

Ringraziamenti

Arrivati a questo punto, desidero esprimere la mia sincera gratitudine a tutti coloro che hanno reso possibile la realizzazione di questa tesi, che rappresenta il culmine di un percorso di studi impegnativo e, al tempo stesso, entusiasmante.

In primo luogo, il mio sentito ringraziamento va al Professor Antonio Franchi, relatore di questo lavoro, per la sua guida e il suo supporto costante durante tutto il processo di ricerca. La sua esperienza e i suoi preziosi consigli hanno avuto un impatto significativo sul mio lavoro e mi hanno aiutato a superare le sfide che ho incontrato lungo il cammino. Un ringraziamento altrettanto speciale va al mio relatore esterno, Mirko Mizzoni, per la sua disponibilità e il suo supporto durante la stesura di questa tesi. La sua pazienza e la sua esperienza hanno contribuito in modo significativo alla qualità del mio lavoro.

Il mio pensiero più affettuoso va ai miei nonni, a cui questa tesi è dedicata. Durante la stesura di questo lavoro, la loro presenza è stata per me una fonte costante di ispirazione e conforto. Ringrazio mia nonna Laura, che ha sempre creduto nelle mie capacità, e mio nonno Ernesto, la cui stima e fiducia mi hanno motivato a dare il meglio di me. Sento la loro presenza ogni giorno sempre più preziosa e delicata, e con questa dedica desidero lasciare un segno tangibile dell'affetto e della gratitudine che provo per loro, affinché possano sentirsi sempre parte del mio percorso, oggi come in futuro.

Un ringraziamento speciale va ai miei genitori, senza i quali non avrei potuto raggiungere questo traguardo. Hanno sempre creduto in me e mi hanno sostenuto in ogni passo del mio percorso accademico. Un ringraziamento particolare va a mia madre, che anche nel silenzio e nella discrezione c'è sempre stata, senza chiedere nulla in cambio. A lei devo ogni traguardo che ho raggiunto. Un ringraziamento va poi a mio padre, che mi ha sempre incoraggiato a dare il massimo e a perseguire i miei sogni.

Un sentito ringraziamento va a mia sorella Elisa, complice di vita, che ha condiviso con me momenti di gioia e di difficoltà, e che mi ha sempre sostenuto con il suo affetto e la sua comprensione. La sua presenza mi ha sempre rasserenato, convinto che insieme possiamo affrontare qualsiasi sfida. A lei devo molto più di quanto le parole possano esprimere.

Vorrei poi ringraziare di cuore Anastasia, con cui ho condiviso attimi di emozioni, lacrime e risate. Il mio percorso accademico è diventato anche un po' il suo, intrecciandosi tra ansie e soddisfazioni vissute insieme. A lei va la mia più sincera gratitudine e l'augurio che la vita possa restituirle tutto il bene che mi ha donato. Possa il suo cammino essere sempre colmo di successi, gioia e serenità, come quelli che abbiamo saputo regalarci a vicenda.

Desidero successivamente ringraziare mia cugina Laura, che ho sempre sentito come una sorella più che una semplice cugina. Abbiamo iniziato l'università insieme e fin dal primo giorno è stata una presenza capace di comprendermi davvero, di accogliere le mie paure come le mie gioie, condividendo ogni momento di questo percorso. Con tutto il cuore le auguro di realizzare ogni suo sogno, uno dopo l'altro.

Un pensiero di profonda gratitudine va a tutti i miei amici Alessandro, Antonio, Cristian, Francesco (Buzza), Matteo, Michele e Stefano, con cui ho condiviso momenti

indimenticabili, risate sincere e giornate che hanno reso questo percorso unico e irripetibile. La forza del nostro legame è stata per me un porto sicuro, capace di donarmi leggerezza e serenità anche nei momenti più difficili. Spero che la nostra amicizia continui a crescere e ad accompagnarci ancora a lungo, ovunque la vita ci porti.

Una menzione d'onore va a Michele, una presenza solida e rassicurante, che anche nei suoi periodi più avversi non ha mai fatto mancare il suo ascolto e i suoi preziosi consigli. La sua capacità di esserci, con discrezione e profondità, ha rappresentato per me un punto di riferimento costante, e di questo gli sarò sempre grato.

Voglio poi ringraziare di cuore Alessandra, Angelica e Florinda, amiche della triennale con le quali ho condiviso ogni passo di quel percorso. Nonostante le distanze e le strade diverse che la vita ci ha fatto intraprendere, il nostro legame è rimasto saldo e autentico. Spero che possa continuare a resistere, forte com'è, nel tempo e nello spazio.

Una menzione speciale va ad Angelica, che durante gli anni della triennale è stata per me una presenza fondamentale. Il suo sostegno e la sua capacità di comprendermi davvero hanno reso ogni difficoltà più leggera e ogni gioia più intensa. Anche ora che la distanza ci separa, il nostro rapporto è rimasto solido e profondo, segno di un legame indissolubile.

Desidero poi ringraziare con tutto il cuore il gruppo "Cueli della menza" e in generale i miei amici della magistrale. Un grazie sincero ad Antonio De Lucia, Antonio Rapuano, Dumitru, Edoardo, Francesca, Francesco (Ciccio), Giulia, Greta, Karim, Lorenzo, Mert e a tutti gli altri che ho avuto la fortuna di incontrare lungo questo cammino. La vostra presenza ha reso questo percorso meno tortuoso e infinitamente più ricco di gioia, risate e momenti indimenticabili. Senza di voi, ogni traguardo avrebbe avuto un sapore diverso, meno intenso e meno vero.

Una menzione speciale va ad Antonio, che è stato per me un fratello con cui ho condiviso ogni tappa di questo viaggio, dal primo esame fino alla proclamazione. Insieme abbiamo affrontato dubbi, difficoltà e incertezze, sostenendoci a vicenda e trovando sempre la forza di andare avanti. La sua presenza costante e il suo sostegno sono stati per me un punto di riferimento imprescindibile, e di questo gli sarò sempre grato.

Un ringraziamento altrettanto speciale va a Greta, che durante la stesura della tesi mi è rimasta accanto con una pazienza fuori dal comune. Nei momenti di sconforto, la sua vicinanza mi ha dato la forza di superare ogni ostacolo, ricordandomi l'importanza di avere accanto persone che credono in te anche quando tu stesso vacilli.

Un sentito ringraziamento a tutto il gruppo Sapienza Flight Team, un'esperienza preziosa che mi ha arricchito sia dal punto di vista umano che professionale e che porterò sempre con me.

Oggi concludo un capitolo importante della mia vita. A ognuno di voi devo un pezzo di questo traguardo, convinto che più del risultato conta chi c'è stato accanto per raggiungerlo.

Acknowledgments

At this point, I would like to express my sincere gratitude to all those who made this thesis possible, which represents the culmination of a challenging and, at the same time, exciting academic journey.

First of all, my heartfelt thanks go to Professor Antonio Franchi, supervisor of this work, for his guidance and constant support throughout the entire research process. His experience and valuable advice have had a significant impact on my work and helped me overcome the challenges I encountered along the way. An equally special thank you goes to my external advisor, Mirko Mizzoni, for his availability and support during the writing of this thesis. His patience and expertise have contributed significantly to the quality of my work.

My warmest thoughts go to my grandparents, to whom this thesis is dedicated. During the writing of this work, their presence has been a constant source of inspiration and comfort. I thank my grandmother Laura, who has always believed in my abilities, and my grandfather Ernesto, whose esteem and trust have motivated me to give my best. I feel their presence every day, increasingly precious and gentle, and with this dedication I wish to leave a tangible sign of the affection and gratitude I feel for them, so that they may always feel part of my journey, today and in the future.

A special thank you goes to my parents, without whom I could not have reached this milestone. They have always believed in me and supported me at every step of my academic journey. A particular thank you goes to my mother, who has always been there for me, even in silence and discretion, never asking for anything in return. I owe every achievement I have reached to her. My thanks also go to my father, who has always encouraged me to give my best and to pursue my dreams.

A heartfelt thank you goes to my sister Elisa, my partner in crime, who has shared moments of joy and difficulty with me, and who has always supported me with her affection and understanding. Her presence has always reassured me, convincing me that together we can face any challenge. I owe her more than words can express.

I would also like to express my heartfelt thanks to Anastasia, with whom I shared moments of emotion, tears and laughter. My academic journey has also become a little bit hers, intertwined with the anxieties and satisfactions we have experienced together. I offer her my sincere gratitude and hope that life will give her back all the good she has given me. May her path always be filled with success, joy and serenity, just as we have been able to give each other.

I would like to thank my cousin Laura, whom I have always felt more like a sister than just a cousin. We started university together and from the very first day she has been someone who truly understands me, welcoming my fears as well as my joys, sharing every moment of this journey. With all my heart, I wish her to fulfill every one of her dreams, one after another.

A thought of deep gratitude goes to all my friends Alessandro, Antonio, Cristian, Francesco (Buzza), Matteo, Michele, and Stefano, with whom I have shared unforgettable moments, sincere laughter, and days that have made this journey unique and unrepeatable. The strength of our bond has been a safe harbor for me, able to give me lightness and serenity even in the most difficult moments. I hope our friendship continues to grow and accompany us for a long time, wherever life takes us.

An honorable mention goes to Michele, my soul mate, a solid and reassuring presence, who even in his most difficult times has never failed to listen and give precious advice. His ability to be there, with discretion and depth, has been a constant point of reference for me, and for this I will always be grateful to him.

I would also like to sincerely thank Alessandra, Angelica, and Florinda, friends from my bachelor's degree with whom I shared every step of that journey. Despite the distances and the different paths life has taken us on, our bond has remained strong and authentic. I hope it can continue to endure, as strong as it is, over time and space.

A special mention goes to Angelica, who during the years of my bachelor's degree was a fundamental presence for me. Her support and her ability to truly understand me made every difficulty lighter and every joy more intense. Even now that distance separates us, our relationship has remained solid and deep, a sign of an unbreakable bond.

I would also like to thank with all my heart the group "Cueli della menza" and, in general, my friends from my master's degree. A sincere thank you to Antonio De Lucia, Antonio Rapuano, Dumitru, Edoardo, Francesca, Francesco (Ciccio), Giulia, Greta, Karim, Lorenzo, Mert, and all the others I have been lucky enough to meet along this journey. Your presence has made this path less tortuous and infinitely richer in joy, laughter, and unforgettable moments. Without you, every achievement would have had a different, less intense, and less true flavor.

A special mention goes to Antonio, who has been like a brother to me, with whom I have shared every stage of this journey, from the first exam to graduation. Together we have faced doubts, difficulties, and uncertainties, supporting each other and always finding the strength to move forward. His constant presence and support have been an essential point of reference for me, and for this I will always be grateful to him.

An equally special thank you goes to Greta, who stayed by my side with extraordinary patience during the writing of the thesis. In moments of discouragement, her closeness gave me the strength to overcome every obstacle, reminding me of the importance of having people by your side who believe in you even when you doubt yourself. I owe her much more than words can express.

A heartfelt thank you to the Sapienza Flight Team for the collaboration, a valuable experience that has enriched me both personally and professionally and that I will always carry with me.

Today I am closing an important chapter of my life. To each of you I owe a piece of this achievement, convinced that more than the result itself, what matters is who was there by your side to reach it.

Contents

List of Symbols

n	Number of propellers
$\mathcal{N}$	Index set of propellers
$\mathcal{F}_W$	Inertial world reference frame
$\mathcal{O}_W$	Origin of the inertial world reference frame
$\mathcal{F}_B$	Body-fixed reference frame
$\mathcal{O}_B$	Origin of the body-fixed reference frame
$\boldsymbol{p}$	Position of $\mathcal{O}_B$ in $\mathcal{F}_W$
$\boldsymbol{R}$	Rotation matrix of $\mathcal{F}_B$ w.r.t. $\mathcal{F}_W$
$\boldsymbol{v}$	Linear velocity of $\mathcal{O}_B$ in $\mathcal{F}_W$
$\boldsymbol{\omega}$	Angular velocity of $\mathcal{F}_B$ w.r.t. $\mathcal{F}_W$ expressed in $\mathcal{F}_B$
$\mathcal{F}_{P_i}$	Reference frame of the i-th propeller
$\mathcal{O}_{P_i}$	Origin of the i-th propeller reference frame
$\boldsymbol{p}_i$	Position of $\mathcal{O}_{P_i}$ relative to $\mathcal{O}_B$ in $\mathcal{F}_B$
l	Distance between $\mathcal{O}_B$ and $\mathcal{O}_{P_i}$
θ_i	Angular orientation of $\boldsymbol{p}_i$ on the $(\boldsymbol{x}_B, \boldsymbol{y}_B)$ plane
ϕ	Parameter that generalizes the arrangement of the propellers
α_i	Tilt angle of the i-th propeller about the $\boldsymbol{x}_{P_i}$ axis
β_i	Tilt angle of the i-th propeller about the $\boldsymbol{y}'_{P_i}$ axis
$\hat{\boldsymbol{w}}_i$	Spinning axis of the i-th propeller expressed in $\mathcal{F}_B$
w_i	Angular velocity of the i-th propeller about its spinning axis
$\boldsymbol{f}_i$	Lift force generated by the i-th propeller at $\mathcal{O}_{P_i}$
c_{f_i}	Thrust coefficient of the i-th propeller
$\boldsymbol{\tau}_i^d$	Drag moment generated by the i-th propeller at $\mathcal{O}_{P_i}$

$c^{+}_{\tau_i}$	Drag moment coefficient of the i-th propeller
$\boldsymbol{\tau}_i^t$	Thrust moment generated by the i-th propeller at $\mathcal{O}_{P_i}$
$\boldsymbol{F}_1$	Control force input matrix
$\boldsymbol{F}_2$	Control moment input matrix
$\boldsymbol{F}$	Control input matrix
$\boldsymbol{u}$	Control input vector
m	Total mass of the GTM
g	Gravity constant
$\boldsymbol{J}$	Inertia matrix of the GTM expressed in $\mathcal{F}_B$
$\boldsymbol{f}_c^A$	Spurious force
$\boldsymbol{f}_c^B$	Free force
$\mathfrak{F}$	Control force space
$\mathfrak{F}_A$	Spurious control force space
$\mathfrak{F}_B$	Free control force space
$\boldsymbol{d}_\star$	Preferential direction of the GTM in $\mathcal{F}_B$
$\boldsymbol{p}_r$	Reference position
$\boldsymbol{R}_r$	Reference rotation matrix
$\boldsymbol{R}_d$	Desired rotation matrix
$\boldsymbol{f}_r$	Reference control force
$\boldsymbol{\tau}_r$	Reference control moment
$\boldsymbol{w}_r$	Reference control wrench
$\boldsymbol{u}_r$	Reference control input
$\boldsymbol{u}_\tau$	Control input for the implementation of the reference control moment
$\boldsymbol{u}_f$	Control input for the implementation of the reference control force
$\boldsymbol{e}_p$	Position tracking error
$\boldsymbol{e}_R$	Attitude tracking error
Ψ	Attitude error function
$\boldsymbol{e}_\omega$	Angular velocity tracking error
$\boldsymbol{P}_\star^\perp$	Projection operator onto the orthogonal complement of $\boldsymbol{d}_\star$

$\boldsymbol{X}$	Misalignment between the preferential direction and the desired thrust direction
$\boldsymbol{\omega}_d$	Desired angular velocity
$e_p^{\max}$	Maximum position tracking error allowed
$e_R^{\max}$	Maximum attitude tracking error allowed
$\omega^{\max}$	Maximum angular velocity allowed
$\mathcal{D}$	Stability domain
$\mathcal{D}_a$	Region of attraction
$\mathcal{G}$	Set of admissible control gains
γ	Ratio between the maximum and minimum singular values of $\boldsymbol{F}_1$ and $\boldsymbol{F}_2$, respectively
$\lambda_{\max}(\cdot)$	Maximum eigenvalue of a matrix
$\lambda_{\min}(\cdot)$	Minimum eigenvalue of a matrix
c_1	Slack parameter for the stability analysis
c_2	Slack parameter for the stability analysis
ψ	Upper bound for the attitude error function Ψ
δ	Upper bound for the projection of the reference control force direction onto the heading direction (first column of $\boldsymbol{R}_r$)

Part I

Introduction

Chapter 1

Introduction

Since the dawn of human civilization, man has always observed nature in order to understand its mechanisms and shape it to face the challenges that arose during his evolutionary journey. The concept behind this thinking is known as biomimicry, or the observation of nature to understand its principles and find solutions to the concrete problems that stood between man and the future. Engineering pioneers such as Leonardo da Vinci began to meticulously observe the flight of birds, the morphology of their wings, and their light yet resistant structure in order to understand the principles that guided their efficiency and agility. These studies provided the fundamental knowledge for human flight. Today, this legacy is reflected in unmanned aerial vehicles, commonly known as drones.

1.1 Motivation and Applications

In recent years, UAVs have become increasingly popular, probably due to their vertical take-off and landing capabilities, but above all because they do not require complex mechanisms such as swash plates or teeter hinges (typical of traditional helicopters, for example). For these reasons, they have found application in a wide range of sectors, offering practical solutions to numerous problems. For example, in agriculture, they allow crops to be monitored and harvests to be estimated [6, 40]. In mapping and environmental monitoring, UAVs provide valuable data for terrain analysis and infrastructure inspection, especially in hard-to-reach areas [31, 33, 2, 13].

UAVs are also used in surveillance and security, enabling efficient area coverage and real-time monitoring [36, 7]. In logistics, they help meet last-mile delivery and urgent transport needs, particularly where traditional methods encounter issues [28, 12]. Search and rescue operations benefit from their rapid deployment and coordination capabilities, which improve response times [10, 43, 24].

Recent developments in aerial manipulation have expanded the range of tasks that UAVs can perform. For example, soft grippers have been developed that allow drones to grasp objects during flight [41]. Fully actuated UAVs are now capable of applying controlled forces for inspection tasks [2] and can interact with surfaces using tactile sensors [13]. Furthermore, cooperative grasping and transport by multiple UAVs has evolved from early attempts to more systematic approaches with established design and control methods [25, 38].

Overall, these examples highlight just a few of the many ways UAVs are being used to address practical problems across different domains, reflecting their growing presence and utility in everyday life [35].

1.2 Full-Actuation and Rotor Failures

While the modeling, design, and control of quadrotors are now well understood, recent research has increasingly focused on redundant multirotor platforms—those equipped with five, six, seven, or more propellers. These platforms can achieve fully actuated or omnidirectional flight, providing additional degrees of freedom that allow for independent control of position and orientation. This capability enables more precise force and torque generation, which is particularly useful for advanced aerial manipulation and interaction tasks. Recent developments include pentacopters capable of adhering to vertical surfaces, as well as heptarotors and hexacopters with tiltable rotors that can hover in arbitrary orientations. These examples demonstrate how redundancy in the number of propellers leads to new actuation capabilities and expands the range of possible applications [34, 4, 32, 1, 14, 39, 21, 16, 19].

When dealing with such UAVs, analyzing their robustness to rotor failures becomes interesting and relevant. Of particular interest is understanding how the actuation capabilities of the drone degrade when a propeller fails. In these scenarios, the platform may lose the ability to independently control its position and orientation, resulting in partial coupling and parasitic forces that hinder full control authority. The ability to design a control law that allows the platform to reach a forced equilibrium point—achieving static hovering with zero linear and angular velocity—after a rotor failure is highly valuable. This property is fundamental to prevent abrupt collisions or more severe consequences following a failure. A deeper theoretical understanding of the actuation properties of multirotors is needed to address these challenges.

Several works have addressed these challenges. Du et al. [5] performed a controllability analysis based on the linearized multirotor dynamics around hovering, showing that controllability after a rotor failure strongly depends on the propeller spinning directions. Giribet et al. [11] proposed a design method for star-shaped hexarotors that preserves the ability to reject disturbance moments in all directions, even after any single motor failure. In [27], Michieletto et al. demonstrated that by applying a modest, common tilt to all the spinning axes of the propellers, a conventional star-shaped hexarotor can be made tolerant to a single rotor failure, thus enabling the platform to achieve static hovering even after a fault. Moreover, they conducted an in-depth analysis of the actuation capabilities of UAVs, offering definitions that allow for the classification of different drones according to their actuation properties. In particular, they provided conditions under which a platform can be considered *partially coupled*.

1.3 Geometric Control for Static Hovering

As aforementioned, the choice of control strategy is crucial to ensure that the platform can achieve static hovering after a rotor failure. Traditional approaches—such as proportional-derivative controllers or linear quadratic regulators, typically formulated using Euler angles or quaternions (see, e.g., [3, 8])—are limited by their underlying representations. Controllers based on Euler angles are susceptible to gimbal-lock singularities, while quaternion-based methods face the double-cover issue, where a single orientation corresponds to two opposite quaternions, potentially introducing discontinuities in the control law.

A solution is offered by geometric controllers that act directly on the Special Orthogonal Group $\mathbf{SO}(3)$ and, more generally, on the Special Euclidean Group $\mathbf{SE}(3)$. In this framework the attitude is represented by global entities on the manifold rather than local coordinates, rendering the control law coordinate-free: no singularities, no arbitrary representation choices, and no sign flips. The outcome is smoother tracking and proofs of local exponential stability that remain valid even under sizeable disturbances or parameter uncertainties [22].

In [26], Michieletto et al. provide a formal definition of *static hovering* for multirotor platforms, characterizing it as the ability to maintain zero linear and angular velocity. They also establish general conditions under which a generically tilted multirotor[1] can achieve static hovering. Furthermore, the authors propose a geometric control law that enables the platform to reach and maintain this equilibrium state. This control law has been extensively validated through simulations and real-world experiments at the Laboratory for Analysis and Architecture of Systems[2] on a tilted hexarotor platform shown in Figure 1.1.

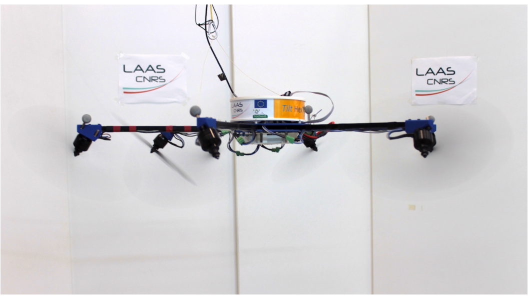

Figure 1.1. A tilted hexarotor platform used for experimental validation of the control law proposed in [26].

The control law applies to a broad class of generically tilted multirotor platforms, comprising at least four propellers arranged beyond the standard regular polygon configuration. These platforms are fully actuated in orientation and possess at least one direction in which thrust can be regulated independently of the applied moment, enabling static hovering.

---

[1] A *generically tilted multirotor* is a platform in which the spinning axes of the propellers are intentionally tilted with respect to the body-fixed reference frame, without requiring additional external hardware.

[2] LAAS-CNRS, Université de Toulouse, CNRS, Toulouse, France. A video of the experimental results is available at: `https://youtu.be/Oa65WMc1Ct8?si=oCjqIWRUyThvaqcQ`.

It is worth noting that this control law is not limited to multirotor UAVs. Rather, it can be applied to any floating rigid body that shares the same actuation capabilities, regardless of the surrounding medium. This includes, for example, underwater vehicles such as submarines, as well as spacecraft and satellites operating in space. The underlying principles of the control strategy remain valid as long as the platform possesses the necessary actuation properties, making the approach broadly applicable across different domains of robotics and autonomous systems.

Importantly, the control law is designed to achieve static hovering even in the presence of partial force-moment coupling, whether this arises after a rotor failure or is inherent to the platform's configuration. This makes the approach applicable to both fully actuated and underactuated, partially-coupled vehicles. The results presented in this thesis provide a rigorous theoretical framework for establishing the local exponential stability of the closed-loop error dynamics induced by the geometric control law. Specifically, a general proof pattern is developed that can be systematically applied to demonstrate local exponential stability of the static hovering equilibrium, even under partial coupling due to rotor failures. This analysis leverages advanced tools from nonlinear control theory and differential geometry, enabling a unified and coordinate-free treatment of the error dynamics on the underlying manifold.

The structure of the thesis is as follows. Chapter 2 introduces the mathematical model for a generically tilted multirotor, building on the foundational work of [27, 22]. This model captures both the general arrangement of the propellers and the orientation of each spinning axis. Chapter 3 synthesizes the analysis from [27], focusing on the fundamental properties of the model, including actuation capabilities and the conditions under which a platform is considered partially coupled. In Chapter 4, thanks to the seminal works of [27, 26], we define static hovering and establish the criteria that enable a generically tilted multirotor to achieve it. In Chapter 5 is presented the geometric control law provided by Michieletto et al. in [26], that allows the platform to realize static hovering. The main original contribution of this thesis is detailed in Chapter 6, where we rigorously prove the local exponential stability of the closed-loop error dynamics induced by the proposed control law. Although the control law has been extensively validated, Chapter 7 provides illustrative numerical simulations, not to validate the control law itself, but to demonstrate the stability results obtained in the thesis through three representative maneuvers for a partially coupled platform. Finally, Chapter 8 summarizes the main contributions and outlines directions for future research.

At the end of the thesis, several appendices are provided. These may be useful to the reader as a quick reference for some theoretical concepts on stability theory, as well as a summary of several calculations whose results are used throughout the proofs.

Part II

Modeling and Fundamental Properties

Chapter 2

Mathematical Modeling of a Generically Tilted Multirotor

In this chapter, we will attempt to derive a mathematical model for generically tilted multirotors (GTM). By synergistically integrating kinematic and dynamic equations, the model should provide a complete description of the platform's behaviour. The kinematic equations describe the motion in terms of linear and angular velocities, while the dynamic equations capture the forces and moments acting on the system.

The establishment of a rigorous mathematical model is of paramount importance, as it constitutes the essential groundwork upon which advanced control laws are conceived. Through such a model, one is endowed with the analytical means to systematically design control strategies that induce the desired behaviour in the platform, thereby enabling precise and reliable operation even in the presence of complex and uncertain environments.

The mathematical model presented in this chapter is entirely based on the seminal works of [27] and [22]. Here, a synthesis of these two references is provided, combining their methodologies and summarizing key concepts to offer a unified exposition. For an accessible introduction to multirotor platform modelling, see [42].

2.1 Generically Tilted Multirotors

The following definition, adapted from Definition 1 in [15], helps clarify what is meant by a generically tilted multirotor (GTM).

Definition 2.1 (Generically Tilted Multirotors, [15])**.** *A* GTM *(Generically Tilted Multirotor) is a rigid body equipped with n lightweight propellers, each capable of producing the aerodynamic forces and moments required to control the vehicle's motion. Let*

$$\mathcal{N} = \{1, 2, \dots, n\}$$

denote the index set of the propellers. The system so defined is completely described by the quantity of propellers and their arrangement (their position and tilt angle).

Before proceeding, it is important to note that the GTM model developed here is an approximation of the real system. Specifically, we will neglect the mass, inertia, and secondary aerodynamic effects of the propellers, such as, e.g., flapping effects. This assumption, widely adopted in the literature, is justified by the fact that the mass and inertia of the propellers are negligible compared to those of the main body.

To eliminate any potential ambiguities, the following notation will be formally adopted.

- ${}^{c}\boldsymbol{r} \in \mathbb{R}^3$ denotes a vector whose coordinates are expressed in frame $\mathcal{F}_c$;
- $\boldsymbol{r}_j^i \in \mathbb{R}^3$ denotes the position of the origin of frame $\mathcal{F}_j$ with respect to the origin of frame $\mathcal{F}_i$;
- $\dot{\boldsymbol{r}}_j^i \in \mathbb{R}^3$ denotes the velocity of the origin of frame $\mathcal{F}_j$ with respect to the origin of frame $\mathcal{F}_i$;
- ${}^{i}\boldsymbol{R}_j \in \mathbf{SO}(3)$ denotes the orientation of frame $\mathcal{F}_j$ with respect to frame $\mathcal{F}_i$;

For any vector $\boldsymbol{v} \in \mathbb{R}^3$, we decompose it into its magnitude and direction as

$$\boldsymbol{v} = \|\boldsymbol{v}\|\, \hat{\boldsymbol{v}},$$

where

- $\|\boldsymbol{v}\| = \sqrt{\boldsymbol{v}^\top \boldsymbol{v}} \in \mathbb{R}$ is the Euclidean norm of $\boldsymbol{v}$, and
- $\hat{\boldsymbol{v}} \in S^2 := \{\boldsymbol{x} \in \mathbb{R}^3 : \|\boldsymbol{x}\| = 1\}$ is the corresponding unit vector, defined by

$$\hat{\boldsymbol{v}} := \frac{\boldsymbol{v}}{\|\boldsymbol{v}\|}.$$

Hereafter, $\boldsymbol{e}_i$ will denote the i-th canonical basis vector of the reference frame expressed in its coordinates. In particular, $\boldsymbol{e}_i$ denotes the i-th column of the identity matrix $\boldsymbol{I}_3$.

2.2 Kinematics

In order to derive the GTM model, we will consider:

- The inertial world reference frame $\mathcal{F}_W = \{\mathcal{O}_W, (\boldsymbol{x}_W, \boldsymbol{y}_W, \boldsymbol{z}_W)\}$ with origin $\mathcal{O}_W$;
- The body-fixed reference frame $\mathcal{F}_B = \{\mathcal{O}_B, (\boldsymbol{x}_B, \boldsymbol{y}_B, \boldsymbol{z}_B)\}$ with origin $\mathcal{O}_B$ located at the center of mass of the rigid body.

The body-fixed reference frame $\mathcal{F}_B$ is a rigidly attached moving frame to the platform, which undergoes roto-translations with respect to the fixed world reference frame $\mathcal{F}_W$. The origin $\mathcal{O}_B$ of $\mathcal{F}_B$ is located at the center of mass (CoM) of the platform and generally does not coincide with the origin $\mathcal{O}_W$ of $\mathcal{F}_W$. The position of $\mathcal{O}_B$ relative to $\mathcal{O}_W$ is described by the vector ${}^{W}\boldsymbol{r}_B^W =: {}^{W}\boldsymbol{p} \in \mathbb{R}^3$, expressed in $\mathcal{F}_W$. The orientation of $\mathcal{F}_B$ w.r.t. $\mathcal{F}_W$ is described by the rotation matrix ${}^{W}\boldsymbol{R}_B \in \mathbf{SO}(3)$. Thus, the full pose of the vehicle in the world frame $\mathcal{F}_W$ is described by the pair ${}^{W}\boldsymbol{q} = ({}^{W}\boldsymbol{p}, {}^{W}\boldsymbol{R}_B) \in \mathbf{SE}(3)$.

In addition, the twist of the platform is described by the pair $({}^W\boldsymbol{v},\, {}^B\boldsymbol{\omega}_B^W)$, where ${}^W\boldsymbol{v} := {}^W\dot{\boldsymbol{r}}_B^W \in \mathbb{R}^3$ denotes the linear velocity of the center of mass $\mathcal{O}_B$ of the platform w.r.t. the velocity of the origin of $\mathcal{F}_W$, expressed in $\mathcal{F}_W$, and ${}^B\boldsymbol{\omega}_B^W \in \mathbb{R}^3$ represents the angular velocity of $\mathcal{F}_B$ w.r.t. $\mathcal{F}_W$, expressed in $\mathcal{F}_B$. Using the previous ingredients, the kinematics equations of a GTM can be derived. The linear kinematics of the platform is given by the relation

$$ {}^W\boldsymbol{v} = {}^W\dot{\boldsymbol{p}}. \tag{2.1}$$

The orientation kinematics is governed by the relation

$$ {}^W\dot{\boldsymbol{R}}_B = {}^W\boldsymbol{R}_B\boldsymbol{S}({}^B\boldsymbol{\omega}_B^W), \tag{2.2}$$

where $\boldsymbol{S} : \mathbb{R}^3 \to \mathfrak{so}(3)$, defined by the condition that $\boldsymbol{S}(\boldsymbol{x})\boldsymbol{y} = \boldsymbol{x} \times \boldsymbol{y}$ for all $\boldsymbol{x}, \boldsymbol{y} \in \mathbb{R}^3$, is the map that associates any vector in $\mathbb{R}^3$ with its corresponding skew-symmetric matrix belonging to $\mathfrak{so}(3)$ (see Appendix A for more details).

2.3 Actuation Units

Let $\mathcal{F}_{P_i} = \{\mathcal{O}_{P_i}, (\boldsymbol{x}_{P_i}, \boldsymbol{y}_{P_i}, \boldsymbol{z}_{P_i})\}$ denote the reference frame associated with the i-th propeller, where $\mathcal{O}_{P_i}$ represents its center, with $i \in \mathcal{N}$. The axis $\boldsymbol{z}_{P_i}$ aligns with the spinning axis of the propeller, while the plane defined by $\boldsymbol{x}_{P_i}$ and $\boldsymbol{y}_{P_i}$ is orthogonal to it, known as the spinning plane. The axis $\boldsymbol{x}_{P_i}$ is arbitrarily selected among those perpendicular to $\boldsymbol{z}_{P_i}$, and $\boldsymbol{y}_{P_i}$ is defined as $\boldsymbol{y}_{P_i} = \boldsymbol{z}_{P_i} \times \boldsymbol{x}_{P_i}$.

The position of $\mathcal{O}_{P_i}$ relative to $\mathcal{O}_B$ is described by the vector ${}^B\boldsymbol{p}_i := {}^B\boldsymbol{r}_{P_i}^B \in \mathbb{R}^3$, expressed in $\mathcal{F}_B$. We derive an expression for ${}^B\boldsymbol{p}_i$ to ensure the propellers are in a coplanar configuration[1]. The position of the i-th propeller is given by

$$ {}^B\boldsymbol{p}_i = l\boldsymbol{R}_Z(\theta_i)\boldsymbol{e}_1, \tag{2.3}$$

where l is the distance from the center of mass to the propeller, $\boldsymbol{R}_Z(\theta_i)$ is the canonical rotation matrix about the $\boldsymbol{z}_B$ axis by an angle $\theta_i := (i-1)\frac{2\pi}{n} - \frac{1}{2}(1+(-1)^i)\phi$, where ϕ is a parameter that generalizes the arrangement of the propellers, and $i \in \mathcal{N}$. The parameter $\phi \in [0, \frac{\pi}{3}]$ allows the propellers to be placed in a more general way than at the vertices of regular polygons. Specifically, $\phi = 0$ corresponds to the traditional star-shaped configuration, while $\phi \neq 0$ allows for a more general arrangement (i.e., Y-shaped configuration for $\phi = \frac{\pi}{3}$).

In general, the axis $\boldsymbol{z}_{P_i}$ is not parallel to the third body-fixed axis $\boldsymbol{z}_B$, leading to a difference in orientation between the frames $\mathcal{F}_{P_i}$ and $\mathcal{F}_B$. This relative orientation is captured by the rotation matrix ${}^B\boldsymbol{R}_{P_i} \in \mathbf{SO}(3)$, which maps vectors from $\mathcal{F}_{P_i}$ to $\mathcal{F}_B$. We can decompose each ${}^B\boldsymbol{R}_{P_i}$ into 3 consecutive rotations:

$$ {}^B\boldsymbol{R}_{P_i} = \boldsymbol{R}_Z(\theta_i)\boldsymbol{R}_X(\alpha_i)\boldsymbol{R}_Y(\beta_i), \tag{2.4}$$

---

[1] Although the ability to reallocate and reorient the propellers enhances design flexibility, it also increases the number of design parameters, making the design process more complex. To mitigate this complexity, we impose the constraint that the propeller centers and the center of mass (CoM) of the platform lie in the same plane.

where $\boldsymbol{R}_X(\alpha_i)$, $\boldsymbol{R}_Y(\beta_i)$, and $\boldsymbol{R}_Z(\theta_i)$ are the canonical rotation matrices about the $\boldsymbol{x}_B$, $\boldsymbol{y}_B$, and $\boldsymbol{z}_B$ axes by angles α_i, β_i, and θ_i, respectively. The angles α_i and β_i represent the tilt angles that uniquely define the rotation plane of the i-th propeller, $(\boldsymbol{x}_{P_i}, \boldsymbol{y}_{P_i})$, or equivalently, the orientation of the propeller spinning axis with respect to the body frame. The spinning plane of the i-th propeller is obtained starting from the plane $(\boldsymbol{x}_B, \boldsymbol{y}_B)$, then applying a first rotation of θ_i about the $\boldsymbol{z}_B$ axis to align the first body-fixed axis with $\boldsymbol{x}_{P_i}$, followed by a rotation of α_i about the $\boldsymbol{x}_{P_i}$ axis and a rotation of β_i about the $\boldsymbol{y}'_{P_i}$ axis, which is the intermediate axis obtained by applying the first two rotations.

The tilt angles α_i and β_i are defined as

$$\begin{aligned} \alpha_i &= (-1)^{i-1}\alpha, \quad \alpha \in \left[-\frac{\pi}{2}, \frac{\pi}{2}\right], \\ \beta_i &= (-1)^{i-1}\beta, \quad \beta \in \left[-\frac{\pi}{2}, \frac{\pi}{2}\right], \end{aligned}$$

with $i \in \mathcal{N}$. The parameters $\{\alpha_i, \beta_i\}_{i=1}^n$ dictate whether the propeller axes are parallel or differently oriented and are assumed constant during flight, except for tiltable rotor platforms. When $\alpha_i = \beta_i = 0$ for all $i \in \mathcal{N}$, the axes ${}^B\boldsymbol{z}_{P_i}$ align with ${}^B\boldsymbol{z}_B$, i.e., $\boldsymbol{e}_3$, defining a standard collinear multirotor configuration.

A graphic representation of the propeller's position and orientation is shown in Figure 2.1.

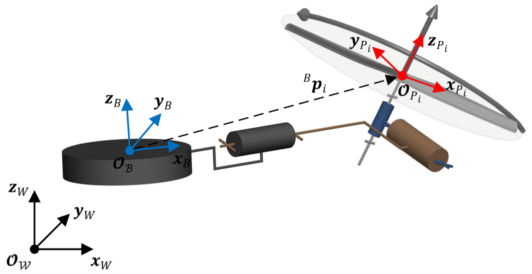

Figure 2.1. Representation of the position and orientation of the i-th propeller in the body frame $\mathcal{F}_B$. This picture is taken from [9].

The parameters defining each propeller are summarized as follows.

- *Aerodynamic parameters*: The propeller's shape and airfoil profile determine its aerodynamic forces and moments, typically characterized by the thrust coefficient c_{f_i} and drag coefficient c_{τ_i}. These parameters, usually provided by the manufacturer, influence payload capacity and energy consumption and are assumed constant during flight.

- *Propeller chord*: A propeller with an ascending chord generates thrust opposite to its angular velocity, while a descending-chord propeller generates thrust in the same direction. The drag moment is always opposed to the angular velocity. The propeller chord influences the value of k_i in the thrust and drag moment definitions.

- *Unidirectional or bidirectional thrust*: Most multirotors are designed with unidirectional thrust, where $0 \leq \underline{w}_i \leq w_i \leq \overline{w}_i$, with $\underline{w}_i, \overline{w}_i \in \mathbb{R}_{>0}$. Bidirectional thrust allows $\underline{w}_i \leq w_i \leq \overline{w}_i$, with $\underline{w}_i < 0$ and $\overline{w}_i > 0$, increasing thrust range but typically reducing c_{f_i} due to the need for symmetrical sections.

- *Fixed or actuated spinning axis*: A fixed spinning axis implies a constant orientation of $\boldsymbol{z}_{P_i}$ during flight. In contrast, an actuated spinning axis allows thrust vectoring by changing the orientation of $\boldsymbol{z}_{P_i}$ via servomotors. For this discussion, only fixed spinning axes are considered.
- *Position of the i-th propeller*: The position ${}^{B}\boldsymbol{p}_i$ relative to $\mathcal{O}_B$ affects the total moment applied to the platform's center of mass. Furthermore, the position of the propellers defines the type and structure of the platform.

This modeling approach, which parametrizes both the position and orientation of each propeller, enables the identification of a vast number of possible configurations, far beyond traditional arrangements such as regular polygons or parallel spinning axes. By allowing for arbitrary allocation and orientation of the propellers—while maintaining the constraint that all centers lie in the same plane—this framework provides a highly general and flexible foundation for the analysis and design of multirotor aerial vehicles. This generalization is taken from the approach proposed in [34].

2.4 Control Forces and Moments

The i-th propeller rotates with an angular velocity $\boldsymbol{w}_i \in \mathbb{R}^3$ about its spinning axis. The angular velocity can be expressed as

$$\boldsymbol{w}_i = \|w_i\| \hat{\boldsymbol{w}}_i = k_i w_i \boldsymbol{z}_{P_i}, \tag{2.5}$$

where $w_i \in \mathbb{R}_{>0}$ represents the magnitude of the angular velocity (i.e., the spinning rate) and $k_i \in \{-1, 1\}$ is the rotor's direction coefficient, determined by the propeller's design. Specifically, $k_i = 1$ corresponds to a counterclockwise (CCW) propeller, while $k_i = -1$ corresponds to a clockwise (CW) propeller. The unit vector $\hat{\boldsymbol{w}}_i$, which defines the direction of $\boldsymbol{w}_i$, is aligned with the spinning axis of the i-th propeller and is given by

$$\hat{\boldsymbol{w}}_i = k_i \boldsymbol{z}_{P_i}.$$

Due to its rotation, the i-th propeller generates a thrust (or lift) force $\boldsymbol{f}_i \in \mathbb{R}^3$ at $\mathcal{O}_{P_i}$, directed along the propeller axis $\boldsymbol{z}_{P_i}$. This force is expressed as

$$\boldsymbol{f}_i = k_i c_{f_i} \|\boldsymbol{w}_i\|^2 \hat{\boldsymbol{w}}_i = c_{f_i} w_i^2 \boldsymbol{z}_{P_i}, \tag{2.6}$$

where the constant $c_{f_i} > 0$ is the thrust coefficient of the i-th propeller, which depends on its physical characteristics. Here, the lift force is proportional to the square of the spinning rate w_i. The relation is derived using (2.5), i.e. taking into account the fact that CCW propellers produce lift in the same direction as their angular velocity, while CW propellers produce lift in the opposite direction.

In addition, the i-th propeller also generates a drag moment $\boldsymbol{\tau}_i^d \in \mathbb{R}^3$ at $\mathcal{O}_{P_i}$ whose direction is always opposite to the angular velocity of the propeller. Its expression is

$$\boldsymbol{\tau}_i^d = -c_{\tau_i}^+ \|\boldsymbol{w}_i\|^2 \hat{\boldsymbol{w}}_i = -k_i c_{\tau_i}^+ w_i^2 \boldsymbol{z}_{P_i}, \tag{2.7}$$

where $c_{\tau_i}^+ > 0$ is the drag coefficient of the i-th propeller, which depends on its physical characteristics. It is important to remind that the propeller is assumed to be sufficiently lightweight, such that its associated moment of inertia can be neglected when compared to the two primary aerodynamic effects described above, as well as the platform's moment of inertia.

Moreover, due to the presence of a thrust force $\boldsymbol{f}_i$ at $\mathcal{O}_{P_i}$, i.e. at $\boldsymbol{r}_{P_i}^B$, a thrust moment $\boldsymbol{\tau}_i^t \in \mathbb{R}^3$ is generated, whose expression is

$$\boldsymbol{\tau}_i^t = \boldsymbol{r}_{P_i}^B \times \boldsymbol{f}_i. \tag{2.8}$$

Finally, we proceed to represent the total force and total moment that the platform can generate, both in coordinates expressed in the body frame $\mathcal{F}_B$.

In coordinates, the total control force that the multirotor is able to generate is given by

$$^B\boldsymbol{f}_c = \sum_{i=1}^n {}^B\boldsymbol{f}_i = \sum_{i=1}^n c_{f_i}\, {}^B\boldsymbol{R}_{P_i}\boldsymbol{e}_3 w_i^2, \tag{2.9}$$

which follows directly from (2.6). The quantity ${}^B\boldsymbol{R}_{P_i}\boldsymbol{e}_3$ represents nothing more than the third column of ${}^B\boldsymbol{R}_{P_i}$, the definition of which has already been given in (2.4). It describes the third axis $\boldsymbol{z}_{P_i}$ of the propeller frame $\mathcal{F}_{P_i}$ expressed in the body frame $\mathcal{F}_B$.

The total drag moment acting on the multirotor is given by

$$^B\boldsymbol{\tau}^d = \sum_{i=1}^n {}^B\boldsymbol{\tau}_i^d = -\sum_{i=1}^n k_i c_{\tau_i}^+\, {}^B\boldsymbol{R}_{P_i}\boldsymbol{e}_3 w_i^2, \tag{2.10}$$

derived from (2.7). The total thrust moment acting on the multirotor is given by

$$^B\boldsymbol{\tau}^t = \sum_{i=1}^n {}^B\boldsymbol{p}_i \times {}^B\boldsymbol{f}_i = \sum_{i=1}^n c_{f_i}\, \boldsymbol{S}({}^B\boldsymbol{p}_i)\, {}^B\boldsymbol{R}_{P_i}\boldsymbol{e}_3 w_i^2, \tag{2.11}$$

whose expression follows directly from (2.8).

The total control moment generated by all propellers is given by

$$^B\boldsymbol{\tau}_c = {}^B\boldsymbol{\tau}^d + {}^B\boldsymbol{\tau}^t = \sum_{i=1}^n ({}^B\boldsymbol{\tau}_i^d + {}^B\boldsymbol{\tau}_i^t).$$

By exploiting (2.10) and (2.11), the generic term of the sum can be rewritten as

$$^B\boldsymbol{\tau}_i^d + {}^B\boldsymbol{\tau}_i^t = \left(-k_i c_{\tau_i}^+ \boldsymbol{I}_3 + c_{f_i}\boldsymbol{S}({}^B\boldsymbol{p}_i)\right) {}^B\boldsymbol{R}_{P_i}\boldsymbol{e}_3 w_i^2.$$

Therefore, the total control moment can be expressed as

$$^{B}\boldsymbol{\tau}_c = \sum_{i=1}^{n} \left(-k_i c_{\tau_i}^{+} \boldsymbol{I}_3 + c_{f_i} \boldsymbol{S}(^{B}\boldsymbol{p}_i)\right) {}^{B}\boldsymbol{R}_{P_i} \boldsymbol{e}_3 w_i^2. \tag{2.12}$$

Let $\boldsymbol{u} \in \mathbb{R}^n$ represent the vector containing the spinning rates of the propellers, i.e., $\boldsymbol{u} = [w_1^2 \dots w_n^2]^\top$, the expressions (2.9) and (2.12) can be succinctly reformulated as

$$^{B}\boldsymbol{f}_c = \boldsymbol{F}_1 \boldsymbol{u}, \qquad {}^{B}\boldsymbol{\tau}_c = \boldsymbol{F}_2 \boldsymbol{u}, \tag{2.13}$$

where the control force input matrix $\boldsymbol{F}_1 \in \mathbb{R}^{3\times n}$ and the control moment input matrix $\boldsymbol{F}_2 \in \mathbb{R}^{3\times n}$, which enclose the propeller arrangement along with the thrust and drag coefficients, are defined as

$$\boldsymbol{F}_1 = \begin{bmatrix} \boldsymbol{\mu}_{1,1} & \cdots & \boldsymbol{\mu}_{1,n} \end{bmatrix}, \tag{2.14}$$

where $\boldsymbol{\mu}_{1,i} \in \mathbb{R}^3$ is given by

$$\boldsymbol{\mu}_{1,i} = c_{f_i} \, {}^{B}\boldsymbol{R}_{P_i} \boldsymbol{e}_3, \tag{2.15}$$

and

$$\boldsymbol{F}_2 = \begin{bmatrix} \boldsymbol{\nu}_{2,1} & \cdots & \boldsymbol{\nu}_{2,n} \end{bmatrix}, \tag{2.16}$$

where $\boldsymbol{\nu}_{2,i} \in \mathbb{R}^3$ is given by

$$\boldsymbol{\nu}_{2,i} = \left(c_{f_i} \, \boldsymbol{S}(^{B}\boldsymbol{p}_i) - k_i c_{\tau_i}^{+} \boldsymbol{I}_3\right) {}^{B}\boldsymbol{R}_{P_i} \boldsymbol{e}_3. \tag{2.17}$$

Due to the fact that c_{f_i} and $c_{\tau_i}^{+}$ are positive constants, none of the columns of both $\boldsymbol{F}_1$ and $\boldsymbol{F}_2$ is a zero vector, and therefore, we have both $\text{rank}(\boldsymbol{F}_1) \geq 1$ and $\text{rank}(\boldsymbol{F}_2) \geq 1$ by construction.

By combining these two matrices, we can define the control input matrix $\boldsymbol{F} \in \mathbb{R}^{6\times n}$ as

$$\boldsymbol{F} = \begin{bmatrix} \boldsymbol{F}_1 \\ \boldsymbol{F}_2 \end{bmatrix}. \tag{2.18}$$

Remark 1 (Thrust Direction)**.** *Henceforth, the direction of the control force* $^{B}\hat{\boldsymbol{f}}_c = {}^{B}\boldsymbol{f}_c / \|^{B}\boldsymbol{f}_c\|$ *will be defined as the thrust direction of the GTM, indicating the direction along which the platform can generate thrust. This direction is dictated by the configuration of the propellers and their respective spinning rates. Specifically, for a feasible control input vector* $\bar{\boldsymbol{u}}$*, the thrust direction is supplied by*

$$^{B}\hat{\boldsymbol{f}}_c = \frac{\boldsymbol{F}_1 \bar{\boldsymbol{u}}}{\|\boldsymbol{F}_1 \bar{\boldsymbol{u}}\|}. \tag{2.19}$$

2.5 Dynamics

Finally, we can derive the model of a GTM by combining the kinematics and dynamics equations. From the second Newton's law, in the inertial world frame $\mathcal{F}_W$, the resultant force applied to the platform is equal to the rate of change of its linear momentum:

$$^{W}\boldsymbol{f} = m \, ^{W}\dot{\boldsymbol{v}},$$

where the constant $m \in \mathbb{R}_{>0}$ is the mass of the platform. The total force acting on the platform is the sum of the control force and the gravitational force:

$$^{W}\boldsymbol{f} = \, ^{W}\boldsymbol{f}_c + \, ^{W}\boldsymbol{f}_g,$$

where $^{W}\boldsymbol{f}_g = -mg\boldsymbol{e}_3$ is the gravitational force acting on the platform, with g being the acceleration due to gravity. Therefore the linear dynamics of the GTM can be expressed as

$$m \, ^{W}\dot{\boldsymbol{v}} = -mg\boldsymbol{e}_3 + \, ^{W}\boldsymbol{R}_B \boldsymbol{F}_1 \boldsymbol{u}. \tag{2.20}$$

Regarding the angular dynamics of the platform, we refer to the second Newton-Euler law. In the inertial world frame $\mathcal{F}_W$, this law states that the resultant moment acting on the platform equals the time derivative of its angular momentum. Specifically, this relationship is governed by the equation

$$^{W}\boldsymbol{\tau} = \frac{d}{dt}\left(^{W}\boldsymbol{J}_B \, ^{W}\boldsymbol{\omega}_B^W \right),$$

where $^{W}\boldsymbol{J}_B \in \mathbb{R}^{3\times 3}$ denotes the inertia matrix of the platform expressed in the world frame $\mathcal{F}_W$. It is important to note that this matrix is, in general, not constant when expressed in $\mathcal{F}_W$, as it depends on the platform's orientation. However, when expressed in the body-fixed frame $\mathcal{F}_B$, the inertia matrix, denoted as $^{B}\boldsymbol{J}_B$, becomes constant, reflecting the structural properties of the platform. By exploiting this property, from the previous equation we get

$$^{W}\boldsymbol{R}_B \, ^{B}\boldsymbol{\tau} = \frac{d}{dt}\left(^{W}\boldsymbol{R}_B \, ^{B}\boldsymbol{J}_B \, ^{B}\boldsymbol{\omega}_B^W \right),$$

where the orthonormal properties of $^{W}\boldsymbol{R}_B$ allow similar transformations also for moments between $\mathcal{F}_W$ and $\mathcal{F}_B$, ensuring consistency in the representation of the dynamics without introducing additional complexities. It should be noted that the transition between the two relationships above was made possible by exploiting the change of coordinates of an inertia matrix $^{W}\boldsymbol{J} = \, ^{W}\boldsymbol{R}_B \, ^{B}\boldsymbol{J} \, ^{W}\boldsymbol{R}_B^\top$, the change of coordinates of an angular velocity $^{W}\boldsymbol{\omega} = \, ^{W}\boldsymbol{R}_B \, ^{B}\boldsymbol{\omega}$, and the property $^{W}\boldsymbol{R}_B \, ^{W}\boldsymbol{R}_B^\top = \boldsymbol{I}_3$. Expanding the time derivative term leads to

$$^{W}\boldsymbol{R}_B \, ^{B}\boldsymbol{\tau} = \, ^{W}\dot{\boldsymbol{R}}_B \, ^{B}\boldsymbol{J}_B \, ^{B}\boldsymbol{\omega}_B^W + \, ^{W}\boldsymbol{R}_B \, ^{B}\boldsymbol{J}_B \, ^{B}\dot{\boldsymbol{\omega}}_B^W,$$

and rewriting the equation in the body-fixed frame $\mathcal{F}_B$, we arrive at

$$^{B}\boldsymbol{\tau} = \, ^{B}\boldsymbol{R}_W \, ^{W}\dot{\boldsymbol{R}}_B \, ^{B}\boldsymbol{J}_B \, ^{B}\boldsymbol{\omega}_B^W + \, ^{B}\boldsymbol{J}_B \, ^{B}\dot{\boldsymbol{\omega}}_B^W.$$

Here, recalling (2.2), the angular dynamics equation in $\mathcal{F}_B$ takes the form

$$ {}^{B}\boldsymbol{\tau} = \boldsymbol{S}({}^{B}\boldsymbol{\omega}_B^W)\,{}^{B}\boldsymbol{J}_B\,{}^{B}\boldsymbol{\omega}_B^W + {}^{B}\boldsymbol{J}_B\,{}^{B}\dot{\boldsymbol{\omega}}_B^W . $$

The latter fully describes the platform's angular dynamics in the body-fixed frame, emphasizing the role of both the inertial and gyroscopic effects. Finally, recalling that the total control moment acting on the platform is given by (2.12), the angular dynamics of the GTM can be expressed as

$$ {}^{B}\boldsymbol{J}_B\,{}^{B}\dot{\boldsymbol{\omega}}_B^W = -{}^{B}\boldsymbol{\omega}_B^W \times {}^{B}\boldsymbol{J}_B\,{}^{B}\boldsymbol{\omega}_B^W + \boldsymbol{F}_2\boldsymbol{u}. \tag{2.21} $$

We are now prepared to derive the complete mathematical model of the GTM. Before proceeding, we adopt a simplified notation by omitting the explicit dependency of variables on their respective coordinates or frames. This simplification is made purely for the sake of clarity and brevity, while keeping in mind that such dependencies remain implicit and must not be overlooked in the interpretation of the equations. Combining the linear kinematics (2.1), the orientation kinematics (2.2), the linear dynamics (2.20) and the angular dynamics (2.21), we obtain the complete mathematical model of a GTM:

$$ \begin{cases} \dot{\boldsymbol{p}} = \boldsymbol{v}, \\ m\dot{\boldsymbol{v}} = -mg\boldsymbol{e}_3 + \boldsymbol{R}\boldsymbol{F}_1\boldsymbol{u}, \\ \dot{\boldsymbol{R}} = \boldsymbol{R}\boldsymbol{S}(\boldsymbol{\omega}), \\ \boldsymbol{J}\dot{\boldsymbol{\omega}} = -\boldsymbol{\omega} \times \boldsymbol{J}\boldsymbol{\omega} + \boldsymbol{F}_2\boldsymbol{u}, \end{cases} \tag{2.22} $$

where we remind that the linear dynamics equation is expressed in the world frame $\mathcal{F}_W$, while the angular dynamics equation is expressed in the body-fixed frame $\mathcal{F}_B$.

In Fig. (2.2) a schematic representation of the model (2.22) is shown.

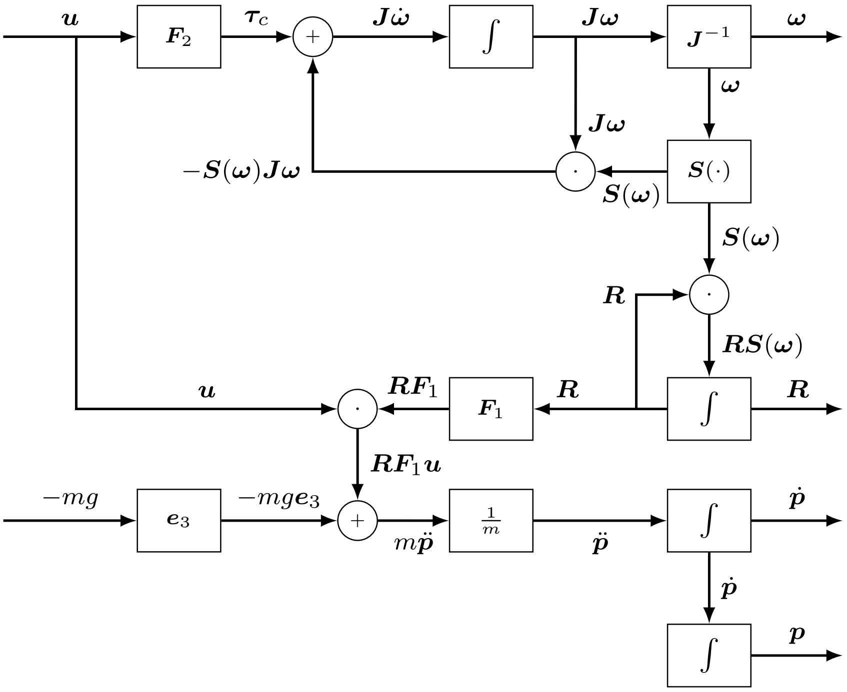

Figure 2.2. Schematic representation of a GTM. The rotation matrix $\boldsymbol{R}$ plays a fundamental role as the link between translational and rotational dynamics. This coupling is essential for accurately describing the platform's motion and control, and can be strategically exploited during control law design to address potential underactuation of the platform.

Chapter 3

Actuation Properties

This chapter systematically examines the actuation properties of a generically tilted multirotor (GTM), with a focus on the decoupling between force and moment. The concepts and results presented are based directly on the work of Michieletto et al. [27], to which we refer for a thorough and rigorous discussion. Their results are essential for the understanding and development of the main contributions that this thesis aims to make, and therefore one cannot redeem oneself from not presenting them. For this reason, this chapter is dedicated to summarising them, with the aim of providing the reader with the necessary background for what follows.

Throughout the discussion, it is assumed that the GTM satisfies the condition

$$\operatorname{rank}(\boldsymbol{F}_2) = 3. \tag{3.1}$$

Under this assumption, the input space $\mathbb{R}^n$ can be decomposed into the orthogonal subspaces $\operatorname{Im}(\boldsymbol{F}_2^\top)$ and its orthogonal complement $\ker(\boldsymbol{F}_2)$, as follows:

$$\mathbb{R}^n = \operatorname{Im}(\boldsymbol{F}_2^\top) \oplus \ker(\boldsymbol{F}_2).$$

This decomposition allows the control input $\boldsymbol{u} \in \mathbb{R}^n$ to be expressed via a suitable transformation. Specifically, one can introduce a nonsingular matrix $\boldsymbol{T} \in \mathbb{R}^{n\times n}$, defined as

$$\boldsymbol{T} = \begin{bmatrix} \boldsymbol{A}_2 & \boldsymbol{B}_2 \end{bmatrix}, \tag{3.2}$$

where the matrices $\boldsymbol{A}_2 \in \mathbb{R}^{n\times 3}$ and $\boldsymbol{B}_2 \in \mathbb{R}^{n\times(n-3)}$ satisfy

$$\begin{cases} \operatorname{Im}(\boldsymbol{A}_2) = \operatorname{Im}(\boldsymbol{F}_2^\top), \\ \operatorname{Im}(\boldsymbol{B}_2) = \ker(\boldsymbol{F}_2). \end{cases} \tag{3.3}$$

Given the full-rank assumption (3.1), $\boldsymbol{A}_2$ has rank 3, while $\boldsymbol{B}_2$ has rank $n-3$. Using this transformation, the control input can be written as

$$\boldsymbol{u} = \boldsymbol{T}\tilde{\boldsymbol{u}} = \boldsymbol{A}_2\tilde{\boldsymbol{u}}_A + \boldsymbol{B}_2\tilde{\boldsymbol{u}}_B, \tag{3.4}$$

where $\tilde{\boldsymbol{u}}_A \in \mathbb{R}^3$ and $\tilde{\boldsymbol{u}}_B \in \mathbb{R}^{n-3}$.

Applying this transformation, the control force and moment can be rewritten as

$$\boldsymbol{f}_c = \boldsymbol{F}_1\boldsymbol{u} = \boldsymbol{F}_1\boldsymbol{T}\tilde{\boldsymbol{u}} = \boldsymbol{F}_1\boldsymbol{A}_2\tilde{\boldsymbol{u}}_A + \boldsymbol{F}_1\boldsymbol{B}_2\tilde{\boldsymbol{u}}_B =: \boldsymbol{f}_c^A + \boldsymbol{f}_c^B, \tag{3.5}$$

$$\boldsymbol{\tau}_c = \boldsymbol{F}_2\boldsymbol{u} = \boldsymbol{F}_2\boldsymbol{T}\tilde{\boldsymbol{u}} = \boldsymbol{F}_2\boldsymbol{A}_2\tilde{\boldsymbol{u}}_A + \boldsymbol{F}_2\boldsymbol{B}_2\tilde{\boldsymbol{u}}_B =: \boldsymbol{\tau}_c^A + \boldsymbol{\tau}_c^B. \tag{3.6}$$

Since $\mathrm{Im}\,(\boldsymbol{B}_2) = \ker\,(\boldsymbol{F}_2)$, it follows that $\boldsymbol{F}_2\boldsymbol{B}_2\boldsymbol{x} = \boldsymbol{0}$ for any $\boldsymbol{x} \in \mathbb{R}^{n-3}$, so $\boldsymbol{\tau}_c^B = \boldsymbol{0}$. Furthermore, the matrix $\boldsymbol{F}_2\boldsymbol{A}_2 \in \mathbb{R}^{3\times 3}$ is invertible[1], ensuring that any desired moment $\boldsymbol{\tau}^\star \in \mathbb{R}^3$ can be achieved by selecting $\boldsymbol{\tau}_c^A = (\boldsymbol{F}_2\boldsymbol{A}_2)^{-1}\,\boldsymbol{\tau}^\star$ in (3.6), with $\tilde{\boldsymbol{u}}_B$ arbitrary.

The control force $\boldsymbol{f}_c \in \mathrm{Im}\,(\boldsymbol{F}_1) =: \mathfrak{F} \subseteq \mathbb{R}^3$ is thus decomposed into two components:

- $\boldsymbol{f}_c^A \in \mathrm{Im}\,(\boldsymbol{F}_1\boldsymbol{A}_2) =: \mathfrak{F}_A \subseteq \mathbb{R}^3$, representing the component induced by the allocation of inputs required to generate the control moment;
- $\boldsymbol{f}_c^B \in \mathrm{Im}\,(\boldsymbol{F}_1\boldsymbol{B}_2) =: \mathfrak{F}_B \subseteq \mathbb{R}^3$, corresponding to the component that can be assigned independently of the control moment, via inputs in $\ker\,(\boldsymbol{F}_2)$, i.e., $\tilde{\boldsymbol{u}}_B$.

Since $\boldsymbol{T}$ is nonsingular, it follows that $\mathfrak{F} = \mathfrak{F}_A + \mathfrak{F}_B$. Moreover, as $1 \leq \mathrm{rank}(\boldsymbol{F}_1) \leq 3$, it holds that $1 \leq \dim(\mathfrak{F}) \leq 3$, i.e., $1 \leq \dim(\mathfrak{F}_A) + \dim(\mathfrak{F}_B) \leq 3$. In particular, since $\mathfrak{F}_B \subseteq \mathfrak{F}$, one has $\dim(\mathfrak{F}_B) \leq \dim(\mathfrak{F}) \leq 3$. The dimension of $\mathfrak{F}_B$ and its relation to $\mathfrak{F}$ provide insight into the actuation capabilities of the GTM.

Below we report Definitions 1 and 2 presented in [27], which provide two criteria for classifying a GTM based on the results just discussed.

Definition 3.1 (First classification of a GTM, [27])**.** *A GTM is said to be*

1. ***fully coupled** (FC) if* $\dim(\mathfrak{F}_B) = 0$, *i.e., if* $\boldsymbol{F}_1\boldsymbol{B}_2 = \boldsymbol{0}$. *Here, the control force* $\boldsymbol{f}_c$ *is generated solely by the "spurious" force* $\boldsymbol{f}_c^A$*;*
2. ***partially coupled** (PC) if* $1 \leq \dim(\mathfrak{F}_B) < 3$ *and* $\mathfrak{F}_B \subset \mathfrak{F}$*, i.e., the control force* $\boldsymbol{f}_c$ *is generated by both the "spurious" force* $\boldsymbol{f}_c^A$ *and the "free" force* $\boldsymbol{f}_c^B$*;*
3. ***fully decoupled** (FD) if* $\mathfrak{F}_B = \mathfrak{F}$*, or equivalently, if* $\mathfrak{F}_A \subseteq \mathfrak{F}_B$*. Here, the control force* $\boldsymbol{f}_c$ *can be faithfully implemented by the "free" force* $\boldsymbol{f}_c^B$*.*

In a fully coupled (FC) GTM, the control force is entirely determined by the implemented control moment, as $\boldsymbol{f}_c^B = \boldsymbol{0}$ and thus $\boldsymbol{f}_c = \boldsymbol{f}_c^A$. In a partially coupled (PC) GTM, the component of the control force within $\mathfrak{F}_B$ can be independently assigned, while the component within $\mathfrak{F}_B^\perp \cap \mathfrak{F}$ remains dependent on the implemented control moment. In a fully decoupled (FD) GTM, the control force can be freely assigned throughout the entire space $\mathfrak{F}$, independently of the control moment. It is important to note that the FD property does not necessarily imply that the control force can be assigned in the whole space $\mathbb{R}^3$, unless $\dim(\mathfrak{F}) = 3$.

The second key classification is reported below:

Definition 3.2 (Second classification of a GTM, [27])**.** *A GTM*

1. *has a **decoupled direction** (D1) if* $\dim(\mathfrak{F}_B) \geq 1$*,*

---

[1] If $\boldsymbol{A} \in \mathbb{R}^{3\times n}$ has rank 3, then $\boldsymbol{A}\boldsymbol{A}^\top$ is symmetric positive-definite and invertible.

2. has a ***decoupled plane*** *($D2$) if dim($\mathfrak{F}_B$) ≥ 2,*

3. is ***fully actuated*** *($D3$) if dim($\mathfrak{F}_B$) $= 3$.*

Combining the previous definitions, we say that a GTM

1. has a **single decoupled direction** ($SD1$) if $\dim(\mathfrak{F}_B) = 1$,
2. has a **single decoupled plane** ($SD2$) if $\dim(\mathfrak{F}_B) = 2$,

If a GTM is $D1$, there exists at least one direction in the force space along which the projection of the control force can be chosen independently of the control moment. For a GTM that is $D2$, there exists at least one plane in the force space along which the projection of the control force can be independently assigned. Finally, if a GTM is $D3$, the control force can be assigned freely, independently of the control moment, throughout the entire space $\mathbb{R}^3$.

Moreover, in [27] is shown that the $D3$ definition is equivalent to the classical criterion commonly adopted in the literature, namely,

$$\operatorname{rank}(\boldsymbol{F}) = \operatorname{rank}\left(\begin{bmatrix}\boldsymbol{F}_1\\ \boldsymbol{F}_2\end{bmatrix}\right) = 6. \tag{3.7}$$

Postmultiplying $\boldsymbol{F}$ by the transformation matrix $\boldsymbol{T}$ in (3.4) does not change its rank:

$$\operatorname{rank}(\boldsymbol{F}\boldsymbol{T}) = \operatorname{rank}\left(\begin{bmatrix}\boldsymbol{F}_1\\ \boldsymbol{F}_2\end{bmatrix}\begin{bmatrix}\boldsymbol{A}_2 & \boldsymbol{B}_2\end{bmatrix}\right) = \operatorname{rank}\left(\begin{bmatrix}\boldsymbol{F}_1\boldsymbol{A}_2 & \boldsymbol{F}_1\boldsymbol{B}_2\\ \boldsymbol{F}_2\boldsymbol{A}_2 & \boldsymbol{0}\end{bmatrix}\right) = 6. \tag{3.8}$$

Given the assumption in (3.1), we have $\operatorname{rank}(\boldsymbol{F}_2\boldsymbol{A}_2) = 3$. Therefore, $\operatorname{rank}(\boldsymbol{F}) = 6$ if and only if $\operatorname{rank}(\boldsymbol{F}_1\boldsymbol{B}_2) = 3$, which is precisely the $D3$ condition as previously defined.

For completeness and to provide a clear overview, we now summarize all possible combinations arising from the relationships among the definitions introduced above. Specifically, Table 3.1—which corresponds to Table 1 in [27]—systematically presents the interplay between the notions of fully coupled (FC), partially coupled (PC), fully decoupled (FD), and the existence of decoupled directions and planes ($D1$, $D2$, $D3$).

It is evident that $D3$ implies both $D2$ and $D1$, and $D2$ implies $D1$. Moreover, $D1$ (and thus $D2$) can coexist with the PC and FD classifications, but not with FC: if a GTM is FC, then $\boldsymbol{F}_1\boldsymbol{B}_2 = \boldsymbol{0}$, which is incompatible with the $D1$ (and $D2$) property. Furthermore, $D3$ implies FD, while the converse is not always true and depends on the dimension of the space $\mathfrak{F}_B$.

3.1 Standard (Collinear) Multirotors

For completeness, we briefly recall the classical case of collinear multirotors, which is widely encountered in real-world applications. This configuration has been extensively studied in the work of Michieletto et al. [27], and here we limit ourselves to summarizing its main properties for reference.

Standard multirotors are typically characterized by an even number of propellers arranged in a symmetric configuration, with a balanced selection of clockwise (CW)

Table 3.1. Classification of GTM actuation properties according to the dimensions of $\mathfrak{F}_B$ and $\mathfrak{F}$ (taken from [27]). Color highlights: FC (red), PC (yellow), FD (green), N/A (gray, invalid combination).

		Decoupled Directions		
			Decoupled Planes	
	$\dim \mathfrak{F}_B = 0$	$\dim \mathfrak{F}_B = 1$	$\dim \mathfrak{F}_B = 2$	$\dim \mathfrak{F}_B = 3$
$\mathfrak{F}_B \subsetneq \mathfrak{F}$	🟥 FC	🟨 PC & SD1	🟨 PC & SD2	⬜ N/A
$\mathfrak{F}_B = \mathfrak{F}$	⬜ N/A	🟩 FD & SD1	🟩 FD & SD2	🟩 D3 (FD)
	$\dim \mathfrak{F} \geq 1$	$\dim \mathfrak{F} \geq 1$	$(\Rightarrow \dim \mathfrak{F} \geq 2)$	$(\Rightarrow \dim \mathfrak{F} = 3)$

and counterclockwise (CCW) types, and all spinning axes aligned parallel to one another, i.e., $\boldsymbol{z}_{P_i} = \boldsymbol{z}_P$ for all $i \in \mathcal{N}$. This configuration corresponds to the scenario discussed in Subsection 2.3, where the tilt angles α_i and β_i are set to zero, resulting in $\boldsymbol{z}_{P_i} = \boldsymbol{z}_P$ for all $i \in \mathcal{N}$.

Under these conditions, the matrices $\boldsymbol{F}_1$ and $\boldsymbol{F}_2$ take the following forms:

$$\boldsymbol{F}_1 = \begin{bmatrix} c_{f_1}\boldsymbol{z}_P & \cdots & c_{f_n}\boldsymbol{z}_P \end{bmatrix}, \tag{3.9}$$

$$\boldsymbol{F}_2 = \begin{bmatrix} c_{f_1}\boldsymbol{r}_1 \times \boldsymbol{z}_P & \cdots & c_{f_n}\boldsymbol{r}_n \times \boldsymbol{z}_P \end{bmatrix} + \begin{bmatrix} c_{\tau_1}\boldsymbol{z}_P & \cdots & c_{\tau_n}\boldsymbol{z}_P \end{bmatrix}. \tag{3.10}$$

It is evident that $\operatorname{rank}(\boldsymbol{F}_1) = 1$, as all columns are parallel. Conversely, $\boldsymbol{F}_2$ is composed of two contributions: the cross products $c_{f_i}\boldsymbol{r}_i \times \boldsymbol{z}_P$, and the drag moments $c_{\tau_i}\boldsymbol{z}_P$. The drag moment matrix has rank 1, as all its columns are parallel. However, the cross product matrix consists of columns that are linearly independent of the drag moment columns. Consequently, $\boldsymbol{F}_2$ is full rank if and only if:

$$\operatorname{rank}\left(\begin{bmatrix} c_{f_1}\boldsymbol{r}_1 \times \boldsymbol{z}_P & \cdots & c_{f_n}\boldsymbol{r}_n \times \boldsymbol{z}_P \end{bmatrix}\right) = 2,$$

which occurs when at least two vectors $\boldsymbol{r}_i \times \boldsymbol{z}_P$ and $\boldsymbol{r}_j \times \boldsymbol{z}_P$ are linearly independent, for some $i, j \in \mathcal{N}$.

The family of standard multirotors consists of systems that satisfy the fully decoupling (FD) condition. This is evident from the fact that these systems adhere to the property $\operatorname{Im}(\boldsymbol{F}_1^\top) \subseteq \ker(\boldsymbol{F}_2) = \operatorname{Im}(\boldsymbol{B}_2)$. From this condition, and recalling that $\boldsymbol{F}_1 \neq \boldsymbol{0}$, it follows that $\boldsymbol{F}_1\boldsymbol{B}_2 \neq \boldsymbol{0}$. In particular, for any vector $\boldsymbol{x} \in \mathbb{R}^3$, one has $\boldsymbol{F}_2\boldsymbol{F}_1^\top\boldsymbol{x} = \boldsymbol{0}$, as $\boldsymbol{F}_1^\top\boldsymbol{x} \in \ker(\boldsymbol{F}_2)$. Equivalently, $\boldsymbol{F}_1\boldsymbol{F}_2^\top\boldsymbol{x} = \boldsymbol{0}$, and since $\boldsymbol{F}_2^\top\boldsymbol{x} \in \operatorname{Im}(\boldsymbol{F}_2^\top) = \operatorname{Im}(\boldsymbol{A}_2)$, we get $\boldsymbol{F}_1\boldsymbol{A}_2\boldsymbol{x} = \boldsymbol{0}$ for all $\boldsymbol{x} \in \mathbb{R}^3$, or alternatively:

$$\boldsymbol{F}_1\boldsymbol{A}_2 = \boldsymbol{0}. \tag{3.11}$$

This result implies $\mathfrak{F}_A = \{\boldsymbol{0}\}$, leading to $\mathfrak{F}_B = \mathfrak{F}$, thereby confirming that these systems are FD. The symmetrical geometry and parallel spinning axes of classical multirotors inherently ensure compliance with this condition.

To demonstrate that $\boldsymbol{F}_2\boldsymbol{F}_1^\top = \mathbf{0}$, we first note that $\boldsymbol{F}_2\boldsymbol{F}_1^\top$ can be expressed as the sum $\boldsymbol{C}_f + \boldsymbol{C}_\tau$, where:

$$\boldsymbol{C}_f = \left(\left(\sum_{i\in\mathcal{N}} c_{f_i}^2 \boldsymbol{r}_i\right) \times \boldsymbol{z}_P\right) \boldsymbol{z}_P^\top \in \mathbb{R}^{3\times3},\ \boldsymbol{C}_\tau = \left(\sum_{i\in\mathcal{N}} c_{f_i} c_{\tau_i}\right) \boldsymbol{z}_P \boldsymbol{z}_P^\top \in \mathbb{R}^{3\times3}.$$

By appropriately selecting the positions and coefficients $\{c_{\tau_i}, c_{f_i}\}$ of the propellers, it is straightforward to make $\boldsymbol{C}_f = \boldsymbol{C}_\tau = \mathbf{0}$. For instance, it suffices to balance the propellers in pairs, such that $\boldsymbol{r}_i = -\boldsymbol{r}_j$, $c_{f_i} = c_{f_j}$, and $c_{\tau_i} = -c_{\tau_j}$ for $i \in \{1, 2, \ldots, \frac{n}{2}\}$ and $j = i + \frac{n}{2}$. Under these conditions, $\boldsymbol{F}_2\boldsymbol{F}_1^\top = \mathbf{0}$, and the system is fully decoupled (FD).

Furthermore, by referring to the auxiliary table (3.1), it can be observed that such multirotor systems possess a decoupled direction ($D1$), while lacking a decoupled plane ($D2$) and full actuation ($D3$). This follows from the fact that $\operatorname{rank}(\boldsymbol{F}_1) = 1$, which implies $\dim(\mathfrak{F}_B) = 1$. Consequently, classical multirotor systems are FD GTMs with a single decoupled direction ($SD1$).

In these platforms, the control moment and control force can be treated independently. Moreover, two key properties have been instrumental in ensuring the simplicity and success of their control. First, the control force is always aligned along a fixed direction in the body frame, regardless of the input $\boldsymbol{u}$, making it immune to uncertainties in the propeller spinning rates. Second, the direction of the force in the world frame can be reliably determined through simple attitude estimation and its derivative (using a gyroscope), enabling effective control via the fully actuated rotational dynamics. The only trade-off is underactuation, characterized by $\dim(\mathfrak{F}) = 1$, which, in many practical scenarios, has not posed significant limitations.

3.2 Tilted Quadrotors

Tilted quadrotors constitute a class of aerial vehicles distinguished by the inclination of their propeller axes relative to the main body frame. This configuration gives rise to the phenomenon of spurious force generation, which is central to the developments presented in this thesis and motivates their selection as a case study for our simulations. The following section, completely taken from the seminal work of Michieletto et al. [27], summarizes the key aspects relevant to our discussion.

Consider a system equipped with $n = 4$ identical propellers, each located at $\mathcal{O}_{P_i}$ and characterized by a spinning axis $\boldsymbol{z}_{P_i}$, where $i \in \mathcal{N} = \{1, 2, 3, 4\}$. The distance from the body center of mass $\mathcal{O}_B$ to the i-th propeller is denoted by l, assumed equal for all propellers. The spinning axis of each propeller is tilted by an angle α_i about the axis joining $\mathcal{O}_B$ and $\mathcal{O}_{P_i}$. The tilt angles are assigned such that consecutive rotors are oriented in opposite directions: specifically, $\alpha_1 = \alpha_3 = \alpha$ and $\alpha_2 = \alpha_4 = -\alpha$, with $\alpha \in [0, \frac{\pi}{2}]$.

Assuming uniform aerodynamic properties for all propellers, namely $c_{f_i} = c_f$ and $|c_{\tau_i}| = c_\tau$, and defining $s(\alpha) = \sin(\alpha)$, $c(\alpha) = \cos(\alpha)$, and $r = l(c_f/c_\tau)$, the force and torque allocation matrices $\boldsymbol{F}_1$ and $\boldsymbol{F}_2$ can be expressed as follows:

$$\boldsymbol{F}_1 = c_f \begin{bmatrix} 0 & s(\alpha) & 0 & -s(\alpha) \\ s(\alpha) & 0 & -s(\alpha) & 0 \\ c(\alpha) & c(\alpha) & c(\alpha) & c(\alpha) \end{bmatrix}, \tag{3.12}$$

$$\boldsymbol{F}_2 = c_\tau \begin{bmatrix} 0 & s(\alpha) + rc(\alpha) & 0 & -s(\alpha) - rc(\alpha) \\ -s(\alpha) - rc(\alpha) & 0 & s(\alpha) + rc(\alpha) & 0 \\ -c(\alpha) + rs(\alpha) & c(\alpha) - rs(\alpha) & -c(\alpha) + rs(\alpha) & c(\alpha) - rs(\alpha) \end{bmatrix}. \tag{3.13}$$

From (3.12), we observe the following properties of the force space $\mathfrak{F}$: if $s(\alpha) \neq 0$ and $c(\alpha) \neq 0$, then $\mathfrak{F} = \mathbb{R}^3$; if $s(\alpha) = 0$, then $\mathfrak{F} = \operatorname{span}\{\boldsymbol{e}_3\}$; and if $c(\alpha) = 0$, then $\mathfrak{F} = \operatorname{span}\{\boldsymbol{e}_1, \boldsymbol{e}_2\}$. Furthermore, the matrix $\boldsymbol{F}_2$ in (3.13) is full rank as long as $\tan(\alpha) \neq -r$ and $\tan(\alpha) \neq \frac{1}{r}$. If $\tan(\alpha) = \frac{1}{r}$ (i.e., $-c(\alpha) + rs(\alpha) = 0$), then $\operatorname{rank}(\boldsymbol{F}_2) = 2$; if $\tan(\alpha) = -r$ (i.e., $s(\alpha) + rc(\alpha) = 0$), then $\operatorname{rank}(\boldsymbol{F}_2) = 1$. When $\operatorname{rank}(\boldsymbol{F}_2) = 3$, the input space $\mathbb{R}^4$ can be partitioned as described in (3.3). By choosing a suitable transformation matrix $\boldsymbol{T}$, such as

$$\boldsymbol{T} = \begin{bmatrix} 0 & -1 & -1 & 1 \\ 1 & 0 & 1 & 1 \\ 0 & 1 & -1 & 1 \\ -1 & 0 & 1 & 1 \end{bmatrix},$$

we get

$$\boldsymbol{F}_1 \boldsymbol{T} = 2c_f \begin{bmatrix} s(\alpha) & 0 & 0 & 0 \\ 0 & -s(\alpha) & 0 & 0 \\ 0 & 0 & 0 & 2c(\alpha) \end{bmatrix}.$$

When $c(\alpha) = 0$, the generically tilted multirotor (GTM) is fully coupled (FC) because $\dim(\mathfrak{F}_B) = 0$. Conversely, as long as $c(\alpha) \neq 0$, we have $\dim(\mathfrak{F}_B) = 1$, meaning the GTM has a single decoupled direction (SD1), which corresponds to the direction $\boldsymbol{e}_3$. In this case, the platform is un-coupled (UC) if and only if $s(\alpha) = 0$, since only in this case $\mathfrak{F}_B = \mathfrak{F}$ (or equivalently, $\mathfrak{F}_A = \{\boldsymbol{0}\} \subseteq \mathfrak{F}_B$). Otherwise, when $s(\alpha) \neq 0$, the GTM is partially coupled (PC). The subspace $\mathfrak{F}_B^{\perp} \cap \mathfrak{F} = \operatorname{span}\{\boldsymbol{e}_1, \boldsymbol{e}_2\}$ represents the directions along which the projection of the control force depends entirely on the choice of the control moment. The purpose of this thesis it exactly to demonstrate the stability properties of a control law capable of mitigating these coupling effects.

Part III

Hovering and Control Strategies

Chapter 4

Static Hoverability Conditions

The formulation of the GTM model in (2.22) allows us to investigate the conditions under which it can maintain a controlled static equilibrium. Our ultimate goal is to provide a control law that enables a GTM to achieve static hovering and to rigorously prove its stability properties. However, since the precise definition of static hovering and the conditions under which a GTM can realize it are not immediately evident, the purpose of this chapter is to clarify these foundational aspects.

It is important to emphasize that the present chapter constitutes a synthesis and critical revision of concepts introduced in the cited works by Michieletto et al. [27, 26]. We restrict ourselves to extracting and adapting certain key notions that are instrumental for our objectives, while referring the interested reader to the original papers for a more comprehensive treatment.

We begin by defining the concept of static hover, a concept introduced in [26]:

Definition 4.1 (Static Hover, [26])**.** *A GTM platform, modeled by* (2.22)*, is said to be in static hover when its position and attitude are stably kept constant:*

$$(\boldsymbol{p}, \boldsymbol{v}, \boldsymbol{R}, \boldsymbol{\omega}) = (\mathbf{0}, \mathbf{0}, \boldsymbol{R}, \mathbf{0}).$$

The state $(\mathbf{0}, \mathbf{0}, \boldsymbol{R}, \mathbf{0})$ constitutes a locally stable forced equilibrium of the dynamics (2.22) for some attitude $\boldsymbol{R} \in \mathbf{SO}(3)$ and constant input $\boldsymbol{u} \in \mathbb{R}^n$. When the GTM platform is in static hover, it is rendered entirely safe with respect to its environment, as it exhibits neither translational nor rotational motion.

It is noteworthy, however, that the overwhelming majority of propellers employed in GTMs are engineered to rotate exclusively in a single direction. This restriction arises predominantly from the superior efficiency of propellers with asymmetric profiles, as well as the inherent technical challenges associated with achieving reliable and rapid reversal of their rotational direction. Consequently, it is imperative to incorporate this constraint into the model and to rigorously assess its ramifications.

To formalise this constraint, we adopt the notation $\boldsymbol{u} \in \mathcal{U}$ or $\boldsymbol{u} \in \mathcal{U}_+$, signifying that the input vector $\boldsymbol{u}$ is subject to the requirement that each component u_i is nonnegative or strictly positive, respectively. Adopting this new notation, our objective becomes to undertake a theoretical examination of the conditions under which a GTM may sustain a controlled static equilibrium, whilst adhering to the additional constraint $\boldsymbol{u} \in \mathcal{U}$.

An equivalent definition of static hover is provided in [27], expressed in terms of the equilibrium conditions of the GTM model (2.22). Specifically, the equilibrium is characterized by the following conditions:

$$\begin{cases} \dot{\boldsymbol{p}} = \boldsymbol{0}, \\ \ddot{\boldsymbol{p}} = \boldsymbol{0} \\ \boldsymbol{\omega} = \boldsymbol{0}, \\ \dot{\boldsymbol{\omega}} = \boldsymbol{0}. \end{cases} \iff \begin{cases} \dot{\boldsymbol{p}} = \boldsymbol{v} = \boldsymbol{0}, \\ \boldsymbol{f}_c = \boldsymbol{F}_1\boldsymbol{u} = mg\boldsymbol{R}^\top \boldsymbol{e}_3, \\ \boldsymbol{\omega} = \boldsymbol{0}, \\ \boldsymbol{\tau}_c = \boldsymbol{F}_2\boldsymbol{u} = \boldsymbol{0}. \end{cases} \tag{4.1}$$

Notably, the equilibrium conditions (4.1) require the ability to exert a control moment $\boldsymbol{\tau}_c$ in any direction and intensity, along with a control force $\boldsymbol{f}_c$, to ensure robust control of the GTM. This relies on the proper allocation of the input vector $\boldsymbol{u} \in \mathcal{U}$. To formalize this requirement, we recall Definition 4 and 5 from [27]:

Definition 4.2 (Realizability of any control moment, [27])**.** *A GTM can realize any control moment $\boldsymbol{\tau}_c \in \mathbb{R}^3$ if there exists a control input $\boldsymbol{u} \in \mathcal{U}$ such that $\boldsymbol{\tau}_c = \boldsymbol{F}_2\boldsymbol{u}$. Formally if*

$$\forall\, \boldsymbol{\tau}_c \in \mathbb{R}^3,\ \exists\, \boldsymbol{u} \in \mathcal{U} \ \text{ s.t. } \ \boldsymbol{\tau}_c = \boldsymbol{F}_2\boldsymbol{u}. \tag{4.2}$$

In [11], it has been shown that the aforementioned condition (4.2) is equivalent to the simultaneous satisfaction of (3.1) and the following condition:

$$\exists\, \boldsymbol{u} \in \mathcal{U}_+ \ \text{ s.t. } \ \boldsymbol{F}_2\boldsymbol{u} = \boldsymbol{0}. \tag{4.3}$$

Definition 4.3 (Realizability of any control force, [27])**.** *A GTM can realize any control force if it is possible to allocate the input vector $\boldsymbol{u} \in \mathcal{U}$ to obtain a control force with any intensity $f_c \in \mathbb{R}_{>0}$ while the platform is in static hovering. Formally if*

$$\forall\, f_c \in \mathbb{R}_{>0},\ \exists\, \boldsymbol{u} \in \mathcal{U} \ \text{ s.t. } \ \boldsymbol{F}_2\boldsymbol{u} = \boldsymbol{0} \ \text{ and } \ \|\boldsymbol{F}_1\boldsymbol{u}\| = f_c. \tag{4.4}$$

Note that the static hovering equilibrium (4.1) does not force the vehicle in a certain orientation. As a consequence, when it is possible to generate a control force with any nonnegative intensity, then it is sufficient to attain the suitable attitude (orientation) in order to realize any other control force vector.

We are now in a position to state a fundamental result originally presented as Proposition 1 in [27]:

Proposition 4.1 ([27])**.** *Condition* (4.4) *is equivalent to the following:*

$$\exists\, \boldsymbol{u} \in \mathcal{U} \ \text{ s.t. } \ \boldsymbol{F}_2\boldsymbol{u} = \boldsymbol{0} \ \text{ and } \ \boldsymbol{F}_1\boldsymbol{u} \neq \boldsymbol{0}. \tag{4.5}$$

Proof. We want to show that the conditions (4.4) and (4.5) are equivalent.

1. Suppose that $\overline{\boldsymbol{u}}$ satisfies (4.4). Then, $\boldsymbol{F}_2\overline{\boldsymbol{u}} = \boldsymbol{0}$ and $\|\boldsymbol{F}_1\overline{\boldsymbol{u}}\| = f_c$ for some $f_c \in \mathbb{R}_{>0}$. Since $f_c > 0$, we have that $\boldsymbol{F}_1\overline{\boldsymbol{u}} \neq \boldsymbol{0}$, which implies that $\overline{\boldsymbol{u}}$ satisfies (4.5).

2. Suppose that $\overline{\boldsymbol{u}}$ satisfies (4.5). Then, $\boldsymbol{F}_2\overline{\boldsymbol{u}} = \boldsymbol{0}$ and $\boldsymbol{F}_1\overline{\boldsymbol{u}} \neq \boldsymbol{0}$. Since $\boldsymbol{F}_1\overline{\boldsymbol{u}} \neq \boldsymbol{0}$, we have that $\|\boldsymbol{F}_1\overline{\boldsymbol{u}}\| \neq 0$. Therefore, $\forall f_c \in \mathbb{R}_{\geq 0}$, there exists $\boldsymbol{u} = \frac{f_c}{\|\boldsymbol{F}_1\overline{\boldsymbol{u}}\|}\overline{\boldsymbol{u}}$ satisfying (4.4).

$\square$

4.1 Prerequisites for Static Hoverability

This section establishes the conditions for a GTM to achieve static hovering while ensuring that the control input satisfies $\boldsymbol{u} \in \mathcal{U}$. To implement the virtual inputs $\boldsymbol{\tau}_c$ and $\boldsymbol{f}_c$ in accordance with the equilibrium conditions (4.1), the mappings $\boldsymbol{F}_1$ and $\boldsymbol{F}_2$ must be appropriately "inverted" by allocating $\boldsymbol{u} \in \mathcal{U}$ accordingly. We recall three prerequisites that guarantee the feasibility of static hovering, as introduced in [26].

The first requirement is the *full actuation of the orientation dynamics*, i.e., the system must be capable of generating any control moment $\boldsymbol{\tau}_c \in \mathbb{R}^3$. This is formalized in Definition 4.2 and is satisfied if (3.1) holds, ensuring that $\boldsymbol{F}_2$ has full rank, along with the additional constraint (4.3).

The second requirement is the *ability to independently regulate the magnitude of the control force* $\|\boldsymbol{f}_c\|$ without affecting the control moment $\boldsymbol{\tau}_c$. This property, captured in Definition 4.3, is met if and only if there exists at least a decoupled direction in the force space (D1), i.e., if rank $\left(\begin{bmatrix}\boldsymbol{F}_1^\top & \boldsymbol{F}_2^\top\end{bmatrix}\right) \geq 4$. Equivalently:

$$\exists\, \hat{\boldsymbol{b}} \in \ker(\boldsymbol{F}_2) \quad \text{s.t.} \quad \boldsymbol{F}_1 \hat{\boldsymbol{b}} \neq \boldsymbol{0}. \tag{4.6}$$

Choosing $\hat{\boldsymbol{u}} \in \ker(\boldsymbol{F}_2)$ ensures $\boldsymbol{\tau}_c = \boldsymbol{F}_2 \boldsymbol{u} = \boldsymbol{0}$, so (4.6) is equivalent to (4.5).

Building on these, we introduce Definition 6 from [27], which formalizes static hoverability for a GTM, encompassing both the necessary conditions for static hovering and the requirement that $\boldsymbol{u} \in \mathcal{U}$.

Definition 4.4 (Static Hovering Realizability, [27]). *A GTM is statically hoverable if it satisfies* (3.1)*,* (4.2)*, and* (4.4)*.*

Note that these are necessary conditions for equilibrium as defined in (4.1), but do not restrict the vehicle's orientation. Achieving a forced equilibrium requires a specific direction of the control force, which can only be realized by managing the GTM's attitude. Thus, among all possible attitudes, only those that allow satisfaction of (4.1) are admissible.

As illustrated in Fig. (2.2), the angular velocity $\boldsymbol{\omega}$ influences the rotation matrix $\boldsymbol{R}$, which affects the translational velocity $\boldsymbol{v}$ and, ultimately, the position $\boldsymbol{p}$. This sequential dependency classifies GTMs as cascaded dynamical systems, a structure often leveraged in control design. Typically, $\boldsymbol{\omega}$ and $\boldsymbol{R}$ are stabilized via $\boldsymbol{\tau}_c$ in an inner loop, independently of the translational dynamics, toward a desired attitude $\boldsymbol{R}_d$. In an outer loop, $\boldsymbol{R}_d$ and $\boldsymbol{f}_c$ are then used to regulate $\boldsymbol{v}$ and $\boldsymbol{p}$.

We thus seek a control input $\boldsymbol{u} \in \mathcal{U}$ such that $\hat{\boldsymbol{u}} \in \ker(\boldsymbol{F}_2)$ and $\boldsymbol{R}\boldsymbol{F}_1\boldsymbol{u} = mg\boldsymbol{e}_3$. Both requirements are satisfied by setting

$$\boldsymbol{u} = \delta \hat{\boldsymbol{b}}, \quad \text{with} \quad \delta = \frac{mg}{\|\boldsymbol{F}_1 \hat{\boldsymbol{b}}\|}, \tag{4.7}$$

where $\hat{\boldsymbol{b}} \in \ker(\boldsymbol{F}_2)$. The attitude $\boldsymbol{R}$ must then be chosen so that $\boldsymbol{R}\boldsymbol{F}_1\hat{\boldsymbol{b}} \propto \boldsymbol{e}_3$, aligning the thrust direction with the required force vector.

This imposes a geometric constraint, defining a line in the input space along which $\boldsymbol{u}$ must lie to maintain hovering. The precise operating point depends on the GTM's mass m and the configuration of the propellers, which determine $\boldsymbol{F}_1$

and $\boldsymbol{F}_2$. Specifically, $\boldsymbol{F}_1$ determines $\|\boldsymbol{F}_1\hat{\boldsymbol{b}}\|$, while $\boldsymbol{F}_2$ influences the condition via $\hat{\boldsymbol{b}} \in \ker(\boldsymbol{F}_2)$[1].

The third prerequisite concerns *input saturation.* To maintain hovering equilibrium, $\boldsymbol{u}$ must belong to the admissible set $\mathcal{U} = \mathcal{U}_1 \times \cdots \times \mathcal{U}_n$, with $\boldsymbol{u}_i \in \mathcal{U}_i$ for all $i \in \mathcal{N}$. However, feasibility alone is not sufficient: the hovering point must allow some operational margin within $\mathcal{U}$ to ensure maneuverability for attitude and position regulation.

To address this, we introduce a conservative subset $\mathcal{H} = \mathcal{H}_1 \times \cdots \times \mathcal{H}_n$, with $\mathcal{H}_i \subset \mathcal{U}_i$ for all $i \in \mathcal{N}$, defining a safety margin. The equilibrium command must therefore satisfy

$$\delta\hat{\boldsymbol{b}} \in \mathcal{H}. \tag{4.8}$$

This ensures the equilibrium input is not too close to actuator limits, preserving the ability to apply necessary control variations.

The three prerequisites for static hoverability are summarized in the following proposition, adapted from [26]:

Proposition 4.2 (Static Hoverability Condition (SHC), [26]). *A GTM is statically hoverable if the following conditions are satisfied:*

1. $\operatorname{rank}(\boldsymbol{F}_2) = 3$,
2. $\exists\, \hat{\boldsymbol{b}} \in \ker(\boldsymbol{F}_2)$ *s.t.* :
   - 2.1. $\boldsymbol{F}_1\hat{\boldsymbol{b}} \neq \boldsymbol{0}$,
   - 2.2. $\delta = \frac{mg}{\|\boldsymbol{F}_1\hat{\boldsymbol{b}}\|}$, *with* $\delta\hat{\boldsymbol{b}} \in \mathcal{H}$.

Finally, we present Proposition 4 from [27], which provides a possible choice for the decoupled direction in the force space.

Proposition 4.3 ([27]). *A statically hoverable GTM has a decoupled direction in the force space. In particular, for any* $\tilde{\mathbf{u}} \in \mathcal{H}$ *satisfying Proposition 4.2, a possible choice for the decoupled direction is*

$$\boldsymbol{d}_\star = \frac{\boldsymbol{F}_1\tilde{\boldsymbol{u}}}{\|\boldsymbol{F}_1\tilde{\boldsymbol{u}}\|}. \tag{4.9}$$

The preferential direction $\boldsymbol{d}_\star$ is a unit vector in the body frame $\mathcal{F}_B$, determined solely by the platform's characteristics, such as propeller arrangement and rotor properties. It is thus a typical feature of the GTM, independent of the specific hovering configuration.

Proof. Let $\tilde{\mathbf{u}} \in \mathcal{H}$ satisfy Proposition 4.2. In particular,

$$\tilde{\mathbf{u}} \in \ker(\mathbf{F}_2), \quad \mathbf{F}_1\,\tilde{\mathbf{u}} \neq \mathbf{0}.$$

Since $\tilde{\mathbf{u}} \in \ker(\mathbf{F}_2)$,

$$\mathbf{F}_2\,\tilde{\mathbf{u}} = \mathbf{0},$$

---

[1] Although $\boldsymbol{F}_2$ has full rank, $\dim(\ker(\boldsymbol{F}_2))$ is not necessarily zero. For $\boldsymbol{F}_2$ of size $3 \times n$ with $n \geq 3$, $\dim(\ker(\boldsymbol{F}_2)) \geq n - 3$.

i.e., no control moment is generated. On the other hand, $\mathbf{F}_1 \tilde{\mathbf{u}} \neq \mathbf{0}$ guarantees a nonzero control force.

By construction, $\mathbf{d}_\star$ in (4.9) is a unit vector in $\mathcal{F}_B$. Moreover, since $\tilde{\mathbf{u}}$ lies in the kernel of $\mathbf{F}_2$, any scaling of $\mathbf{F}_1 \tilde{\mathbf{u}}$ along this direction does not induce a control moment. Hence, $\mathbf{d}_\star$ yields the desired decoupled direction in force space, concluding the proof. □

A direct consequence of Proposition 4.2 is stated in Proposition 1 from [26], which is restated here for clarity:

Proposition 4.4 ([26])**.** *A GTM can be statically hoverable only if* $|\mathcal{C}| \geq 4$.

The following proof is an original and rigorous argument establishing the necessity of $|\mathcal{C}| \geq 4$ for static hoverability. While it may differ in style from those found in the literature, it provides a clear and formal justification for this requirement.

Proof. We aim to show that the condition $|\mathcal{C}| \geq 4$ is necessary for the existence of a set of rotors $\mathcal{C}$ such that the prerequisites of Proposition 4.2 are satisfied.

Suppose, for contradiction, that the set of controllable rotors $\mathcal{C}$ satisfies

$$0 < |\mathcal{C}| = k < 4$$

and yet the system is statically hoverable as per Proposition 4.2. Under this assumption, the input control vector can be written as

$$\boldsymbol{u}_i = \begin{cases} \boldsymbol{u}_i^\star, & i \in \mathcal{N} \setminus \mathcal{C}, \\ \star, & i \in \mathcal{C}, \end{cases}$$

and therefore can be partitioned as

$$\mathbf{u} = \underbrace{\mathbf{u}_{\mathcal{N}\setminus\mathcal{C}}}_{\text{fixed}=\mathbf{u}^\star} \oplus \underbrace{\mathbf{u}_{\mathcal{C}}}_{\text{free, dimension } k} .$$

Let $\boldsymbol{F}$ be the $6 \times n$ control allocation matrix with $\operatorname{rank}(\boldsymbol{F}) \geq 4$. Since only the k components in $\mathbf{u}_{\mathcal{C}}$ may vary, the space of attainable force-moment vectors

$$\mathbf{F}\,\mathbf{u} \;=\; \mathbf{F}_{\mathcal{N}\setminus\mathcal{C}}\,\mathbf{u}^\star \;+\; \mathbf{F}_{\mathcal{C}}\,\mathbf{u}_{\mathcal{C}}$$

is an affine subspace whose direction space equals $\operatorname{Im}(\mathbf{F}_{\mathcal{C}})$, with

$$\dim\Big(\operatorname{Im}(\mathbf{F}_{\mathcal{C}})\Big) \;\leq\; \min\{6, k\} \;=\; k < 4.$$

In other words, regardless of the variations in the k independent inputs, the resulting space can only cover a k-dimensional portion of the full 6-dimensional force-moment space. However, achieving static hoverability requires the ability to cover a subspace of at least four dimensions (three for the control moment and one for the control force). Therefore, it is necessary that

$$\dim\Big(\operatorname{Im}(\mathbf{F}_{\mathcal{C}})\Big) \;\geq\; 4,$$

which contradicts $k < 4$. Therefore, necessarily $|\mathcal{C}| \geq 4$. □

Chapter 5

Hover Control Strategy

In this chapter, we present a hierarchical control strategy for maintaining a generically tilted multirotor (GTM) in static hover, even in the presence of spurious forces. The control law is suggested by Michieletto et al. in [26], which can be consulted for a more detailed explanation.

We begin by defining the class of GTMs under consideration and outlining the specific control objectives, namely, achieving and maintaining static hover. Subsequently, we detail the hierarchical control architecture, emphasizing its ability to mitigate the effects of spurious forces, which are forces that arise when the reference control moment is implemented while simultaneously affecting the platform's translational dynamics.

5.1 Platforms Class Definition

In this section, we formally recall the class of aerial platforms already identified and discussed in the previous chapter. Here, we simply summarize the key conditions that characterize this class and that must be kept in mind for the analyses and control results developed in the following chapters. In particular, we are considering platforms whose dynamics are given by (2.22) and enjoy the following properties:

- The number of propellers satisfies $n \geq 4$. As shown in Proposition 4.4, this condition is necessary to guarantee the possibility of static hovering.
- The control moment input matrix $\boldsymbol{F}_2$ in (2.16) associated with the platform satisfies the rank condition $\text{rank}(\boldsymbol{F}_2) = 3$, as already discussed in (3.1).
- It is possible to independently regulate the control force component along at least one direction, as formalized in (4.6). In matrix terms, the control force input matrix $\boldsymbol{F}_1$ in (2.14) must satisfy

$$\text{rank}\left(\begin{bmatrix}\boldsymbol{F}_1\\ \boldsymbol{F}_2\end{bmatrix}\right) \geq 4.$$

In the following, we will therefore restrict our attention to platforms that satisfy these properties, as they guarantee the existence of a preferential direction, which is crucial for the development of the control strategies and theoretical results presented in the following.

5.2 Control Objective

The primary objective is to regulate the platform to a prescribed constant reference position $\boldsymbol{p}_r \in \mathbb{R}^3$ and to achieve an orientation that closely approximates a given constant reference rotation matrix $\boldsymbol{R}_r \in \mathbf{SO}(3)$. Formally, the control problem consists in designing an admissible control input $\boldsymbol{u}_r \in \mathcal{U} \subseteq \mathbb{R}^n$ such that

$$\lim_{t\to\infty} \boldsymbol{p}(t) = \boldsymbol{p}_r, \qquad \lim_{t\to\infty} \boldsymbol{R}(t) = \boldsymbol{R}_r.$$

The class of vehicles under consideration is actuated through a control force $\boldsymbol{f}_c = \boldsymbol{F}_1\boldsymbol{u}$, governing the translational dynamics and steering the platform toward $\boldsymbol{p}_r$, and a control moment $\boldsymbol{\tau}_c = \boldsymbol{F}_2\boldsymbol{u}$, responsible for the attitude dynamics and reorienting the platform toward $\boldsymbol{R}_r$.

A critical aspect arises from the requirement that the thrust direction $\hat{\boldsymbol{f}}_c$ must be aligned with the direction of the resultant force necessary to accomplish the translational objective. If the user-specified reference orientation $\boldsymbol{R}_r$ does not ensure this alignment, the translational control objective cannot be fulfilled. To address this, we introduce a modified reference orientation $\boldsymbol{R}_d(t)$, which balances the need to track the desired attitude while guaranteeing that the thrust direction is compatible with the required force vector. Consequently, the control objective is reformulated as

$$\lim_{t\to\infty} \boldsymbol{p}(t) = \boldsymbol{p}_r, \qquad \lim_{t\to\infty} \boldsymbol{R}(t) = \boldsymbol{R}_d(t), \tag{5.1}$$

where the construction of the desired rotation matrix $\boldsymbol{R}_d(t)$ will be detailed in the following section.

5.3 Hover Control Strategy

The hierarchical control strategy proposed in [26] consisting of two loops: an outer, slower loop for translational dynamics, which computes the reference control force $\boldsymbol{f}_r$ to solve the command in translation, and an inner, faster loop for attitude dynamics, which computes the reference control moment $\boldsymbol{\tau}_r$ to execute the command in orientation. The reference control input $\boldsymbol{u}_r$ is then determined by a wrench mapper, ensuring that $\boldsymbol{\tau}_c = \boldsymbol{F}_2\boldsymbol{u}_r = \boldsymbol{\tau}_r$ and that, at least, the projection of the control force $\boldsymbol{f}_c = \boldsymbol{F}_1\boldsymbol{u}_r$ along a specific direction matches the magnitude of the reference control force $\boldsymbol{f}_r$. In Fig. 5.1, we provide a schematic representation of the hierarchical control structure.

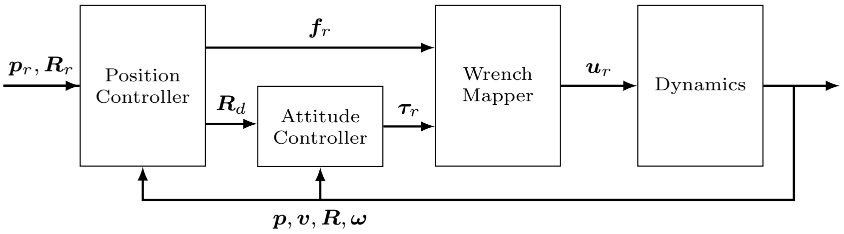

Figure 5.1. Hierarchical control structure for a GTM.

The core idea of the suggested controller is to prioritize attitude control, treating the desired rotation matrix $\boldsymbol{R}_d$ as an additional control input to ensure that the thrust direction aligns with the desired one. Once the attitude is stabilized, the translational dynamics are controlled by adjusting the thrust magnitude, keeping the platform at the desired position $\boldsymbol{p}_r$ while maintaining an attitude close to $\boldsymbol{R}_r$, specifically $\boldsymbol{R}_d$.

A key feature of this strategy is to find a preferential direction in the force space, $\boldsymbol{d}_\star \in \operatorname{Im}(\boldsymbol{F}_1)$, along which the control force $\boldsymbol{f}_c$ can be adjusted independently of the control moment $\boldsymbol{\tau}_c$. This requires finding a unitary vector $\boldsymbol{d}_\star$ that satisfies the rank condition

$$\operatorname{rank}\left(\begin{bmatrix}\boldsymbol{F}_1^\top \boldsymbol{d}_\star & \boldsymbol{F}_2^\top\end{bmatrix}\right) \geq 4.$$

If this condition holds, the term $\boldsymbol{d}_\star^\top \boldsymbol{F}_1 \boldsymbol{u}_r$ can be freely chosen, while ensuring that $\boldsymbol{F}_2 \boldsymbol{u}_r = \boldsymbol{\tau}_r$. Assuming the Static Hovering Conditions (SHCs) from Proposition 4.2 are met, a suitable choice for $\boldsymbol{d}_\star$ is given by

$$\boldsymbol{d}_\star = \frac{\boldsymbol{F}_1 \hat{\boldsymbol{b}}}{\|\boldsymbol{F}_1 \hat{\boldsymbol{b}}\|}, \tag{5.2}$$

where $\hat{\boldsymbol{b}}$ is the unit vector defined in the same Proposition. Among the possible choices for $\boldsymbol{u}$, we select the one that lies along $\hat{\boldsymbol{b}}$ so that

$$\hat{\boldsymbol{f}}_c = \frac{\boldsymbol{F}_1 \hat{\boldsymbol{u}}}{\|\boldsymbol{F}_1 \hat{\boldsymbol{u}}\|} = \frac{\boldsymbol{F}_1 \hat{\boldsymbol{b}}}{\|\boldsymbol{F}_1 \hat{\boldsymbol{b}}\|} = \boldsymbol{d}_\star.$$

Thus, the direction of the control force $\boldsymbol{f}_c$ coincides with the preferential direction $\boldsymbol{d}_\star$. This choice decouples the magnitude of the control force from the control moment.

In summary, the attitude controller generates a reference control moment $\boldsymbol{\tau}_r$ that ensures

$$\lim_{\boldsymbol{R} \to \boldsymbol{R}_d} \boldsymbol{R} \hat{\boldsymbol{f}}_c = \hat{\boldsymbol{f}}_r,$$

specifically, rotates the platform so that the thrust direction $\boldsymbol{R}\hat{\boldsymbol{f}}_c = \boldsymbol{R}\boldsymbol{d}_\star$ aligns with the direction of the reference control force $\hat{\boldsymbol{f}}_r$. Once this alignment is achieved, the magnitude of $\boldsymbol{f}_c$ can be adjusted independently of the implementation of $\boldsymbol{\tau}_r$, ensuring that both the magnitude and direction of $\boldsymbol{f}_c$ match those of $\boldsymbol{f}_r$.

In the following, we provide a detailed description of the position and attitude controllers, as well as the wrench mapper.

5.3.1 Position Controller

Given a reference position $\boldsymbol{p}_r \in \mathbb{R}^3$ and a reference rotation matrix $\boldsymbol{R}_r \in \mathbf{SO}(3)$, the position controller generates a reference control force $\boldsymbol{f}_r \in \mathbb{R}^3$ and a desired rotation matrix $\boldsymbol{R}_d \in \mathbf{SO}(3)$.

It is designed to regulate the translational dynamics of the GTM, ensuring that the platform's position $\boldsymbol{p}$ converges to the desired position $\boldsymbol{p}_r$ and that the velocity $\dot{\boldsymbol{p}}$ converges to zero. The translational task can be summarized as follows

$$\lim_{t \to \infty} (\boldsymbol{p}(t), \dot{\boldsymbol{p}}(t), \ddot{\boldsymbol{p}}(t)) = (\boldsymbol{p}_r, \boldsymbol{0}, \boldsymbol{0}), \tag{5.3}$$

Formally, let $\boldsymbol{e}_p := \boldsymbol{p} - \boldsymbol{p}_r$ be the position error and $\boldsymbol{v} := \dot{\boldsymbol{p}}$ be the velocity of the platform, the reference control force is designed in such a way that $(\boldsymbol{e}_p, \boldsymbol{v}, \dot{\boldsymbol{v}}) \to (\boldsymbol{0}, \boldsymbol{0}, \boldsymbol{0})$, namely

$$\boldsymbol{f}_r = -\boldsymbol{K}_p \boldsymbol{e}_p - \boldsymbol{K}_v \boldsymbol{v} + mg\boldsymbol{e}_3, \tag{5.4}$$

where $\boldsymbol{K}_p, \boldsymbol{K}_v \in \mathbb{R}^{3\times 3}$ are positive definite matrices and allow to tune the effect of the position tracking error and the velocity feedback term, respectively. This formulation combines a PD controller with a gravity compensation term.

The role of the position controller is also to provide the desired rotation matrix $\boldsymbol{R}_d$, computed by combining two rotations

- A rotation $\boldsymbol{R}_b$ that rotates the preferential direction $\boldsymbol{d}_\star$ with $\boldsymbol{e}_3$. This is achieved by exploiting the Rodrigues' rotation formula:

  $$\boldsymbol{R}_b = \left[\boldsymbol{r}\boldsymbol{r}^\top + (\boldsymbol{I}_3 - \boldsymbol{r}\boldsymbol{r}^\top)\cos(\theta_{\min}) + \boldsymbol{S}(\boldsymbol{r})\sin(\theta_{\min})\right],$$

  where $\boldsymbol{r} = \boldsymbol{d}_\star \times \boldsymbol{e}_3$ and $\theta_{\min}$ is the minimum angle between $\boldsymbol{d}_\star$ and $\boldsymbol{e}_3$, i.e.,

  $$\theta_{\min} = \min(\theta, \pi - \theta), \quad \theta = \arccos(\langle \boldsymbol{d}_\star, \boldsymbol{e}_3 \rangle).$$

  In conclusion, the rotation $\boldsymbol{R}_b$ is such that $\boldsymbol{R}_b \boldsymbol{d}_\star = \boldsymbol{e}_3$.

- A rotation $\boldsymbol{R}_w$ that aligns the the unit vector $\boldsymbol{e}_3$ to $\hat{\boldsymbol{f}}_r$:

  $$\boldsymbol{R}_w = \begin{bmatrix}(\boldsymbol{w}_3 \times \boldsymbol{w}_1) \times \boldsymbol{w}_3 & \boldsymbol{w}_3 \times \boldsymbol{w}_1 & \boldsymbol{w}_3\end{bmatrix}, \tag{5.5}$$

  where $\boldsymbol{w}_1 := \boldsymbol{R}_r \boldsymbol{e}_1$, i.e., is the first column of $\boldsymbol{R}_r$ and $\boldsymbol{w}_3 = \hat{\boldsymbol{f}}_r$. Therefore, the rotation $\boldsymbol{R}_w$ is such that $\boldsymbol{R}_w \boldsymbol{e}_3 := \hat{\boldsymbol{f}}_r$, i.e., is the reference force direction.

The desired orientation matrix is then computed as

$$\boldsymbol{R}_d = \boldsymbol{R}_w \boldsymbol{R}_b, \tag{5.6}$$

and it is such that $\hat{\boldsymbol{f}}_r = \boldsymbol{R}_d \boldsymbol{d}_\star$.

5.3.2 Attitude Controller

Given a desired rotation matrix $\boldsymbol{R}_d \in \mathbf{SO}(3)$, the attitude controller generates a reference control moment $\boldsymbol{\tau}_r \in \mathbb{R}^3$. The latter is designed to ensure that the platform's orientation $\boldsymbol{R}$ tracks the desired orientation $\boldsymbol{R}_d$, and that the angular velocity $\boldsymbol{\omega}$ converges to zero. The control objective is formally stated as

$$\lim_{t\to\infty} (\boldsymbol{R}(t), \boldsymbol{\omega}(t), \dot{\boldsymbol{\omega}}(t)) = (\boldsymbol{R}_d(t), \boldsymbol{0}, \boldsymbol{0}). \tag{5.7}$$

To achieve this, we define the attitude tracking errors. The orientation tracking error $\boldsymbol{e}_R$ quantifies the discrepancy between the current orientation $\boldsymbol{R}$ and the desired orientation $\boldsymbol{R}_d$. This is evaluated via the following attitude error function on the tangent bundle of $\mathbf{SO}(3)$:

$$\Psi(\boldsymbol{R}, \boldsymbol{R}_d) = \frac{1}{2}\mathrm{Tr}\left[\boldsymbol{I}_3 - \boldsymbol{R}_d^\top \boldsymbol{R}\right]. \tag{5.8}$$

This function is positive-definite on $\mathbf{SO}(3) \times \mathbf{SO}(3)$, vanishing if and only if $\boldsymbol{R} = \boldsymbol{R}_d$, and is locally positive-definite in the region where the rotation angle between $\boldsymbol{R}$ and $\boldsymbol{R}_d$ is less than π radians. This set can be represented by the sublevel set of Ψ where $\Psi < 2$, denoted as $L_2 = \{\boldsymbol{R}_d, \boldsymbol{R} \in SO(3) : \Psi(\boldsymbol{R}, \boldsymbol{R}_d) < 2\}$, which almost covers the entire $\mathbf{SO}(3)$ manifold.

If the variation in $\boldsymbol{R}$ is expressed as $\boldsymbol{R}\boldsymbol{S}(\boldsymbol{\eta})$ for $\boldsymbol{\eta} \in \mathbb{R}^3$, the time derivative of Ψ is

$$\frac{d}{dt}\Psi(\boldsymbol{R}, \boldsymbol{R}_d) = -\frac{1}{2}\mathrm{Tr}\big[\boldsymbol{R}_d^\top \boldsymbol{R}\boldsymbol{S}(\boldsymbol{\eta})\big].$$

Using the property $-\frac{1}{2}\mathrm{Tr}\big[\boldsymbol{S}(\boldsymbol{x})\boldsymbol{S}(\boldsymbol{y})\big] = \boldsymbol{x}^\top \boldsymbol{y}$ for any $\boldsymbol{x}, \boldsymbol{y} \in \mathbb{R}^3$, and applying the inverse of the skew-symmetric map $\boldsymbol{S}^{-1}(\cdot)$, we obtain

$$-\frac{1}{2}\mathrm{Tr}\big[\boldsymbol{R}_d^\top \boldsymbol{R}\boldsymbol{S}(\boldsymbol{\eta})\big] = \frac{1}{2}\boldsymbol{S}^{-1}(\boldsymbol{R}_d^\top \boldsymbol{R} - \boldsymbol{R}^\top \boldsymbol{R}_d)\boldsymbol{\eta}.$$

Thus, the derivative of Ψ becomes

$$\frac{d}{dt}\Psi(\boldsymbol{R}, \boldsymbol{R}_d) = \frac{1}{2}\boldsymbol{S}^{-1}(\boldsymbol{R}_d^\top \boldsymbol{R} - \boldsymbol{R}^\top \boldsymbol{R}_d)\boldsymbol{\eta}.$$

From this, we define the attitude tracking error as

$$\boldsymbol{e}_R = \frac{1}{2}\boldsymbol{S}^{-1}(\boldsymbol{R}_d^\top \boldsymbol{R} - \boldsymbol{R}^\top \boldsymbol{R}_d). \tag{5.9}$$

This formulation rigorously captures the discrepancy between $\boldsymbol{R}$ and $\boldsymbol{R}_d$ while respecting the geometric structure of $\mathbf{SO}(3)$.

When the desired attitude $\boldsymbol{R}_d(t)$ is time-varying, a corresponding desired angular velocity $\boldsymbol{\omega}_d(t)$ arises, leading to the instantaneous angular velocity tracking error $\boldsymbol{e}_\omega = \boldsymbol{\omega} - \boldsymbol{R}^\top \boldsymbol{R}_d\,\boldsymbol{\omega}_d$ as defined in (C.7).

It is desirable that both $\boldsymbol{e}_\omega$ and the attitude error (5.9) converge to zero. Rather than compensating $\boldsymbol{\omega}_d$ explicitly, we adopt the approach proposed in [26], which ensures convergence of both $\boldsymbol{e}_R$ and $\boldsymbol{\omega}$. Accordingly, to guarantee that $(\boldsymbol{e}_R, \boldsymbol{\omega}, \dot{\boldsymbol{\omega}}) \to (\mathbf{0}, \mathbf{0}, \mathbf{0})$, the attitude control block provides the following reference control moment:

$$\boldsymbol{\tau}_r = \boldsymbol{\omega} \times \boldsymbol{J}\boldsymbol{\omega} - \boldsymbol{K}_R\boldsymbol{e}_R - \boldsymbol{K}_\omega\boldsymbol{\omega}, \tag{5.10}$$

where $\boldsymbol{K}_R, \boldsymbol{K}_\omega \in \mathbb{R}^{3\times 3}$ are positive definite matrices, allowing for the tuning of the rotation tracking error and angular velocity feedback terms, respectively.

5.3.3 Wrench Mapper

The Wrench Mapper is a fundamental component of the control architecture, responsible for converting the reference commands into the corresponding spinning rates of the actuators. Specifically, given the reference control wrench

$$\boldsymbol{w}_r = \begin{bmatrix} \boldsymbol{R}^\top \boldsymbol{f}_r \\ \boldsymbol{\tau}_r \end{bmatrix} \in \mathbb{R}^6, \tag{5.11}$$

where $\boldsymbol{f}_r$ is the reference control force in (5.4) and $\boldsymbol{\tau}_r$ is the reference control moment in (5.10), the Wrench Mapper computes the associated reference control input $\boldsymbol{u}_r$.

The capability of the GTM to faithfully reproduce the reference control wrench is contingent upon the actuation system's ability to generate the required control force and moment.

To determine the reference control input that achieves the reference control wrench in (5.11), we refer to the dynamic model of the multirotor provided in (2.22) and we utilize the input transformation specified in (3.4). Upon applying the transformation $\boldsymbol{T}$ to the control input, it can be represented as

$$\boldsymbol{u}_r = \boldsymbol{u}_\tau + \boldsymbol{u}_f, \tag{5.12}$$

where $\boldsymbol{u}_\tau \coloneqq \boldsymbol{A}_2\tilde{\boldsymbol{u}}_A$ and $\boldsymbol{u}_f \coloneqq \boldsymbol{B}_2\tilde{\boldsymbol{u}}_B$ are the control inputs associated with the control moment and control force, respectively.

Substituting this control input into the dynamic model yields the following equations

$$\begin{bmatrix} m\ddot{\boldsymbol{p}} \\ \boldsymbol{J}\dot{\boldsymbol{\omega}} \end{bmatrix} = -\begin{bmatrix} mg\boldsymbol{e}_3 \\ \boldsymbol{\omega} \times J\boldsymbol{\omega} \end{bmatrix} + \begin{bmatrix} \boldsymbol{R}\boldsymbol{F}_1(\boldsymbol{u}_\tau + \boldsymbol{u}_f) \\ \boldsymbol{F}_2\boldsymbol{u}_\tau \end{bmatrix}, \tag{5.13}$$

where the properties of the transformation matrix $\boldsymbol{T}$ in (3.3) have been utilized.

Regarding the design of the reference control input, we give priority to the implementation of the control moment $\boldsymbol{\tau}_r$ in (5.10) and then, with the remaining actuators, we will deal with the control force $\boldsymbol{f}_c$ so that it can be as similar as possible to the reference control force $\boldsymbol{f}_r$ in (5.4). Specifically, $\boldsymbol{u}_\tau$ represents the segment of the reference control input that will be used to completely realize the reference control torque

$$\boldsymbol{u}_\tau = \boldsymbol{F}_2^\dagger\boldsymbol{\tau}_r, \tag{5.14}$$

where $\boldsymbol{F}_2^\dagger$ represents the pseudoinverse of the $\boldsymbol{F}_2$ matrix, while $\boldsymbol{u}_f$ denotes the portion of the reference control input that will be allocated to approximate the reference control force as closely as possible. To this end, it is necessary to identify a suitable segment $\boldsymbol{u}_f$ within the input space that will allow the control force $\boldsymbol{R}\boldsymbol{F}_1\boldsymbol{u}_r$ to approximate the reference control force $\boldsymbol{f}_r$ as well as possible.

By virtue of the input transformation applied earlier, the vector $\boldsymbol{u}_f$ has to be in the null space of matrix $\boldsymbol{F}_2$, and, at the same time, it has to belong in the column space of matrix $\boldsymbol{F}_1^\top$. This leads to selecting $\boldsymbol{u}_f$ as

$$\boldsymbol{u}_f = \hat{\boldsymbol{b}}c, \tag{5.15}$$

where $\hat{\boldsymbol{b}} \in \mathbb{R}^n$ is a unit vector defined in Proposition 4.2, and $c \in \mathbb{R}$ is a scaling factor obtained by solving the optimization problem

$$c = \arg\min_{c\in\mathbb{R}} \left\| \boldsymbol{R}\boldsymbol{F}_1\boldsymbol{b}c - \left(\boldsymbol{f}_r - \boldsymbol{R}\boldsymbol{F}_1\boldsymbol{F}_2^\dagger\boldsymbol{\tau}_r\right)\right\|^2. \tag{5.16}$$

A closed-form solution to this optimization problem exists and is given by

$$c = \frac{\left(\boldsymbol{f}_r - \boldsymbol{R}\boldsymbol{F}_1\boldsymbol{F}_2^\dagger\boldsymbol{\tau}_r\right)^\top \boldsymbol{R}\boldsymbol{d}_\star}{\|\boldsymbol{F}_1\boldsymbol{b}\|}, \tag{5.17}$$

where this expression is obtained by recalling the preferential direction $\boldsymbol{d}_\star$ defined in (5.2), and noting that the rotation matrix $\boldsymbol{R}$ modifies only the attitude of a vector, leaving its magnitude unchanged.

Finally, note that the reference control input $\boldsymbol{u}_r$ remains feasible, at least in a neighborhood of the equilibrium, because the commands at equilibrium are designed to lie well inside the feasible set, as ensured by the third prerequisite in Proposition 4.2.

The attitude closed-loop dynamics are given by

$$\boldsymbol{J}\dot{\boldsymbol{\omega}} = -\boldsymbol{\omega} \times \boldsymbol{J}\boldsymbol{\omega} + \boldsymbol{\tau}_r, \tag{5.18}$$

where the reference control moment $\boldsymbol{\tau}_r$ is computed in (5.10). Indeed, the translational closed-loop dynamics are given by

$$m\ddot{\boldsymbol{p}} = -mg\boldsymbol{e}_3 + \boldsymbol{R}\boldsymbol{F}_1\boldsymbol{u}_r,$$

where the term $\boldsymbol{R}\boldsymbol{F}_1\boldsymbol{u}_r$ can be rewritten as

$$\begin{aligned}
\boldsymbol{R}\boldsymbol{F}_1\boldsymbol{u}_r =& \boldsymbol{R}\boldsymbol{F}_1\left(\boldsymbol{F}_2^\dagger\boldsymbol{\tau}_r + \boldsymbol{b}\frac{\left(\boldsymbol{f}_r - \boldsymbol{R}\boldsymbol{F}_1\boldsymbol{F}_2^\dagger\boldsymbol{\tau}_r\right)^\top \boldsymbol{R}\boldsymbol{d}_\star}{\|\boldsymbol{F}_1\boldsymbol{b}\|}\right) \\
&= \boldsymbol{R}\boldsymbol{F}_1\boldsymbol{F}_2^\dagger\boldsymbol{\tau}_r + \boldsymbol{R}\boldsymbol{d}_\star\left(\boldsymbol{f}_r - \boldsymbol{R}\boldsymbol{F}_1\boldsymbol{F}_2^\dagger\boldsymbol{\tau}_r\right)^\top \boldsymbol{R}\boldsymbol{d}_\star \\
&= \boldsymbol{R}\boldsymbol{d}_\star\left(\boldsymbol{R}\boldsymbol{d}_\star\right)^\top \boldsymbol{f}_r + \left[\boldsymbol{I}_3 - \boldsymbol{R}\boldsymbol{d}_\star\left(\boldsymbol{R}\boldsymbol{d}_\star\right)^\top\right]\boldsymbol{R}\boldsymbol{F}_1\boldsymbol{F}_2^\dagger\boldsymbol{\tau}_r.
\end{aligned}$$

Let $\boldsymbol{P}_\star \coloneqq \boldsymbol{R}\boldsymbol{d}_\star\left(\boldsymbol{R}\boldsymbol{d}_\star\right)^\top$ be the projection matrix onto the preferential direction, we can rewrite the translational closed-loop dynamics as

$$m\ddot{\boldsymbol{p}} = -mg\boldsymbol{e}_3 + \boldsymbol{P}_\star\boldsymbol{f}_r + \boldsymbol{P}_\star^\perp\boldsymbol{R}\boldsymbol{F}_1\boldsymbol{F}_2^\dagger\boldsymbol{\tau}_r.$$

Since the reference control force can be written as $\boldsymbol{f}_r = \|\boldsymbol{f}_r\|\boldsymbol{R}_d\boldsymbol{d}_\star$, the translational dynamics can be further simplified by adding and subtracting the term $\boldsymbol{f}_r$ in the equation above, yielding

$$\begin{aligned}
m\ddot{\boldsymbol{p}} &= -mg\boldsymbol{e}_3 + \boldsymbol{P}_\star\boldsymbol{f}_r + \boldsymbol{f}_r - \boldsymbol{f}_r + \boldsymbol{P}_\star^\perp\boldsymbol{R}\boldsymbol{F}_1\boldsymbol{F}_2^\dagger\boldsymbol{\tau}_r \\
&= -mg\boldsymbol{e}_3 + \boldsymbol{f}_r + \boldsymbol{X} + \boldsymbol{P}_\star^\perp\boldsymbol{R}\boldsymbol{F}_1\boldsymbol{F}_2^\dagger\boldsymbol{\tau}_r,
\end{aligned} \tag{5.19}$$

where

$$\boldsymbol{X} \coloneqq \boldsymbol{P}_\star\boldsymbol{f}_r - \boldsymbol{f}_r = \|\boldsymbol{f}_r\|(\boldsymbol{d}_\star^\top\boldsymbol{R}_d^\top\boldsymbol{R}\boldsymbol{d}_\star\boldsymbol{R}\boldsymbol{d}_\star - \boldsymbol{R}_d\boldsymbol{d}_\star) \tag{5.20}$$

is a term that highlights the misalignment between the preferential direction and the desired thrust directions. In other words, it measures the deviation of the control force from the reference one.

Remark 2 (Spurious Force)**.** *The term*

$$\boldsymbol{P}_\star^\perp\boldsymbol{R}\boldsymbol{F}_1\boldsymbol{F}_2^\dagger\boldsymbol{\tau}_r \tag{5.21}$$

in (5.19) *is referred to as the* spurious force*, i.e., the component of the control force that arises as a consequence of implementing the reference control moment* $\boldsymbol{\tau}_r$*. This force lies in the subspace* $\mathfrak{F}_A \cap \mathfrak{F}_B^{\perp}$*, i.e., in a subspace along which there is no control authority. This subspace is orthogonal to the directions along which the control force can be independently assigned.*

The presence and impact of the spurious force are intrinsically linked to the actuation properties of the platform. In the case of fully decoupled (FD) GTMs, the spurious force can always be compensated, as it resides within $\mathfrak{F}_A$*, which, for FD platforms, is a subspace of* $\mathfrak{F}_B$*—the space where independent force control is available. For partially coupled (PC) GTMs, the spurious force is restricted to the subspace orthogonal to the decoupled directions or planes, i.e., where direct control authority is lacking. In contrast, for fully coupled (FC) GTMs, the control force is entirely dictated by the control moment, resulting in the total control force coinciding with the spurious force. It is important to note, however, that fully coupled platforms (FC) fall outside the scope of this thesis.*

The control law proposed in this thesis is specifically designed to mitigate the effects of the spurious force in partially coupled (PC) platforms, and the analysis of its impact on stability represents a central contribution of this work.

The closed-loop system is thus composed of the attitude and translational closed-loop dynamics given by (5.18) and (5.19), together with the error dynamics for the position and attitude, $\dot{\boldsymbol{e}}_p$ and $\dot{\boldsymbol{e}}_R$, as defined in (C.3). Explicitly, it can be summarized as:

$$\begin{cases} \dot{\boldsymbol{e}}_p = \boldsymbol{v}, \\ \dot{\boldsymbol{v}} = \frac{1}{m}\left(-mg\boldsymbol{e}_3 + \boldsymbol{f}_r + \boldsymbol{X} + \boldsymbol{P}_{\star}^{\perp}\boldsymbol{R}\boldsymbol{F}_1\boldsymbol{F}_2^{\dagger}\boldsymbol{\tau}_r\right), \\ \dot{\boldsymbol{e}}_R = \boldsymbol{C}(\boldsymbol{R}, \boldsymbol{R}_d)\boldsymbol{e}_{\omega}, \\ \dot{\boldsymbol{\omega}} = \boldsymbol{J}^{-1}\left(-\boldsymbol{\omega} \times \boldsymbol{J}\boldsymbol{\omega} + \boldsymbol{\tau}_r\right), \end{cases} \tag{5.22}$$

where the matrix $\boldsymbol{C}(\boldsymbol{R}, \boldsymbol{R}_d)$ is defined in (C.2).

The control law introduced in this chapter is specifically designed to ensure that

$$\lim_{t\to\infty}(\boldsymbol{e}_p(t),\, \boldsymbol{v}(t),\, \boldsymbol{e}_R(t),\, \boldsymbol{\omega}(t)) = (\mathbf{0},\, \mathbf{0},\, \mathbf{0},\, \mathbf{0}), \tag{5.23}$$

which formalizes the objectives stated in (5.3) and (5.7). As shown in the next chapter, the point $(\boldsymbol{e}_p, \boldsymbol{v}, \boldsymbol{e}_R, \boldsymbol{\omega}) = (\mathbf{0}, \mathbf{0}, \mathbf{0}, \mathbf{0})$ constitutes an equilibrium point of the closed-loop system in (5.22). The demonstration of the stability properties of this equilibrium point will be the subject of the next chapter and constitutes the main contribution of this thesis.

5.4 Control Strategy Motivations

This section provides the motivations behind the adopted control strategy. A seemingly natural approach is to design the reference control moment $\boldsymbol{\tau}_r$ so that the attitude tracking errors $\boldsymbol{e}_R$ and $\boldsymbol{e}_{\omega}$ asymptotically vanish, thus ensuring convergence of the platform's attitude to the desired configuration. However, this solution does not guarantee the elimination of the spurious force. We show that the proposed control law not only achieves the attitude objective stated in (5.7), but also enables suppression of the spurious force.

Since $\boldsymbol{R}_d$ is a time-varying rotation matrix, it is associated with a desired angular velocity $\boldsymbol{\omega}_d$ and a desired angular acceleration $\dot{\boldsymbol{\omega}}_d$. One might therefore be inclined to formulate the control law so that $\boldsymbol{e}_R$ and $\boldsymbol{e}_\omega$ are driven to zero, leading to the reference control moment proposed by Lee et al. in [22]:

$$\tilde{\boldsymbol{\tau}}_r = \boldsymbol{\omega} \times \boldsymbol{J}\boldsymbol{\omega} - \boldsymbol{K}_R\boldsymbol{e}_R - \boldsymbol{K}_\omega\boldsymbol{e}_\omega - \boldsymbol{J}\left(\boldsymbol{\omega} \times \boldsymbol{R}^\top \boldsymbol{R}_d\boldsymbol{\omega}_d - \boldsymbol{R}^\top \boldsymbol{R}_d\dot{\boldsymbol{\omega}}_d\right). \tag{5.24}$$

The final term in (5.24) serves as a feedforward component, necessitated by the time-varying nature of $\boldsymbol{R}_d$. This term is essential for accurate tracking of the desired orientation, as it accounts for both $\boldsymbol{\omega}_d$ and $\dot{\boldsymbol{\omega}}_d$. The role of the reference control torque $\tilde{\boldsymbol{\tau}}_r$ is to make the actual attitude dynamics mimic the desired ones. As the attitude tracking errors $\boldsymbol{e}_R$ and $\boldsymbol{e}_\omega$ converge to zero, the current attitude dynamics increasingly resemble the desired dynamics. Nevertheless, this approach fails to ensure the nullification of the spurious force.

From (5.21), it follows that

$$\boldsymbol{P}_\star^\perp \boldsymbol{R}\boldsymbol{F}_1 \boldsymbol{F}_2^\dagger \tilde{\boldsymbol{\tau}}_r = \boldsymbol{0} \quad \Longleftrightarrow \quad \tilde{\boldsymbol{\tau}}_r \to \boldsymbol{0}.$$

However, $\tilde{\boldsymbol{\tau}}_r$ is a function of both $\boldsymbol{\omega}_d$ and $\dot{\boldsymbol{\omega}}_d$. As demonstrated in Appendix D, $\boldsymbol{\omega}_d$ itself depends on the reference control force $\boldsymbol{f}_r$ and its derivative, while $\dot{\boldsymbol{f}}_r$ is influenced by the spurious force, and thus by $\tilde{\boldsymbol{\tau}}_r$.

This interdependence reveals a problematic circularity: attempting to design $\tilde{\boldsymbol{\tau}}_r$ solely to drive the attitude-tracking errors to zero induces a feedback loop between the reference control moment and the spurious force, perpetuating the excitation of the latter.

(a) **(b)**

Figure 5.2. **(a)**: The choice of $\tilde{\boldsymbol{\tau}}_r$ induces a circular dependency between the control moment and the spurious force. **(b)**: The proposed control law breaks this circularity.

The approach proposed by Michieletto et al. [26] departs from the standard objective of driving the tracking error $\boldsymbol{e}_\omega$ to zero. Instead, the control law is designed so that the actual angular velocity $\boldsymbol{\omega}$ converges directly to zero. This ensures that, in steady-state conditions (such as static hovering), the control moment—and consequently any spurious force—naturally vanishes, while still maintaining full attitude control.

Part IV

Stability Analysis

Chapter 6

Stability Analysis

In this chapter, we present a comprehensive stability analysis of the control law developed in Chapter 5, designed for platforms affected by spurious force generation. The analysis methodology is inspired by the framework established by Lee et al. [22], and is adapted to address the specific characteristics of the system under consideration.

The analysis focuses on the closed-loop system dynamics presented in (5.22), within the set $L_1 = \{\boldsymbol{R}, \boldsymbol{R}_d \in \mathbf{SO}(3) : \Psi(\boldsymbol{R}, \boldsymbol{R}_d) < 1\}$, corresponding to attitude errors less than 90°. The stability analysis will be conducted by considering the Lyapunov stability theory. In particular, we will define a Lyapunov candidate function V for the closed-loop system and we will go in search of three class $\mathcal{K}_\infty$ functions α_1, α_2, and α_3 such that

$$\alpha_1(\|\boldsymbol{e}\|) \leq V \leq \alpha_2(\|\boldsymbol{e}\|), \qquad \dot{V} \leq -\alpha_3(\|\boldsymbol{e}\|), \tag{6.1}$$

with

$$\alpha_1(\|\boldsymbol{e}\|) = \lambda_1\|\boldsymbol{e}\|^2, \quad \alpha_3(\|\boldsymbol{e}\|) = \lambda_3\|\boldsymbol{e}\|^2.$$

The relevant definitions of stability—including Lyapunov stability, asymptotic stability, and exponential stability—are provided in Appendix B. Exponential stability is of particular interest in control systems, as it ensures not only convergence of system trajectories to the equilibrium point, but also that this convergence occurs at a rate characterized by an exponential function. This property is highly desirable, as it enables explicit performance guarantees and facilitates robustness analysis with respect to model uncertainties and external disturbances.

The following analysis therefore aims to demonstrate the exponential stability of the closed-loop system, showing that the proposed control law ensures both rapid convergence and strong resilience to perturbations, despite the presence of spurious forces.

Remark 3. *For simplicity, from this point onward, we assume that the gain matrices* $\boldsymbol{K}_p$, $\boldsymbol{K}_v$, $\boldsymbol{K}_R$ *and* $\boldsymbol{K}_\omega$ *presented in* (5.4) *and* (5.10) *are diagonal and isotropic, i.e., they can be written as a positive scalar times the identity matrix,* $\boldsymbol{K}_\Delta = k_\Delta \boldsymbol{I}_3$*, with* $k_\Delta > 0$ *for* $\Delta \in \{p; v; R; \omega\}$*. This assumption does not restrict the generality of the analysis, but allows us to focus on the essential dynamics without unnecessary* *notational complexity. The stability analysis can be extended to more general cases with non-diagonal and/or non-isotropic gain matrices, at the cost of increased notational burden and without providing additional insight into the stability properties of the closed-loop system.*

6.1 Local Exponential Stability

We begin by reformulating the closed-loop system in (5.22), using the definitions of the reference control force $\boldsymbol{f}_r$ and moment $\boldsymbol{\tau}_r$ from (5.4) and (5.10). The resulting closed-loop dynamics are:

$$\begin{cases} \dot{\boldsymbol{e}}_p &= \boldsymbol{v}, \\ m\dot{\boldsymbol{v}} &= -\boldsymbol{K}_p\boldsymbol{e}_p - \boldsymbol{K}_v\boldsymbol{v} + \boldsymbol{X} + \boldsymbol{P}_\star^\perp \boldsymbol{R}\boldsymbol{F}_1\boldsymbol{F}_2^\dagger(\boldsymbol{S}(\boldsymbol{\omega})\boldsymbol{J}\boldsymbol{\omega} - \boldsymbol{K}_R\boldsymbol{e}_R - \boldsymbol{K}_\omega\boldsymbol{\omega}), \\ \dot{\boldsymbol{e}}_R &= \boldsymbol{C}(\boldsymbol{R}_d^\top\boldsymbol{R})(\boldsymbol{\omega} - \boldsymbol{R}^\top\boldsymbol{R}_d\boldsymbol{\omega}_d), \\ \boldsymbol{J}\dot{\boldsymbol{\omega}} &= -\boldsymbol{K}_R\boldsymbol{e}_R - \boldsymbol{K}_\omega\boldsymbol{\omega}, \end{cases} \tag{6.2}$$

where the angular velocity tracking error $\boldsymbol{e}_\omega$ from (C.7) has been incorporated into the third equation.

Appendix D details how the desired angular velocity $\boldsymbol{\omega}_d$ can be expressed as a function of the tracking errors $\boldsymbol{e}_R$, $\boldsymbol{\omega}$, $\boldsymbol{e}_p$, and $\boldsymbol{v}$, with the final result summarized in (D.6). Specifically, using $\boldsymbol{w}_3 = \hat{\boldsymbol{f}}_r$ and $\dot{\boldsymbol{w}}_3 = \dot{\hat{\boldsymbol{f}}}_r$ as defined in (D.10), the desired angular velocity is given by:

$$\boldsymbol{\omega}_d = \boldsymbol{R}_d^\top[\boldsymbol{I}_3 + \frac{\hat{\boldsymbol{r}}_1^\top\hat{\boldsymbol{f}}_r}{\|\hat{\boldsymbol{f}}_r \times \hat{\boldsymbol{r}}_1\|^2}\hat{\boldsymbol{f}}_r\hat{\boldsymbol{r}}_1^\top](\hat{\boldsymbol{f}}_r \times \frac{1}{\|\boldsymbol{f}_r\|}(\boldsymbol{I}_3 - \hat{\boldsymbol{f}}_r\hat{\boldsymbol{f}}_r^\top)\dot{\boldsymbol{f}}_r). \tag{6.3}$$

The time derivative of the reference control force $\boldsymbol{f}_r$ is

$$\dot{\boldsymbol{f}}_r = -\boldsymbol{K}_p\dot{\boldsymbol{e}}_p - \boldsymbol{K}_v\dot{\boldsymbol{v}}, \tag{6.4}$$

where $\dot{\boldsymbol{e}}_p = \boldsymbol{v}$ and $\dot{\boldsymbol{v}}$ is given by the second equation of (6.2). Substituting these, we obtain

$$\begin{aligned} \dot{\boldsymbol{f}}_r =& \frac{1}{m}\boldsymbol{K}_v\boldsymbol{K}_p\boldsymbol{e}_p + \left(\frac{1}{m}\boldsymbol{K}_v^2 - \boldsymbol{K}_p\right)\boldsymbol{v} - \frac{1}{m}\boldsymbol{K}_v\boldsymbol{X} \\ &- \frac{1}{m}\boldsymbol{K}_v\boldsymbol{P}_\star^\perp\boldsymbol{R}\boldsymbol{F}_1\boldsymbol{F}_2^\dagger(\boldsymbol{S}(\boldsymbol{\omega})\boldsymbol{J}\boldsymbol{\omega} - \boldsymbol{K}_R\boldsymbol{e}_R - \boldsymbol{K}_\omega\boldsymbol{\omega}). \end{aligned} \tag{6.5}$$

This explicit expression for $\dot{\boldsymbol{f}}_r$ can be substituted into (6.3), yielding a complete characterization of $\boldsymbol{\omega}_d$ in terms of the tracking errors and control gains. The resulting closed-loop system can be written as:

$$\begin{cases} \dot{\boldsymbol{e}}_p &= \boldsymbol{v}, \\ m\dot{\boldsymbol{v}} &= -\boldsymbol{K}_p\boldsymbol{e}_p - \boldsymbol{K}_v\boldsymbol{v} + \boldsymbol{X} + \boldsymbol{P}_\star^\perp \boldsymbol{R}\boldsymbol{F}_1\boldsymbol{F}_2^\dagger(\boldsymbol{S}(\boldsymbol{\omega})\boldsymbol{J}\boldsymbol{\omega} - \boldsymbol{K}_R\boldsymbol{e}_R - \boldsymbol{K}_\omega\boldsymbol{\omega}), \\ \dot{\boldsymbol{e}}_R &= \boldsymbol{C}(\boldsymbol{R}_d^\top\boldsymbol{R})\Big\{\boldsymbol{\omega} - \boldsymbol{R}^\top[\boldsymbol{I}_3 + \frac{\hat{\boldsymbol{r}}_1^\top\hat{\boldsymbol{f}}_r}{\|\hat{\boldsymbol{f}}_r \times \hat{\boldsymbol{r}}_1\|^2}\hat{\boldsymbol{f}}_r\hat{\boldsymbol{r}}_1^\top]\Big[\hat{\boldsymbol{f}}_r \times \tfrac{1}{\|\boldsymbol{f}_r\|}(\boldsymbol{I}_3 - \hat{\boldsymbol{f}}_r\hat{\boldsymbol{f}}_r^\top) \\ &\qquad \Big(\tfrac{1}{m}\boldsymbol{K}_v\boldsymbol{K}_p\boldsymbol{e}_p + (\tfrac{1}{m}\boldsymbol{K}_v^2 - \boldsymbol{K}_p)\boldsymbol{v} - \tfrac{1}{m}\boldsymbol{K}_v\boldsymbol{X} \\ &\qquad -\tfrac{1}{m}\boldsymbol{K}_v\boldsymbol{P}_\star^\perp\boldsymbol{R}\boldsymbol{F}_1\boldsymbol{F}_2^\dagger(\boldsymbol{S}(\boldsymbol{\omega})\boldsymbol{J}\boldsymbol{\omega} - \boldsymbol{K}_R\boldsymbol{e}_R - \boldsymbol{K}_\omega\boldsymbol{\omega})\Big)\Big]\Big\}, \\ \boldsymbol{J}\dot{\boldsymbol{\omega}} &= -\boldsymbol{K}_R\boldsymbol{e}_R - \boldsymbol{K}_\omega\boldsymbol{\omega}. \end{cases} \tag{6.6}$$

It is straightforward to verify that the origin $(\boldsymbol{e}_p, \boldsymbol{v}, \boldsymbol{e}_R, \boldsymbol{\omega}) = (\mathbf{0}, \mathbf{0}, \mathbf{0}, \mathbf{0})$ is an equilibrium point[1] for the closed-loop system (6.6).

Proposition 6.1 (Local Exponential Stability)**.** *Let us consider the closed-loop tracking errors system* (6.6)*, derived by closing the loop with the reference control force* $\boldsymbol{f}_r$*, reference control moment* $\boldsymbol{\tau}_r$*, and reference control input* $\boldsymbol{u}_r$ *as defined in* (5.4)*,* (5.10)*, and* (5.12)*, respectively.*

Assume that

$$\Psi(\boldsymbol{R}(t), \boldsymbol{R}_d(t)) < 1, \quad \forall t \geq 0, \tag{6.7}$$

Define the matrices $\boldsymbol{W}_1$*,* $\boldsymbol{W}_2$ *and* $\tilde{\boldsymbol{W}} \in \mathbb{R}^{3\times 3}$ *as follows:*

$$\begin{aligned}
\boldsymbol{W}_1 &= \begin{bmatrix} c_1 \frac{k_p}{m}(1 - e_R^{\max}) & -c_1 \frac{k_v}{2m}(1 + e_R^{\max}) \\ -c_1 \frac{k_v}{2m}(1 + e_R^{\max}) & k_v(1 - e_R^{\max}) - c_1 \end{bmatrix}, \\
\boldsymbol{W}_2 &= \begin{bmatrix} c_2 \frac{k_R}{\lambda_{\max}(\boldsymbol{J})} - k_R k_v \alpha\,(mg + k_R\gamma) & -\frac{\sigma_{R,\omega}}{2} \\ -\frac{\sigma_{R,\omega}}{2} & k_\omega - c_2\big(1 + k_v\gamma\alpha(\beta + k_\omega)\big) \end{bmatrix}, \\
\tilde{\boldsymbol{W}} &= \boldsymbol{W}_{12} + \boldsymbol{W}_{21},
\end{aligned}$$

where

$$\begin{aligned}
\sigma_{R,\omega} &:= c_2 \left(\frac{k_\omega}{\lambda_{\min}(\boldsymbol{J})} + k_v \gamma \alpha\,(mg + k_R\gamma) \right) + k_R k_v \gamma \alpha (\beta + k_\omega), \\
\boldsymbol{W}_{12} &= \begin{bmatrix} c_1(g + k_R \frac{\gamma}{m}) & c_1 \frac{\gamma}{m}(\beta + k_\omega) \\ k_p e_p^{\max} + mg + \gamma k_R & \gamma(\beta + k_\omega) \end{bmatrix}, \\
\boldsymbol{W}_{21} &= \begin{bmatrix} k_R k_p k_v \alpha (1 + e_R^{\max}) & c_2 k_p k_v \alpha (1 + e_R^{\max}) \\ k_R \alpha m \left(\left| \frac{k_v^2}{m} - k_p \right| + \frac{k_v^2}{m} e_R^{\max} \right) & c_2 \alpha m \left(\left| \frac{k_v^2}{m} - k_p \right| + \frac{k_v^2}{m} e_R^{\max} \right) \end{bmatrix}.
\end{aligned}$$

Let $c_1, c_2, k_p, k_v, k_R, k_\omega$ *be positive constants such that the following conditions hold:*

$$c_1 < \min\left\{ \sqrt{m\,k_p},\ k_v\,(1 - e_R^{\max}),\ \frac{4\,k_p\,k_v\,m\,(e_R^{\max} - 1)^2}{k_v^2\,(e_R^{\max} + 1)^2 + 4\,k_p\,m\,(1 - e_R^{\max})} \right\}, \tag{6.8}$$

$$c_2 < \min\left\{ \sqrt{\lambda_{\min}(\boldsymbol{J}) k_R},\ \frac{k_\omega}{1 + k_v\gamma\alpha(\beta + k_\omega)},\ c_{2,+} \right\}, \tag{6.9}$$

$$c_2 > \max\left\{ k_v \lambda_{\max}(\boldsymbol{J}) \alpha (mg + k_R\gamma),\ c_{2,-} \right\}, \tag{6.10}$$

$$\|\tilde{\boldsymbol{W}}\|^2 < 4\lambda_{\min}(\boldsymbol{W}_1)\lambda_{\min}(\boldsymbol{W}_2). \tag{6.11}$$

Then, the equilibrium point $(\boldsymbol{e}_p, \boldsymbol{v}, \boldsymbol{e}_R, \boldsymbol{\omega}) = (\mathbf{0}, \mathbf{0}, \mathbf{0}, \mathbf{0})$ *is locally exponentially stable. A region inside which the system is guaranteed to be stable is defined as:*

$$\mathcal{D} := \{ (\boldsymbol{e}_p, \boldsymbol{v}, \boldsymbol{R}, \boldsymbol{\omega}) \in \mathbb{R}^3 \times \mathbb{R}^3 \times \mathbf{SO}(3) \times \mathbb{R}^3 \mid \|\boldsymbol{e}_p\| < e_p^{\max},\ \boldsymbol{R} \in L_1,\ \|\boldsymbol{\omega}\| < \omega^{\max} \} \tag{6.12}$$

where $L_1 = \{\boldsymbol{R}, \boldsymbol{R}_d \in \mathbf{SO}(3) : \Psi(\boldsymbol{R}, \boldsymbol{R}_d) < 1\}$ *corresponds to attitude errors less than* 90°*, and* $e_p^{\max}$ *and* $\omega^{\max}$ *are bounds on the position and angular velocity errors, respectively. In particular,* $e_p^{\max}$ *can be chosen as*

$$\lambda_{\max}(\boldsymbol{M}_{12})\|\boldsymbol{z}_1(0)\| + \lambda_{\max}(\boldsymbol{M}_{22})\|\boldsymbol{z}_2(0)\| < \frac{1}{2} k_p e_p^{\max}, \tag{6.13}$$

---

[1] Indeed, when $\boldsymbol{e}_R = \mathbf{0}$, also $\boldsymbol{X}$ vanishes, as can be seen from its definition in (5.20)

where $\boldsymbol{z}_1 = \begin{bmatrix} \|\boldsymbol{e}_p\| & \|\boldsymbol{v}\| \end{bmatrix}^\top$ *and* $\boldsymbol{z}_2 = \begin{bmatrix} \|\boldsymbol{e}_R\| & \|\boldsymbol{\omega}\| \end{bmatrix}^\top$ *and the matrices* $\boldsymbol{M}_{12}$ *and* $\boldsymbol{M}_{21}$ *are defined as*

$$\boldsymbol{M}_{12} = \begin{bmatrix} k_p & c_1 \\ c_1 & m \end{bmatrix}, \qquad \boldsymbol{M}_{22} = \begin{bmatrix} \frac{2k_R}{2-\psi} & c_2 \\ c_2 & \lambda_{\max}(\boldsymbol{J}) \end{bmatrix}.$$

In the subsequent sections, we rigorously establish the proof of Proposition 6.1, confining our analysis to the domain $\mathcal{D}$ as delineated in (6.12). This domain characterizes the set of admissible states for which the local exponential stability of the closed-loop tracking error system can be guaranteed.

It is important to note that the actual region of attraction—namely, the set of initial conditions from which the system trajectories remain within $\mathcal{D}$ for all future times and asymptotically converge to the equilibrium—constitutes a subset of $\mathcal{D}$. Specifically, we define the region of attraction as

$$\mathcal{D}_a = \{(\boldsymbol{e}_p, \boldsymbol{v}, \boldsymbol{R}, \boldsymbol{\omega}) \in \mathcal{D} : \|\boldsymbol{e}_p(0)\| < e_p^{\max},\ \|\boldsymbol{e}_R(0)\| < e_R^{\max},\ \|\boldsymbol{\omega}(0)\| < \omega^{\max}\}. \tag{6.14}$$

Within this set, the closed-loop system is guaranteed to exhibit the desired local exponential convergence properties.

6.2 Lyapunov Candidate Function

To analyze the stability properties of the equilibrium point $(\boldsymbol{e}_p, \boldsymbol{v}, \boldsymbol{e}_R, \boldsymbol{\omega}) = (\boldsymbol{0}, \boldsymbol{0}, \boldsymbol{0}, \boldsymbol{0})$, we construct a Lyapunov candidate function for the closed-loop system. Consider the following composite function:

$$V(\boldsymbol{e}_p, \boldsymbol{v}, \boldsymbol{e}_R, \boldsymbol{\omega}) = V_1(\boldsymbol{e}_p, \boldsymbol{v}) + V_2(\boldsymbol{e}_R, \boldsymbol{\omega}), \tag{6.15}$$

where

$$V_1(\boldsymbol{e}_p, \boldsymbol{v}) = \frac{1}{2} m\|\boldsymbol{v}\|^2 + \frac{1}{2} k_p \|\boldsymbol{e}_p\|^2 + c_1 \boldsymbol{e}_p^\top \boldsymbol{v}, \tag{6.16}$$

$$V_2(\boldsymbol{e}_R, \boldsymbol{\omega}) = \frac{1}{2} \boldsymbol{\omega}^\top \boldsymbol{J} \boldsymbol{\omega} + k_R \Psi(\boldsymbol{R}, \boldsymbol{R}_d) + c_2 \boldsymbol{e}_R^\top \boldsymbol{\omega}. \tag{6.17}$$

Here, c_1 and c_2 are non-negative scalar parameters which are introduced to facilitate the Lyapunov analysis and can be appropriately selected to guarantee exponential stability.

The time derivative of V along the trajectories of the closed-loop system (6.2) is given by

$$\dot{V}(\boldsymbol{e}_p, \boldsymbol{v}, \boldsymbol{e}_R, \boldsymbol{\omega}) = \dot{V}_1(\boldsymbol{e}_p, \boldsymbol{v}, \boldsymbol{e}_R, \boldsymbol{\omega}) + \dot{V}_2(\boldsymbol{e}_p, \boldsymbol{v}, \boldsymbol{e}_R, \boldsymbol{\omega}), \tag{6.18}$$

where

$$\dot{V}_1(\boldsymbol{e}_p, \boldsymbol{v}, \boldsymbol{e}_R, \boldsymbol{\omega}) = m\boldsymbol{v}^\top \dot{\boldsymbol{v}} + k_p \boldsymbol{e}_p^\top \boldsymbol{v} + c_1 \boldsymbol{e}_p^\top \dot{\boldsymbol{v}} + c_1 \|\boldsymbol{v}\|^2, \tag{6.19}$$

$$\dot{V}_2(\boldsymbol{e}_R, \boldsymbol{\omega}, \boldsymbol{e}_p, \boldsymbol{v}) = \boldsymbol{\omega}^\top \boldsymbol{J} \dot{\boldsymbol{\omega}} + k_R \dot{\Psi}(\boldsymbol{R}, \boldsymbol{R}_d) + c_2 \left(\dot{\boldsymbol{e}}_R^\top \boldsymbol{\omega} + \boldsymbol{e}_R^\top \dot{\boldsymbol{\omega}} \right). \tag{6.20}$$

Substituting the closed-loop dynamics for $\dot{\boldsymbol{v}}$ from (6.2) into (6.19), we obtain

$$\begin{aligned}\dot{V}_1 &= \boldsymbol{v}^\top \left(-\boldsymbol{K}_p\boldsymbol{e}_p - \boldsymbol{K}_v\boldsymbol{v} + \boldsymbol{X} + \boldsymbol{P}_\star^\perp\boldsymbol{R}\boldsymbol{F}_1\boldsymbol{F}_2^\dagger\left(\boldsymbol{S}(\boldsymbol{\omega})\boldsymbol{J}\boldsymbol{\omega} - \boldsymbol{K}_R\boldsymbol{e}_R - \boldsymbol{K}_\omega\boldsymbol{\omega}\right)\right)\\ &\quad + \frac{c_1}{m}\boldsymbol{e}_p^\top \left(-\boldsymbol{K}_p\boldsymbol{e}_p - \boldsymbol{K}_v\boldsymbol{v} + \boldsymbol{X} + \boldsymbol{P}_\star^\perp\boldsymbol{R}\boldsymbol{F}_1\boldsymbol{F}_2^\dagger\left(\boldsymbol{S}(\boldsymbol{\omega})\boldsymbol{J}\boldsymbol{\omega} - \boldsymbol{K}_R\boldsymbol{e}_R - \boldsymbol{K}_\omega\boldsymbol{\omega}\right)\right)\\ &\quad + k_p\boldsymbol{e}_p^\top\boldsymbol{v} + c_1\|\boldsymbol{v}\|^2.\end{aligned}$$

By collecting like terms, the above expression can be rewritten as

$$\begin{aligned}\dot{V}_1 &= -(k_v - c_1)\|\boldsymbol{v}\|^2 - c_1\frac{k_p}{m}\|\boldsymbol{e}_p\|^2 - c_1\frac{k_v}{m}\boldsymbol{e}_p^\top\boldsymbol{v}\\ &\quad + \left(\frac{c_1}{m}\boldsymbol{e}_p^\top + \boldsymbol{v}^\top\right)\boldsymbol{P}_\star^\perp\boldsymbol{R}\boldsymbol{F}_1\boldsymbol{F}_2^\dagger\left(\boldsymbol{S}(\boldsymbol{\omega})\boldsymbol{J} - k_\omega\boldsymbol{I}_3\right)\boldsymbol{\omega}\\ &\quad - k_R\left(\frac{c_1}{m}\boldsymbol{e}_p^\top + \boldsymbol{v}^\top\right)\boldsymbol{P}_\star^\perp\boldsymbol{R}\boldsymbol{F}_1\boldsymbol{F}_2^\dagger\boldsymbol{e}_R + \left(\frac{c_1}{m}\boldsymbol{e}_p^\top + \boldsymbol{v}^\top\right)\boldsymbol{X}.\end{aligned} \tag{6.21}$$

Similarly, the time derivative of V_2 can be expanded by substituting the expressions for $\dot{\boldsymbol{e}}_R$ and $\dot{\boldsymbol{\omega}}$ from the last two equations in (6.2), as well as $\dot{\Psi}(\boldsymbol{R}, \boldsymbol{R}_d)$ from (C.1), into (6.20), yielding

$$\begin{aligned}\dot{V}_2 = &- k_\omega\|\boldsymbol{\omega}\|^2 + c_2\boldsymbol{\omega}^\top\boldsymbol{C}(\boldsymbol{R}_d^\top\boldsymbol{R})\boldsymbol{\omega} - c_2k_R\boldsymbol{e}_R^\top\boldsymbol{J}^{-1}\boldsymbol{e}_R - c_2k_\omega\boldsymbol{e}_R^\top\boldsymbol{J}^{-1}\boldsymbol{\omega}\\ &- c_2\boldsymbol{\omega}^\top\boldsymbol{C}(\boldsymbol{R}_d^\top\boldsymbol{R})\boldsymbol{R}^\top\boldsymbol{R}_d\boldsymbol{\omega}_d - k_R\boldsymbol{e}_R^\top\boldsymbol{R}^\top\boldsymbol{R}_d\boldsymbol{\omega}_d,\end{aligned} \tag{6.22}$$

in which we have used the expression of the angular velocity tracking error $\boldsymbol{e}_\omega$ from (C.7).

6.3 Bounding the Lyapunov Candidate Derivative

In this section, we establish an upper bound for the time derivative of the Lyapunov candidate function V as defined in (6.15).

To facilitate the analysis, we decompose the derivative $\dot{V}$ into two components, $\dot{V}_1$ and $\dot{V}_2$, and derive separate bounds for each. We then combine these results to obtain an overall bound for $\dot{V}$.

6.3.1 Bounding the First Lyapunov Derivative

To derivative an upper bound for the Lyapunov candidate $\dot{V}_1$, we can exploit the following inequalities:

$$-c_1\frac{k_v}{m}\boldsymbol{e}_p^\top\boldsymbol{e}_v \le c_1\frac{k_v}{m}\|\boldsymbol{e}_p\|\|\boldsymbol{e}_v\|, \tag{6.23}$$

$$\|\frac{c_1}{m}\boldsymbol{e}_p^\top + \boldsymbol{e}_v^\top\| \le \frac{c_1}{m}\|\boldsymbol{e}_p\| + \|\boldsymbol{e}_v\|, \tag{6.24}$$

$$\|\boldsymbol{S}(\boldsymbol{\omega})\boldsymbol{J} - k_\omega\boldsymbol{I}_3\| \le \lambda_{\max}(\boldsymbol{J})\omega^{\max} + k_\omega, \tag{6.25}$$

where we are assuming that the system dynamics are uniformly globally bounded. Thereby, we can say that the angular velocity magnitude is bounded by $\omega^{\max}$, which denote this upper bound.

Additionally, we need to bound the terms $\boldsymbol{P}_\star^\perp \boldsymbol{R} \boldsymbol{F}_1 \boldsymbol{F}_2^\dagger$ and $\boldsymbol{X}$. For the term $\|\boldsymbol{P}_\star^\perp \boldsymbol{R} \boldsymbol{F}_1 \boldsymbol{F}_2^\dagger\|$, we can write:

$$\|\boldsymbol{P}_\star^\perp \boldsymbol{R} \boldsymbol{F}_1 \boldsymbol{F}_2^\dagger\| \leq \|\boldsymbol{P}_\star^\perp\| \, \|\boldsymbol{R}\| \, \|\boldsymbol{F}_1\| \, \|\boldsymbol{F}_2^\dagger\| = \frac{\sigma_{\max}(\boldsymbol{F}_1)}{\sigma_{\min}(\boldsymbol{F}_2)} =: \gamma, \tag{6.26}$$

where:

- $\sigma_{\max}(\boldsymbol{F}_1)$ and $\sigma_{\min}(\boldsymbol{F}_2)$ denote the maximum singular value of $\boldsymbol{F}_1$ and the minimum singular value of $\boldsymbol{F}_2$, respectively;
- $\|\boldsymbol{P}_\star^\perp\| = 1^2$;
- $\|\boldsymbol{R}\| = 1$.

The ratio $\frac{\sigma_{\max}(\boldsymbol{F}_1)}{\sigma_{\min}(\boldsymbol{F}_2)}$ depends on the configuration of the GTM and quantifies the relative scaling between the maximum amplification induced by $\boldsymbol{F}_1$ and the minimum amplification maintained by $\boldsymbol{F}_2$. A large value indicates that $\boldsymbol{F}_1$ can strongly amplify certain directions, while $\boldsymbol{F}_2$ may significantly attenuate in at least one direction, potentially leading to instability. Conversely, a smaller ratio suggests that both $\boldsymbol{F}_1$ and $\boldsymbol{F}_2$ exhibit similar amplification properties across all directions, indicating more uniform and stable system behavior.

To bound the term $\boldsymbol{X}$, recall its definition in (5.20). By the sub-multiplicative property of norms,

$$\|\boldsymbol{X}\| \leq \|\boldsymbol{f}_r\| \left\| \left(\boldsymbol{d}_\star^\top \boldsymbol{R}_d^\top \boldsymbol{R} \boldsymbol{d}_\star \right) \boldsymbol{R} \boldsymbol{d}_\star - \boldsymbol{R}_d \boldsymbol{d}_\star \right\|.$$

We analyze each factor:

- The force term is bounded as $\|\boldsymbol{f}_r\| \leq k_p \|\boldsymbol{e}_p\| + k_v \|\boldsymbol{e}_v\| + mg$.
- The second term can be rewritten using the vector triple product:

  $$\left(\boldsymbol{d}_\star^\top \boldsymbol{R}_d^\top \boldsymbol{R} \boldsymbol{d}_\star \right) \boldsymbol{R} \boldsymbol{d}_\star - \boldsymbol{R}_d \boldsymbol{d}_\star = \hat{\boldsymbol{f}}_c \times (\hat{\boldsymbol{f}}_c \times \hat{\boldsymbol{f}}_r),$$

  where $\hat{\boldsymbol{f}}_c = \boldsymbol{R} \boldsymbol{d}_\star$ and $\hat{\boldsymbol{f}}_r = \boldsymbol{R}_d \boldsymbol{d}_\star$ are unit vectors. The norm of this expression is $\sin(\beta)$, where β is the angle between $\hat{\boldsymbol{f}}_c$ and $\hat{\boldsymbol{f}}_r$.

Therefore,

$$\left\| \left(\boldsymbol{d}_\star^\top \boldsymbol{R}_d^\top \boldsymbol{R} \boldsymbol{d}_\star \right) \boldsymbol{R} \boldsymbol{d}_\star - \boldsymbol{R}_d \boldsymbol{d}_\star \right\| = \sin(\beta) = \|\boldsymbol{e}_R\| = \sqrt{\Psi(2 - \Psi)},$$

where Ψ is the attitude error function, bounded above by 2. This equality has already been proven in Appendix C, specifically in (C.6). Thus,

$$\|\boldsymbol{X}\| \leq (k_p \|\boldsymbol{e}_p\| + k_v \|\boldsymbol{e}_v\| + mg) \|\boldsymbol{e}_R\| \leq (k_p \|\boldsymbol{e}_p\| + k_v \|\boldsymbol{e}_v\| + mg) e_R^{\max}. \tag{6.27}$$

---

[2] To show that $\|\boldsymbol{P}_\star^\perp\|_2 = 1$, consider a vector $\boldsymbol{v} = \alpha \boldsymbol{R} \boldsymbol{d}_\star + \boldsymbol{z}$. This vector is an eigenvector of $\boldsymbol{P}_\star^\perp$ if and only if there exists $\lambda \in \mathbb{R}$ such that $\boldsymbol{P}_\star^\perp \boldsymbol{v} = \lambda \boldsymbol{v}$. In particular:

– If $\boldsymbol{z} = \boldsymbol{0}$, then $\boldsymbol{P}_\star^\perp \boldsymbol{v} = \alpha \, \boldsymbol{P}_\star^\perp \boldsymbol{R} \boldsymbol{d}_\star = \boldsymbol{0}$, which implies $\lambda = 0$.

– If $\alpha = 0$, then $\boldsymbol{P}_\star^\perp \boldsymbol{v} = \boldsymbol{z}$, and hence $\lambda = 1$.

Thus, the eigenvalues are $\lambda = 0$ (multiplicity 1) and $\lambda = 1$ (multiplicity 2).

Finally, we can combine all these bounds to obtain an upper bound for the Lyapunov candidate derivative $\dot{V}_1$:

$$\begin{aligned}\dot{V}_1 \leq& -(k_v - c_1)\|\boldsymbol{v}\|^2 - c_1\frac{k_p}{m}\|\boldsymbol{e}_p\|^2 + c_1\frac{k_v}{m}\|\boldsymbol{e}_p\|\|\boldsymbol{v}\| \\ &+ (\frac{c_1}{m}\|\boldsymbol{e}_p\| + \|\boldsymbol{v}\|)\gamma\Big((\lambda_{\max}(\boldsymbol{J})\omega^{\max} + k_\omega)\|\boldsymbol{\omega}\| + k_R\|\boldsymbol{e}_R\|\Big) \\ &+ (\frac{c_1}{m}\|\boldsymbol{e}_p\| + \|\boldsymbol{v}\|)(k_p\|\boldsymbol{e}_p\| + k_v\|\boldsymbol{v}\| + mg)\|\boldsymbol{e}_R\|.\end{aligned}$$

Note that the above expression contains a third-order error term, specifically $k_p\|\boldsymbol{e}_R\|\|\boldsymbol{e}_p\|\|\boldsymbol{e}_v\|$. While this term can be bounded using $\|\boldsymbol{e}_R\| \leq e_R^{\max}$, doing so complicates the stability analysis and may require a tighter bound on the initial attitude error. To simplify the analysis, we instead impose an upper bound $e_p^{\max}$ on the position tracking error $\|\boldsymbol{e}_p\|$, treating it as a design parameter. With this restriction and rearranging the terms, the bound becomes

$$\begin{aligned}\dot{V}_1 \leq& -\big(k_v(1 - e_R^{\max}) - c_1\big)\|\boldsymbol{v}\|^2 + c_1\frac{k_v}{m}(1 + e_R^{\max})\|\boldsymbol{e}_p\|\|\boldsymbol{v}\| \\ &- c_1\frac{k_p}{m}(1 - e_R^{\max})\|\boldsymbol{e}_p\|^2 + c_1\Big(g + \gamma\frac{k_R}{m}\Big)\|\boldsymbol{e}_p\|\|\boldsymbol{e}_R\| + k_p e_p^{\max}\|\boldsymbol{v}\|\|\boldsymbol{e}_R\| \\ &+ (mg + \gamma k_R)\|\boldsymbol{v}\|\|\boldsymbol{e}_R\| + c_1\frac{\gamma}{m}(\lambda_{\max}(\boldsymbol{J})\omega^{\max} + k_\omega)\|\boldsymbol{e}_p\|\|\boldsymbol{\omega}\| \\ &+ \gamma(\lambda_{\max}(\boldsymbol{J})\omega^{\max} + k_\omega)\|\boldsymbol{v}\|\|\boldsymbol{\omega}\|.\end{aligned}$$

By rearranging the terms, we can write the Lyapunov derivative as

$$\dot{V}_1 \leq -\boldsymbol{z}_1^\top \boldsymbol{W}_1 \boldsymbol{z}_1 + \boldsymbol{z}_1^\top \boldsymbol{W}_{12}\boldsymbol{z}_2, \tag{6.28}$$

where $\boldsymbol{z}_1 = \begin{bmatrix}\|\boldsymbol{e}_p\| & \|\boldsymbol{v}\|\end{bmatrix}^\top$ and $\boldsymbol{z}_2 = \begin{bmatrix}\|\boldsymbol{e}_R\| & \|\boldsymbol{\omega}\|\end{bmatrix}^\top$. The matrices $\boldsymbol{W}_1$ and $\boldsymbol{W}_{12}$ are defined as

$$\boldsymbol{W}_1 = \begin{bmatrix} c_1\frac{k_p}{m}(1 - e_R^{\max}) & -c_1\frac{k_v}{2m}(1 + e_R^{\max}) \\ -c_1\frac{k_v}{2m}(1 + e_R^{\max}) & k_v(1 - e_R^{\max}) - c_1 \end{bmatrix}, \tag{6.29}$$

$$\boldsymbol{W}_{12} = \begin{bmatrix} c_1(g + k_R\frac{\gamma}{m}) & c_1\frac{\gamma}{m}(\lambda_{\max}(\boldsymbol{J})\omega^{\max} + k_\omega) \\ k_p e_p^{\max} + mg + \gamma k_R & \gamma(\lambda_{\max}(\boldsymbol{J})\omega^{\max} + k_\omega) \end{bmatrix}. \tag{6.30}$$

6.3.2 Bounding the Second Lyapunov Derivative

Let us analyze the structure of the Lyapunov candidate derivative $\dot{V}_2$ defined in (6.22) in order to derive bounds. To this end, we are going to analyze each term separately.

- **First term:** $c_2\boldsymbol{\omega}^\top\boldsymbol{C}^\top(\boldsymbol{R}_d^\top\boldsymbol{R})\boldsymbol{\omega}$. By applying the bound from (C.4), we have

$$c_2\boldsymbol{\omega}^\top\boldsymbol{C}^\top(\boldsymbol{R}_d^\top\boldsymbol{R})\boldsymbol{\omega} \leq c_2\|\boldsymbol{\omega}\|^2. \tag{6.31}$$

- **Second term:** $-c_2k_R\boldsymbol{e}_R^\top\boldsymbol{J}^{-1}\boldsymbol{e}_R$. Since $\boldsymbol{J}$ is positive definite, its inverse is also positive definite. Thus,

$$\lambda_{\min}(\boldsymbol{J}^{-1})\|\boldsymbol{e}_R\|^2 \leq \boldsymbol{e}_R^\top\boldsymbol{J}^{-1}\boldsymbol{e}_R \leq \lambda_{\max}(\boldsymbol{J}^{-1})\|\boldsymbol{e}_R\|^2,$$

where $\lambda_{\min}(\boldsymbol{J}^{-1}) = 1/\lambda_{\max}(\boldsymbol{J})$. Therefore,

$$-c_2 k_R \boldsymbol{e}_R^\top \boldsymbol{J}^{-1} \boldsymbol{e}_R \leq -\frac{c_2 k_R}{\lambda_{\max}(\boldsymbol{J})} \|\boldsymbol{e}_R\|^2. \tag{6.32}$$

- **Third term:** $-c_2 k_\omega \boldsymbol{e}_R^\top \boldsymbol{J}^{-1} \boldsymbol{\omega}$. Using the Cauchy-Schwarz inequality and $\lambda_{\max}(\boldsymbol{J}^{-1}) = 1/\lambda_{\min}(\boldsymbol{J})$, we obtain

$$-c_2 k_\omega \boldsymbol{e}_R^\top \boldsymbol{J}^{-1} \boldsymbol{\omega} \leq \frac{c_2 k_\omega}{\lambda_{\min}(\boldsymbol{J})} \|\boldsymbol{e}_R\| \|\boldsymbol{\omega}\|. \tag{6.33}$$

- **Fourth term:** $-c_2 \boldsymbol{\omega}^\top \boldsymbol{C}(\boldsymbol{R}_d^\top \boldsymbol{R}) \boldsymbol{R}^\top \boldsymbol{R}_d \boldsymbol{\omega}_d$. Using the bound from (C.4) and the fact that rotation matrices are orthogonal (i.e., $\|\boldsymbol{R}\| = 1$ for all $\boldsymbol{R} \in \mathbf{SO}(3)$), we obtain

$$-c_2 \boldsymbol{\omega}^\top \boldsymbol{C}(\boldsymbol{R}_d^\top \boldsymbol{R}) \boldsymbol{R}^\top \boldsymbol{R}_d \boldsymbol{\omega}_d \leq c_2 \|\boldsymbol{\omega}\| \|\boldsymbol{\omega}_d\|. \tag{6.34}$$

- **Fifth term:** $-k_R \boldsymbol{e}_R^\top \boldsymbol{R}^\top \boldsymbol{R}_d \boldsymbol{\omega}_d$. Applying the Cauchy-Schwarz inequality and the orthogonality of rotation matrices, we have

$$-k_R \boldsymbol{e}_R^\top \boldsymbol{R}^\top \boldsymbol{R}_d \boldsymbol{\omega}_d \leq k_R \|\boldsymbol{e}_R\| \|\boldsymbol{\omega}_d\|. \tag{6.35}$$

In conclusion, by combining (6.31), (6.32), (6.33), (6.34) and (6.35) we can write

$$\begin{aligned} \dot{V}_2 \leq & -(k_\omega - c_2)\|\boldsymbol{\omega}\|^2 - c_2 \frac{k_R}{\lambda_{\max}(\boldsymbol{J})} \|\boldsymbol{e}_R\|^2 + c_2 \frac{k_\omega}{\lambda_{\min}(\boldsymbol{J})} \|\boldsymbol{e}_R\| \|\boldsymbol{\omega}\| \\ & + c_2 \|\boldsymbol{\omega}\| \|\boldsymbol{\omega}_d\| + k_R \|\boldsymbol{e}_R\| \|\boldsymbol{\omega}_d\|. \end{aligned}$$

Finally, by combining the bound for the desired angular velocity in (D.11) and the boundedness of the terms $\boldsymbol{X}$ and $\boldsymbol{\tau}_r$ in (6.27) and (6.25), respectively, we get a final bound for the desired angular velocity:

$$\begin{aligned} \|\boldsymbol{\omega}_d\| \leq \left(1 + \frac{\delta}{1-\delta^2}\right) \Bigg[& \frac{k_p k_v}{m^2 g}(1 + e_R^{\max})\|\boldsymbol{e}_p\| + \frac{1}{mg}\left(|\frac{k_v^2}{m} - k_p| + \frac{k_v^2}{m} e_R^{\max}\right) \|\boldsymbol{v}\| \\ & + \frac{k_v}{mg}\left(g + \frac{\gamma k_R}{m}\right)\|\boldsymbol{e}_R\| + \frac{k_v}{m^2 g}\gamma\left(\lambda_{\max}(\boldsymbol{J})\omega^{\max} + k_\omega\right)\|\boldsymbol{\omega}\| \Bigg] \end{aligned} \tag{6.36}$$

Replacing this bound into the expression for $\dot{V}_2$, and rearranging the terms, we get

$$
\begin{aligned}
\dot{V}_2 \leq & -\left[k_\omega - c_2\left(1 + \Big(1 + \frac{\delta}{1-\delta^2}\Big)\frac{k_v}{m^2 g}\gamma(\lambda_{\max}(\boldsymbol{J})\omega^{\max} + k_\omega)\right)\right]\|\boldsymbol{\omega}\|^2 \\
& + \left[\Big(1 + \frac{\delta}{1-\delta^2}\Big)\frac{k_R k_v}{mg}(g + \frac{k_R\gamma}{m}) - c_2\frac{k_R}{\lambda_{\max}(\boldsymbol{J})}\right]\|\boldsymbol{e}_R\|^2 \\
& + \Bigg[c_2\left(\frac{k_\omega}{\lambda_{\min}(\boldsymbol{J})} + \Big(1 + \frac{\delta}{1-\delta^2}\Big)\frac{k_v}{mg}(g + \frac{k_R\gamma}{m})\right) \\
& + k_R\Big(1 + \frac{\delta}{1-\delta^2}\Big)\frac{k_v}{m^2 g}\gamma(\lambda_{\max}(\boldsymbol{J})\omega^{\max} + k_\omega)\Bigg]\|\boldsymbol{e}_R\|\|\boldsymbol{\omega}\| \\
& + \Big(1 + \frac{\delta}{1-\delta^2}\Big)\frac{k_R k_p k_v}{m^2 g}(1 + e_R^{\max})\|\boldsymbol{e}_R\|\|\boldsymbol{e}_p\| \\
& + \Big(1 + \frac{\delta}{1-\delta^2}\Big)\frac{k_R}{mg}\left(|\frac{k_v^2}{m} - k_p| + \frac{k_v^2}{m}e_R^{\max}\right)\|\boldsymbol{e}_R\|\|\boldsymbol{v}\| \\
& + c_2\Big(1 + \frac{\delta}{1-\delta^2}\Big)\frac{k_p k_v}{m^2 g}(1 + e_R^{\max})\|\boldsymbol{\omega}\|\|\boldsymbol{e}_p\| \\
& + c_2\Big(1 + \frac{\delta}{1-\delta^2}\Big)\frac{1}{mg}\left(|\frac{k_v^2}{m} - k_p| + \frac{k_v^2}{m}e_R^{\max}\right)\|\boldsymbol{\omega}\|\|\boldsymbol{v}\|. \qquad (6.37)
\end{aligned}
$$

To make the notation more compact and readable, we introduce the auxiliary variable

$$
\alpha := \left(1 + \frac{\delta}{1-\delta^2}\right)\frac{1}{m^2 g}, \qquad (6.38)
$$

$$
\beta := \lambda_{\max}(\boldsymbol{J})\omega^{\max}. \qquad (6.39)
$$

The previous bound can thus be rewritten in matrix form as

$$
\dot{V}_2 \leq -\boldsymbol{z}_2^\top \boldsymbol{W}_2 \boldsymbol{z}_2 + \boldsymbol{z}_1^\top \boldsymbol{W}_{21}\boldsymbol{z}_2, \qquad (6.40)
$$

where $\boldsymbol{z}_1 = \begin{bmatrix}\|\boldsymbol{e}_p\| & \|\boldsymbol{v}\|\end{bmatrix}^\top$ and $\boldsymbol{z}_2 = \begin{bmatrix}\|\boldsymbol{e}_R\| & \|\boldsymbol{\omega}\|\end{bmatrix}^\top$. The matrices $\boldsymbol{W}_2$ and $\boldsymbol{W}_{21}$ are given by

$$
\boldsymbol{W}_2 = \begin{bmatrix} c_2\frac{k_R}{\lambda_{\max}(\boldsymbol{J})} - k_R k_v \alpha\,(mg + k_R\gamma) & -\frac{\sigma_{R,\omega}}{2} \\ -\frac{\sigma_{R,\omega}}{2} & k_\omega - c_2(1 + k_v\gamma\alpha(\beta + k_\omega)) \end{bmatrix}, \qquad (6.41)
$$

$$
\boldsymbol{W}_{21} = \begin{bmatrix} k_R k_p k_v \alpha(1 + e_R^{\max}) & c_2 k_p k_v \alpha(1 + e_R^{\max}) \\ k_R \alpha m\left(|\frac{k_v^2}{m} - k_p| + \frac{k_v^2}{m}e_R^{\max}\right) & c_2 \alpha m\left(|\frac{k_v^2}{m} - k_p| + \frac{k_v^2}{m}e_R^{\max}\right) \end{bmatrix}. \qquad (6.42)
$$

where $\sigma_{R,\omega} := c_2\left(\frac{k_\omega}{\lambda_{\min}(\boldsymbol{J})} + k_v\gamma\alpha\,(mg + k_R\gamma)\right) + k_R k_v\gamma\alpha(\beta + k_\omega)$.

6.3.3 Combining the Lyapunov Derivative Bounds

In this section, we have derived an upper bound for the time derivative of the Lyapunov candidate derivative $\dot{V}$ as defined in (6.18) by combining the bounds for

$\dot{V}_1$ and $\dot{V}_2$ obtained in Sections 6.3.1 and 6.3.2, respectively. The resulting bound is given by

$$\dot{V} \leq -\boldsymbol{z}_1^\top \boldsymbol{W}_1 \boldsymbol{z}_1 + \boldsymbol{z}_1^\top \tilde{\boldsymbol{W}} \boldsymbol{z}_2 - \boldsymbol{z}_2^\top \boldsymbol{W}_2 \boldsymbol{z}_2, \tag{6.43}$$

where the matrices $\boldsymbol{W}_1$ and $\boldsymbol{W}_2$ are defined in (6.29) and (6.41) respectively. The matrix $\tilde{\boldsymbol{W}}$ is defined as the sum of the matrices $\boldsymbol{W}_{12}$ and $\boldsymbol{W}_{21}$, which are defined in (6.30) and (6.42) respectively.

6.4 Bounding the Lyapunov Candidate

The aims of this section are to establish a lower bound and an upper bound for the Lyapunov candidate function V as defined in (6.15). To achieve this, we will first derive bounds for the components V_1 and V_2 of the Lyapunov candidate, which are defined in (6.16) and (6.17), respectively. We will then combine these bounds to obtain the desired bounds for V.

6.4.1 Bounding the First Lyapunov Candidate

Let us analyze the structure of the Lyapunov candidate V_1 defined in (6.16). We observe that the cross-term $c_1\|\boldsymbol{e}_p\|\|\boldsymbol{v}\|$ can be both positive and negative, depending on the sign of c_1. Therefore, V_1 can be bounded as follows:

$$\frac{1}{2}\boldsymbol{z}_1^\top \boldsymbol{M}_{11} \boldsymbol{z}_1 \leq V_1 \leq \frac{1}{2}\boldsymbol{z}_1^\top \boldsymbol{M}_{12} \boldsymbol{z}_1, \tag{6.44}$$

where the vector $\boldsymbol{z}_1^\top = \begin{bmatrix}\|\boldsymbol{e}_p\| & \|\boldsymbol{v}\|\end{bmatrix}$ has been defined, and the matrices $\boldsymbol{M}_{11}$ and $\boldsymbol{M}_{12}$ are given by

$$\boldsymbol{M}_{11} = \begin{bmatrix} k_p & -c_1 \\ -c_1 & m \end{bmatrix}, \tag{6.45}$$

$$\boldsymbol{M}_{12} = \begin{bmatrix} k_p & c_1 \\ c_1 & m \end{bmatrix}. \tag{6.46}$$

6.4.2 Bounding the Second Lyapunov Candidate

Let us analyze the structure of the Lyapunov candidate V_2 defined in (6.17) in order to derive bounds. To this end, we are going to analyze each term separately. We can bound the first and the last terms by

$$\frac{1}{2}\lambda_{\min}(\boldsymbol{J})\|\boldsymbol{\omega}\|^2 \leq \frac{1}{2}\boldsymbol{\omega}^\top \boldsymbol{J}\boldsymbol{\omega} \leq \frac{1}{2}\lambda_{\max}(\boldsymbol{J})\|\boldsymbol{\omega}\|^2, \tag{6.47}$$

$$-c_2\|\boldsymbol{e}_R\|\|\boldsymbol{\omega}\| \leq c_2 \boldsymbol{e}_R^\top \boldsymbol{\omega} \leq c_2\|\boldsymbol{e}_R\|\|\boldsymbol{\omega}\|. \tag{6.48}$$

As far as the second term is concerned, exploiting the relations in (C.6) for the attitude error function $\Psi(\boldsymbol{R}, \boldsymbol{R}_d)$, we can derive the following bound

$$\frac{1}{2}\|\boldsymbol{e}_R\|^2 \leq \Psi(\boldsymbol{R}, \boldsymbol{R}_d). \tag{6.49}$$

Moreover, in order to solve the translational task, the projection of the reference force $\boldsymbol{f}_r$ along the preferential direction has to be positive, namely

$$\Psi(\boldsymbol{R}(t), \boldsymbol{R}_d(t)) \leq \psi < 1, \quad \forall t \geq 0. \tag{6.50}$$

Under these assumptions, we find the following bound

$$\frac{1}{2-\psi}\|e_R\|^2 \geq \Psi(\boldsymbol{R}, \boldsymbol{R}_d). \tag{6.51}$$

Putting together the bounds in (6.49) and (6.51), we can conclude that

$$\frac{1}{2}\|\boldsymbol{e}_R\|^2 \leq \Psi(\boldsymbol{R}, \boldsymbol{R}_d) \leq \frac{1}{2-\psi}\|\boldsymbol{e}_R\|^2. \tag{6.52}$$

Remark 4 ($e_R^{\max}$)**.** *The maximum value of the attitude error $e_R^{\max}$ can be found exploiting the equation* (5.9) *and the constraint in* (6.50)*. We get*

$$\|\boldsymbol{e}_R\| = \sqrt{\Psi(2-\Psi)} \leq \sqrt{\psi(2-\psi)} =: e_R^{\max}. \tag{6.53}$$

By leveraging the bounds in (6.47), (6.48) and (6.52), we can finally conclude that

$$\frac{1}{2}\boldsymbol{z}_2^\top \boldsymbol{M}_{21}\boldsymbol{z}_2 \leq V_2 \leq \frac{1}{2}\boldsymbol{z}_2^\top \boldsymbol{M}_{22}\boldsymbol{z}_2, \tag{6.54}$$

where

$$\boldsymbol{M}_{21} = \begin{bmatrix} k_R & -c_2 \\ -c_2 & \lambda_{\min}(\boldsymbol{J}) \end{bmatrix}, \tag{6.55}$$

$$\boldsymbol{M}_{22} = \begin{bmatrix} \frac{2k_R}{2-\psi} & c_2 \\ c_2 & \lambda_{\max}(\boldsymbol{J}) \end{bmatrix}. \tag{6.56}$$

6.4.3 Combining the Lyapunov Candidate Bounds

By merging the bounds of V_1 and V_2 respectively expressed in (6.44) and (6.54), we can write

$$\frac{1}{2}\boldsymbol{z}_1^\top \boldsymbol{M}_{11}\boldsymbol{z}_1 + \frac{1}{2}\boldsymbol{z}_2^\top \boldsymbol{M}_{21}\boldsymbol{z}_2 \leq V \leq \frac{1}{2}\boldsymbol{z}_1^\top \boldsymbol{M}_{12}\boldsymbol{z}_1 + \frac{1}{2}\boldsymbol{z}_2^\top \boldsymbol{M}_{22}\boldsymbol{z}_2, \tag{6.57}$$

where the matrices $\boldsymbol{M}_{11}$, $\boldsymbol{M}_{12}$, $\boldsymbol{M}_{21}$ and $\boldsymbol{M}_{22}$ are defined in (6.45), (6.46), (6.55) and (6.56), respectively.

6.5 Final Results

To establish exponential stability of the equilibrium $(\boldsymbol{e}_p, \boldsymbol{v}, \boldsymbol{e}_R, \boldsymbol{\omega}) = (\boldsymbol{0}, \boldsymbol{0}, \boldsymbol{0}, \boldsymbol{0})$, it is sufficient to ensure that the matrices $\boldsymbol{M}_{11}$, $\boldsymbol{M}_{12}$, $\boldsymbol{M}_{21}$, $\boldsymbol{M}_{22}$, $\boldsymbol{W}_1$, and $\boldsymbol{W}_2$ are all positive definite. This requirement can be met by appropriately selecting the parameters c_1 and c_2, as detailed below.

The parameter c_1 must satisfy the following inequality:

$$c_1 < \min\left\{\sqrt{m\,k_p},\ k_v\,(1-e_R^{\max}),\ \frac{4\,k_p\,k_v\,m\,(e_R^{\max}-1)^2}{k_v^2\,(e_R^{\max}+1)^2+4\,k_p\,m\,(1-e_R^{\max})}\right\}.$$

This ensures the positive definiteness of the associated matrices.

For c_2, a set of inequalities must be satisfied

$$\begin{aligned} c_2 &< \min\left\{\sqrt{\lambda_{\min}(\boldsymbol{J})k_R},\ \frac{k_\omega}{1+k_v\gamma\alpha(\beta+k_\omega)},\ c_{2,+}\right\},\\ c_2 &> \max\left\{k_v\lambda_{\max}(\boldsymbol{J})\alpha(mg+k_R\gamma),\ c_{2,-}\right\}. \end{aligned}$$

A rigorous derivation of the conditions presented in (6.8), as well as the bounds in (6.9) and (6.10), is provided in Appendix E, to which the interested reader is referred for further details.

With the above parameter choices, the Lyapunov candidate function V is bounded as follows:

$$\lambda_{\min}(\boldsymbol{M}_{11})\|\boldsymbol{z}_1\|^2+\lambda_{\min}(\boldsymbol{M}_{21})\|\boldsymbol{z}_2\|^2 \le V \le \lambda_{\max}(\boldsymbol{M}_{12})\|\boldsymbol{z}_1\|^2+\lambda_{\max}(\boldsymbol{M}_{22})\|\boldsymbol{z}_2\|^2.$$

Furthermore, its time derivative can be bounded by

$$\dot{V} \le -\lambda_{\min}(\boldsymbol{W}_1)\|\boldsymbol{z}_1\|^2+\|\tilde{\boldsymbol{W}}\|\|\boldsymbol{z}_1\|\|\boldsymbol{z}_2\|-\lambda_{\min}(\boldsymbol{W}_2)\|\boldsymbol{z}_2\|^2.$$

This can be compactly expressed as

$$\dot{V} \le -\begin{bmatrix}\|\boldsymbol{z}_1\| & \|\boldsymbol{z}_2\|\end{bmatrix}\begin{bmatrix}\lambda_{\min}(\boldsymbol{W}_1) & -\frac{\|\tilde{\boldsymbol{W}}\|}{2}\\ -\frac{\|\tilde{\boldsymbol{W}}\|}{2} & \lambda_{\min}(\boldsymbol{W}_2)\end{bmatrix}\begin{bmatrix}\|\boldsymbol{z}_1\|\\ \|\boldsymbol{z}_2\|\end{bmatrix}.$$

Finally, to guarantee that $\dot{V}$ is negative definite, the matrix above must be positive definite. This is equivalent to requiring

$$\|\tilde{\boldsymbol{W}}\|^2 < 4\lambda_{\min}(\boldsymbol{W}_1)\lambda_{\min}(\boldsymbol{W}_2).$$

By ensuring all the above conditions are satisfied, exponential stability of the equilibrium is guaranteed.

Part V

Simulations and Conclusion

Chapter 7

Simulations and Results

This chapter presents and analyzes the simulation results employed to evaluate the proposed control strategy and to validate its stability properties for the partially-coupled, underactuated floating vehicle dynamics.

7.1 Overview

We will focus on the generically tilted multirotor family, introduced in Section 5.1, which all share the dynamic model described by (2.22). The control law implemented on these vehicles is described in detail in Chapter 5. In particular, given the reference control whrench composed by the reference control force $\boldsymbol{f}_r$ (see (5.4)) and the reference control moment $\boldsymbol{\tau}_r$ (see (5.10)), it is processed by the wrench mapper, defined in Section 5.3.3, which computes the reference control inputs $\boldsymbol{u}_r$ to be sent to the vehicle model.

By closing the loop—i.e., applying the reference control input $\boldsymbol{u}_r$ to the open-loop system (2.22)—the following closed-loop dynamics are obtained:

$$\begin{cases} \dot{\boldsymbol{p}} & = \boldsymbol{v}, \\ m\dot{\boldsymbol{v}} & = -mg\boldsymbol{e}_3 + \boldsymbol{f}_r + \boldsymbol{X} + \boldsymbol{P}_\star^\perp \boldsymbol{R}\boldsymbol{F}_1\boldsymbol{F}_2^\dagger \boldsymbol{\tau}_r, \\ \dot{\boldsymbol{R}} & = \boldsymbol{R}\boldsymbol{S}(\boldsymbol{\omega}), \\ \boldsymbol{J}\dot{\boldsymbol{\omega}} & = -\boldsymbol{\omega} \times \boldsymbol{J}\boldsymbol{\omega} + \boldsymbol{\tau}_r, \end{cases} \tag{7.1}$$

where the term $\boldsymbol{P}_\star^\perp \boldsymbol{R}\boldsymbol{F}_1\boldsymbol{F}_2^\dagger \boldsymbol{\tau}_r$, already seen in (5.21), is referred to as the *spurious force.*

It is essential to note that this closed-loop structure is common to all GTMs within the family under consideration. At first glance, this might suggest that the spurious force phenomenon affects all vehicles in the family. However, this is not necessarily true: not all GTMs are subject to spurious force generation and, even when present, depending on the actuation capabilities of the vehicle under consideration, their effects may be negligible or completely mitigated. For example, *fully actuated* GTMs[1] are able to counterbalance the spurious force by appropriately selecting the reference control force $\boldsymbol{f}_r$.

---

[1] These platforms correspond to those denoted as D3 in Definition (3.2). Achieving this configuration requires $n \geq 6$ propellers and $\mathrm{rank}(\boldsymbol{F}) = 6$, i.e., the platform must be *omnidirectional.*

Similarly, the so-called *completely decoupled* GTMs[2] are not affected by the presence of spurious force. In such cases, although spurious force is present, since it resides in the subspace along which control authority is available, it is always possible to select $\boldsymbol{f}_r$ so as to completely compensate for its effects.

The most critical scenario occurs with *partially coupled* GTMs, in which there is a spurious force that cannot be compensated by any choice of $\boldsymbol{f}_r$, since it is located in the orthogonal subspace to that along which it is possible to generate thrust without affecting the dynamics of the attitude. Consequently, the simulations presented in this chapter focus on this type of vehicle.

We notice that the spurious force is absent from the closed-loop system if and only if the product $\boldsymbol{F}_1\boldsymbol{F}_2^\dagger$ is zero, which occurs precisely when all rows of $\boldsymbol{F}_1$ are orthogonal to all rows of $\boldsymbol{F}_2$. In fact, it can be shown that

$$\text{if} \quad \boldsymbol{F}_1\boldsymbol{F}_2^\dagger = \boldsymbol{0}, \quad \Rightarrow \quad \text{rank}(\boldsymbol{F}) = \text{rank}(\boldsymbol{F}_1) + \text{rank}(\boldsymbol{F}_2). \tag{7.2}$$

This result stems from the fact that the orthogonality of the image spaces of $\boldsymbol{F}_1$ and $\boldsymbol{F}_2$ implies that their intersection is trivial. Since the rows of $\boldsymbol{F}$ are obtained by stacking those of $\boldsymbol{F}_1$ and $\boldsymbol{F}_2$, the image space of $\boldsymbol{F}$ is the sum of the image spaces of $\boldsymbol{F}_1$ and $\boldsymbol{F}_2$. When the intersection of these spaces is trivial, this sum is direct, which means that the dimension of the image space of $\boldsymbol{F}$ is given by the sum of the dimensions of the image spaces of $\boldsymbol{F}_1$ and $\boldsymbol{F}_2$. In summary, when the rows of $\boldsymbol{F}_1$ and $\boldsymbol{F}_2$ are linearly independent, the rank of $\boldsymbol{F}$ is equal to the sum of the ranks of $\boldsymbol{F}_1$ and $\boldsymbol{F}_2$.

It should be emphasized that the relation (7.2) provides only a necessary condition for the absence of the spurious force. Conversely, if $\text{rank}(\boldsymbol{F}) \neq \text{rank}(\boldsymbol{F}_1) + \text{rank}(\boldsymbol{F}_2)$, the product $\boldsymbol{F}_1\boldsymbol{F}_2^\dagger$ is non-zero, and thus the spurious force should be present in the closed-loop system. Since our focus is on partially-coupled GTMs, exploiting (7.2) allows us to identify specific platforms within this family that are certainly affected by the spurious force phenomenon. Notable examples include tilted quadrotors and tilted pentarotors.

Consider, for instance, a tilted quadrotor, which is a GTM with $n = 4$ propellers and $\text{rank}(\boldsymbol{F}) = 4$. Given that any platform in our family must satisfy (3.1), i.e., $\text{rank}(\boldsymbol{F}_2) = 3$, it follows that the tilted quadrotor is certainly subject to the spurious force whenever $\text{rank}(\boldsymbol{F}_1) \geq 2$. Similarly, for a tilted pentarotor ($n = 5$, $\text{rank}(\boldsymbol{F}) = 5$), the same condition implies the presence of the spurious force when $\text{rank}(\boldsymbol{F}_1) = 3$.

In conclusion, the primary objective of this chapter was to conduct simulations on partially-coupled GTMs, with a particular focus on identifying platforms within this family that are unequivocally affected by the spurious force phenomenon. Through the analysis presented above, we have established that the tilted quadrotor and the tilted pentarotor are representative examples of such platforms. Consequently, the simulations in the following sections will be carried out on a tilted quadrotor, as it serves as a canonical case study for investigating the effects of the spurious force in partially-coupled configurations.

---

[2] These platforms correspond to those indicated with FD in Definition (3.1). This scenario occurs when the spurious force resides within the subspace along which thrust can be generated without affecting the attitude dynamics. This definition also includes the D3 platforms mentioned above.

7.2 Simulation Environment

In this section, we present the vehicle used in the simulations and discuss the choices made regarding the parameters of the control law.

In this study, we consider a tilted quadrotor configuration, characterized by the following properties: $\mathrm{rank}(\boldsymbol{F}_1) \geq 2$, $\mathrm{rank}(\boldsymbol{F}_2) = 3$, and $\mathrm{rank}(\boldsymbol{F}) = 4$. To realize such configuration, the tilt angles of the propellers are set as follows:

$$\alpha_i = (-1)^{i-1} 35^\circ, \qquad \beta_i = (-1)^{i-1} 25^\circ, \qquad \text{for } i = 1, \ldots, 4$$

This choice ensures that both the control force and moment input matrices have rank 3, while the overall control input matrix in (2.18) achieves full rank, i.e., $\mathrm{rank}(\boldsymbol{F}) = 4$. This choice of tilt angles is not the unique combination that satisfies this condition; however, it is a suitable one that allows for the investigation of the control strategy's performance under the specified conditions.

In light of the above considerations, a star-shaped quadcopter configuration (with $\phi = 0$) is examined, as it possesses the structural properties of primary interest for this study. This lends itself to an analysis of the effects of partial coupling and spurious forces.

The quadcopter is equipped with four identical propellers, each characterized by a thrust coefficient c_f and a drag coefficient c_τ^+, which are the same for all propellers. Each individual propeller can provide a maximum thrust of 15 N. The diameter of the platform is 1.05 m and the total mass is $m = 3\,\mathrm{kg}$. The inertia matrix is diagonal and expressed in the fixed reference system $\mathcal{F}_B$. The parameters are summarized in Table 7.1.

Table 7.1. Quadrotor parameters used in simulations.

Parameter	Symbol	Value
Mass	m	3 kg
Inertia	$\boldsymbol{J}$	$\mathrm{diag}(0.050, 0.052, 0.080)\,\mathrm{kg\,m^2}$
Thrust coefficient	c_f	0.01 kg m
Drag coefficient	c_τ^+	$0.002\,\mathrm{kg\,m^2}$
Arm length	l	0.525 m

The arrangement of the four propellers is illustrated in Fig. 7.1, where each rotor is positioned at the vertices of a square such that each vertex is at a distance l from the center of the body-fixed reference frame $\mathcal{F}_B$. The figure also shows the spinning axes of each propeller, tilted according to the angles α_i and β_i defined previously.

A CAD rendering of the prototype, created using Blender by adapting a 3D model sourced from CGTrader[3] is shown in Fig. 7.2.

With the parameters described above, the control input matrix takes the following

---

[3] A marketplace for 3D models for VR/AR and CG projects, and a community of professional 3D designers.

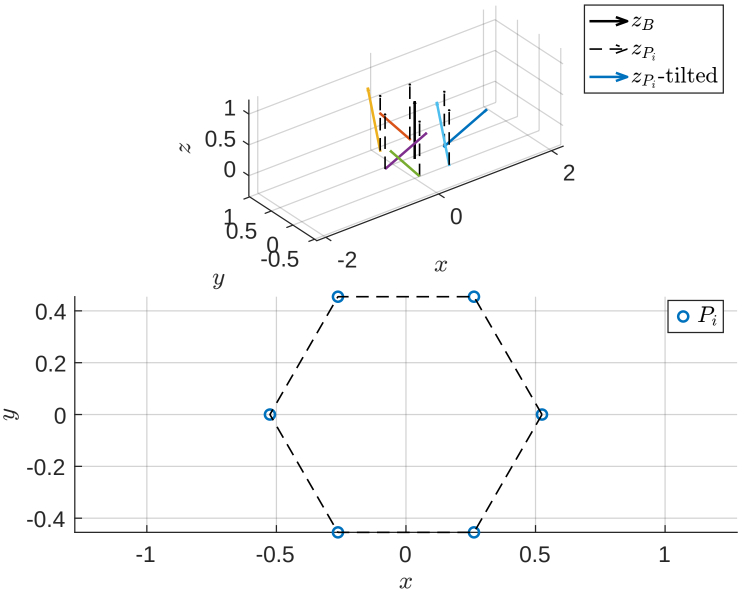

Figure 7.1. Propeller configuration: positions at the vertices of a square with each vertex at distance l from the center, and orientation of the tilted thrust axes.

Figure 7.2. CAD rendering of the tilted quadrotor prototype.

form:

$$\boldsymbol{F} = \begin{bmatrix} 0.0042 & -0.0052 & -0.0042 & 0.0052 \\ -0.0052 & -0.0042 & 0.0052 & 0.0042 \\ 0.0074 & 0.0074 & 0.0074 & 0.0074 \\ -0.0008 & 0.0029 & 0.0008 & -0.0029 \\ -0.0029 & -0.0008 & 0.0029 & 0.0008 \\ -0.0042 & 0.0042 & -0.0042 & 0.0042 \end{bmatrix}. \tag{7.3}$$

The control strategy provided in this thesis is implemented in MATLAB-Simulink, where the quadrotor dynamics are simulated with a sampling time of 0.002 s, corresponding to a simulation frequency of 500 Hz.

To implement the control law introduced in Chapter 5, and in accordance with the requirements of Proposition 4.2, it is necessary to select a unit vector $\hat{\boldsymbol{b}} \in \ker(\boldsymbol{F}_2)$

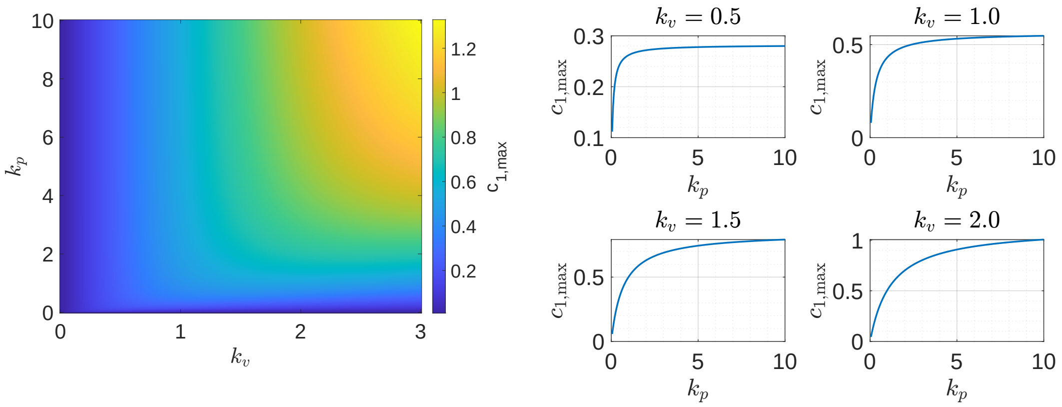

Figure 7.3. **(a)**: Colormap of the admissible range of c_1 as a function of the gains k_p and k_v. Each point in the (k_p, k_v) plane is assigned a color representing the width of the interval in which c_1 can be chosen; warmer colors indicate larger maximum values of c_1. **(b)**: Maximum values of c_1 with respect to k_p for different fixed values of k_v.

such that $\boldsymbol{F}_1\hat{\boldsymbol{b}} \neq 0$. Considering the structural characteristics of the quadrotor under study, the following unit vector is:

$$\hat{\boldsymbol{b}} = \frac{1}{2}\begin{bmatrix}1 & 1 & 1 & 1\end{bmatrix}^\top. \tag{7.4}$$

Accordingly, the preferential direction associated with this choice, as defined in (4.9), is given by:

$$\boldsymbol{d}_\star = \begin{bmatrix}0 & 0 & 1\end{bmatrix}^\top = \boldsymbol{e}_3. \tag{7.5}$$

This direction is expressed in the body-fixed frame $\mathcal{F}_B$ and it can be interpreted as the thrust direction of the quadrotor, which is aligned with the vertical axis of the body frame.

The choice of gains requires the simultaneous satisfaction of conditions (6.8), (6.9), (6.10), and (6.11). Collectively, these constraints delineate a feasible domain in the gain parameter space, called the *set of admissible gains*, within which there exist positive constants c_1 and c_2 such that all the required inequalities are satisfied. Formally, this region is defined as

$$\mathcal{G} := \{k_p, k_v, k_R, k_\omega > 0 \mid \exists\, c_1, c_2 > 0 \text{ such that } (6.8), (6.9), (6.10), \text{ and } (6.11) \text{ hold}\}.$$

It is important to distinguish $\mathcal{G}$ from the region of attraction introduced in (6.14), which characterizes the set of initial conditions for which closed-loop stability is guaranteed. In contrast, the region of admissible gains $\mathcal{G}$ specifies the set of controller parameters that ensure the existence of a Lyapunov function certifying stability.

The simultaneous satisfaction of the conditions (6.8), (6.9) and (6.10) individuates two regions in the gain parameter space, which are shown in Fig.7.3 and in Fig.7.4.

The first region, illustrated in Fig. 7.3, is determined by condition (6.8) and delineates the admissible values of c_1 as a function of the gains k_p and k_v. The second region, depicted in Fig. 7.4, is defined by conditions (6.9) and (6.10), and characterizes the admissible values of c_2 as a function of the gains k_p, k_v, and

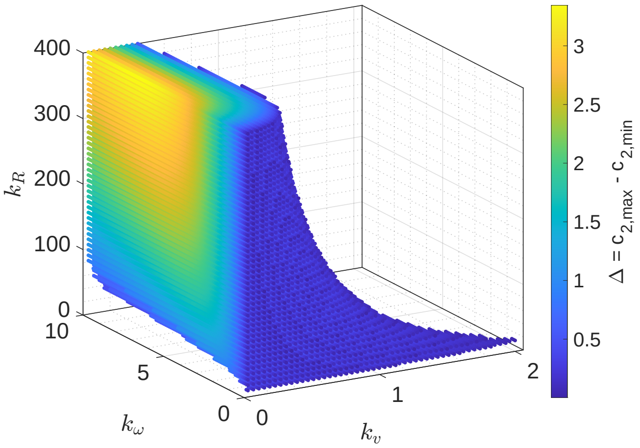

Figure 7.4. 3D volume of the admissible range of c_2 as a function of the gains k_p, k_v, and k_R. Each point in the (k_p, k_v, k_R) space is assigned a color representing the width of the interval in which c_2 can be chosen; warmer colors indicate larger maximum values of c_2.

k_R. A feasible selection of gains must reside within the intersection of these two regions, thereby ensuring that all required conditions are satisfied simultaneously. Accordingly, the following set of gains is adopted:

$$k_p = 0.55, \quad k_v = 2.06, \quad k_R = 8.16, \quad k_\omega = 0.7 \tag{7.6}$$

With this selection, the maximum admissible value for c_1 is $c_1^{\max} = 0.346885$, while the admissible interval for c_2 is $[c_2^{\min}, c_2^{\max}] = [0.181705, 0.219184]$. Now we just need to choose the values of c_1 and c_2 from among those that are admissible to satisfy the last condition expressed in (6.11).

It is important to note that the intersection of the admissible regions in the gain parameter space, as determined above, is not necessarily the largest possible. In fact, the region $\mathcal{G}$ could be enlarged by using tighter (less conservative) upper bounds during the derivations in Chapter 6. The conservative choices made in the proofs, in particular in the estimation of the various upper bounds, limit the size of the admissible region. However, the gains selected in (7.6) are sufficient to guarantee closed-loop stability in accordance with Proposition 6.1.

To make the simulations more realistic, the control vector $\boldsymbol{u}$ is routed through a Brownian noise block before reaching the quadcopter model. This block implements an Ornstein-Uhlenbeck process, sampled every 2 ms, with an exponential decay rate $s = 0.1$. A noise amplitude of 0.2, combined with a frequency factor of 2, produces a standard deviation at steady state of 0.89.

Furthermore, to ensure that no single propeller exceeds its maximum thrust of 15 N, a saturation block has been incorporated into the Simulink model. This mechanism simulates the physical limits of the actuators, preventing the control signals from exceeding the permitted limits and thus preserving the stability of the system and the integrity of the actuators during operation.

7.3 Simulation Results

Numerical simulations are conducted to validate the proposed control strategy and evaluate its performance in stabilizing the dynamics of a partially coupled and underactuated floating vehicle.

We will perform stationary flight maneuvers, in which the vehicle is tasked with maintaining a fixed spatial position and orientation, as formally defined in Definition 4.4. We will perform these maneuvers while trying to diversify the initial conditions of the quadcopter, both in translation and orientation.

The performance of the control strategy is evaluated by observing how the position, velocity, angular velocity, attitude tracking errors, and other important parameters change during the maneuver.

7.3.1 Standard Manoeuvre

The first scenario analyzed is a standard case, i.e., a maneuver in which the quadcopter has to perform static hovering, starting from zero initial conditions. Specifically, the quadcopter is initialized at the origin with zero velocity and an attitude aligned with the inertial system. The simulation is performed for a total duration of 25 s.

The initial conditions are:

$$\begin{aligned} \boldsymbol{p}(0) &= \begin{bmatrix} 0 & 0 & 0 \end{bmatrix}^\top, & \boldsymbol{v}(0) &= \begin{bmatrix} 0 & 0 & 0 \end{bmatrix}^\top, \\ \boldsymbol{R}(0) &= \boldsymbol{I}_3, & \boldsymbol{\omega}(0) &= \begin{bmatrix} 0 & 0 & 0 \end{bmatrix}^\top. \end{aligned}$$

The objective is to realize stitc hovering at a fixed position and orientation, specified as

$$\boldsymbol{p}_r = \begin{bmatrix} 15 & 10 & 20 \end{bmatrix}^\top, \qquad \boldsymbol{R}_r \boldsymbol{e}_1 = \begin{bmatrix} 1 & 0 & 0 \end{bmatrix}^\top. \tag{7.7}$$

The screenshots shown in Figure 7.5 were extracted from the simulation video of the 3D CAD model of the quadcopter. They illustrate, at significant moments, the evolution of the vehicle's position and attitude during the transition phase to the desired hovering position, providing a visual assessment of the system's behavior and its progressive convergence towards the reference configuration.

Fig. 7.6 shows the position components, which demonstrate that the quadcopter successfully reaches the reference position $\boldsymbol{p}_r$ and maintains it throughout the simulation.

Figure 7.7 shows how the velocity and angular velocity components change over time. Both sets of components are set to zero, as needed for static hovering.

As shown in Figure 7.8, the attitude evolution shows a correct alignment of the quadcopter's attitude with the desired orientation. In particular, it is evident that the attitude error components $\boldsymbol{e}_R$ and the attitude error function $\Psi(\boldsymbol{R}, \boldsymbol{R}_d)$ both converge to zero. It is important to note that the attitude error function is always less than 1 during the entire simulation. This observation indicates that the condition (6.7) described in Proposition (6.1) is satisfied.

Figure 7.9 shows the evolution of the control inputs over time during the entire maneuver. The graph shows both the propeller spinning rates $\boldsymbol{u}$ and the corresponding thrust generated by each rotor. It is important to note that, for the current

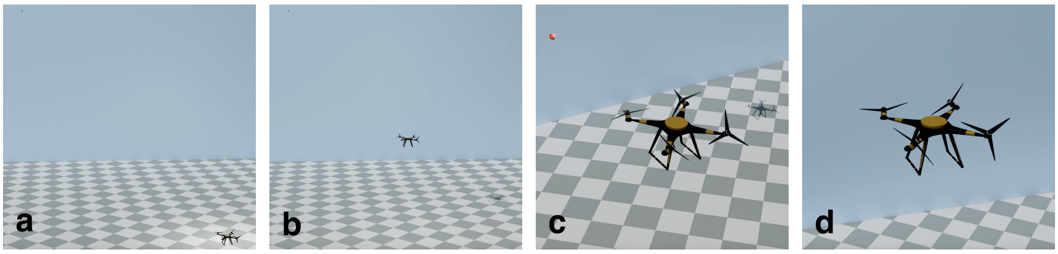

Figure 7.5. Sequence of screenshots from the 3D CAD model of the quadrotor at four distinct instants during the flight manoeuvre, to be read from left to right: **(a)** the drone starts from the initial position (maximum distance from the reference), **(b)** the drone is halfway and approaching $\boldsymbol{p}_r$, **(c)** the point of view changes and the drone is almost at $\boldsymbol{p}_r$, **(d)** the drone has reached $\boldsymbol{p}_r$ and is performing static hovering.

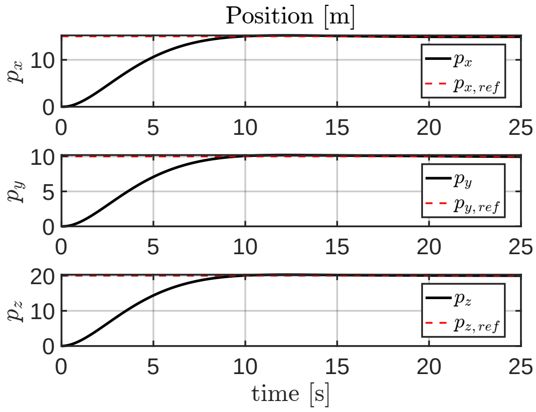

Figure 7.6. Position of the quadrotor during the overall manoeuvre. It can be seen how the position $\boldsymbol{p}$ converge to the reference position $\boldsymbol{p}_r$.

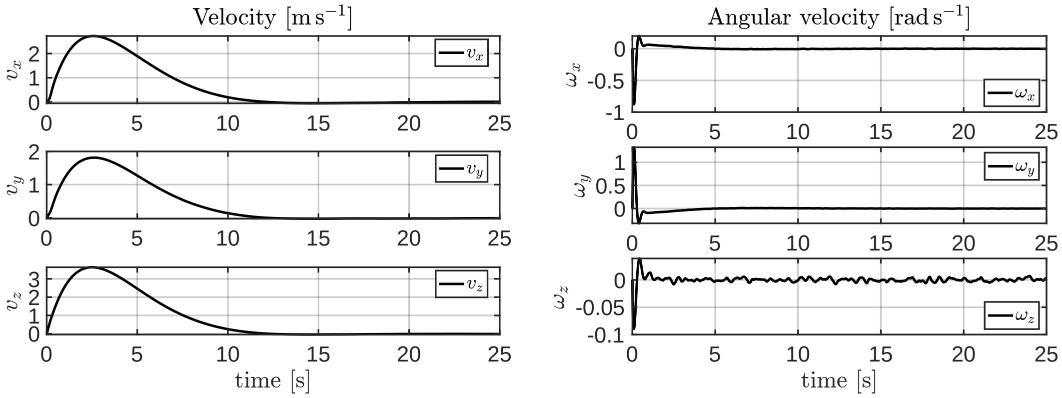

Figure 7.7. Time evolution of the quadrotor's linear and angular velocity components throughout the entire simulation, highlighting convergence. **(a)**: Velocity components $\boldsymbol{v}$, **(b)**: Angular velocity components $\boldsymbol{\omega}$.

maneuver, actuator saturation is not invoked; the control inputs remain well within the saturation limits imposed during the entire simulation.

Finally, Figure 7.10 presents the time histories of the spurious force (panel **(a)**) and the desired angular velocity (panel **(b)**) during the manoeuvre. Notably, both

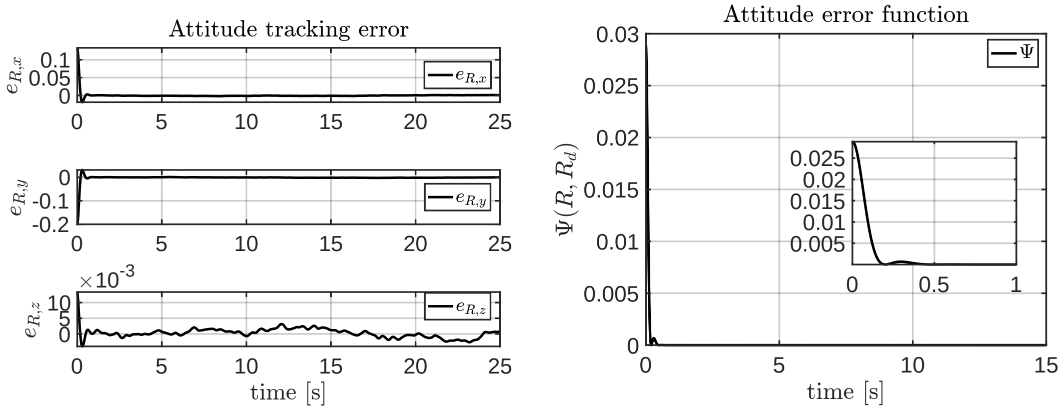

Figure 7.8. Time evolution of the quadrotor's attitude during the entire simulation. **(a)**: Attitude tracking error components $\boldsymbol{e}_R$, **(b)**: Attitude error function $\Psi(\boldsymbol{R}, \boldsymbol{R}_d)$.

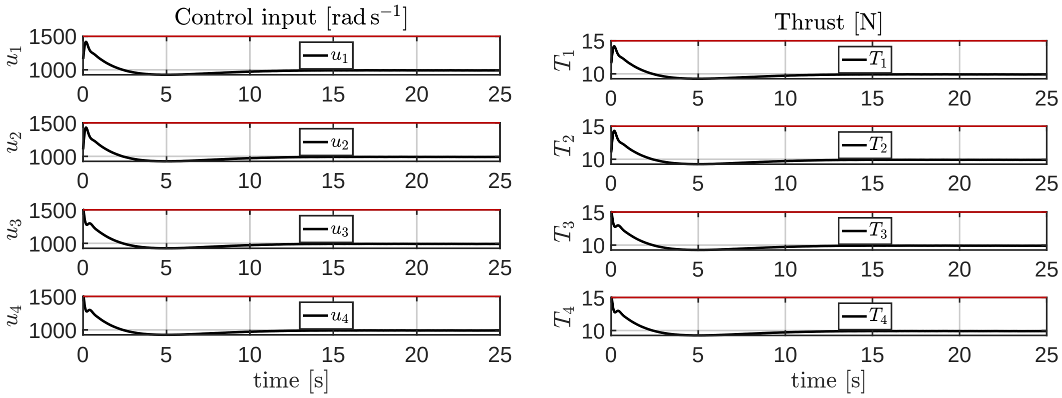

Figure 7.9. Temporal evolution of the control inputs during the whole simulation. **(a)**: Spinning rates $\boldsymbol{u}$, **(b)**: Thrusts T_i generated by each rotor. The control inputs remain well within the imposed saturation limits throughout the entire simulation.

signals converge to zero and remain negligible, underscoring the effectiveness of the control law in actively suppressing spurious forces that could otherwise compromise the control objective. This effect is particularly evident in the evolution of the desired angular velocity, which is consistently driven to zero, thereby preventing excitation of the spurious force.

7.3.2 Complex Manoeuvre

In this section, we analyze a more complex maneuver designed to test the control strategy by bringing some variables close to the stability limits established in Proposition 6.1. The initial conditions for this maneuver are:

$$\begin{aligned} \boldsymbol{p}(0) &= \begin{bmatrix} 0 & 0 & 3 \end{bmatrix}^\top, & \boldsymbol{v}(0) &= \begin{bmatrix} 0 & 0 & 0 \end{bmatrix}^\top, \\ \boldsymbol{R}(0) &= \boldsymbol{I}_3, & \boldsymbol{\omega}(0) &= \begin{bmatrix} 0 & 0 & 0 \end{bmatrix}^\top. \end{aligned}$$

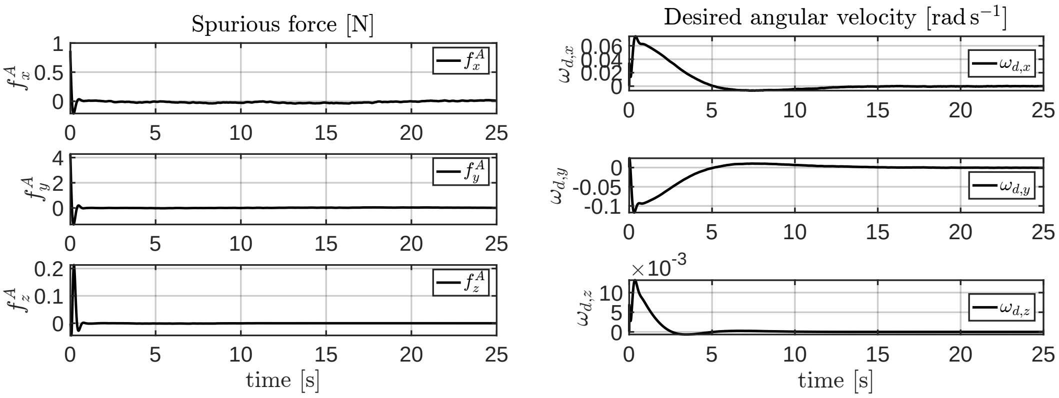

Figure 7.10. Spurious force and desired angular velocity evolution during the manoeuvre. **(a)**: Spurious force $\boldsymbol{f}_s$, **(b)**: Desired angular velocity $\boldsymbol{\omega}_d$. The convergence of both signals to zero is indicative of the efficacy of the control law in mitigating the spurious force effects.

The quadrotor is required to reach the following reference position and orientation:

$$\boldsymbol{p}_r = \begin{bmatrix} 50 & 50 & 3 \end{bmatrix}^\top, \qquad \boldsymbol{R}_r \boldsymbol{e}_1 = \begin{bmatrix} 1 & 0 & 0 \end{bmatrix}^\top. \tag{7.8}$$

The manoeuvre involves static hovering in a position that is much farther away from the drone's initial position, while keeping an altitude that is the same as the drone's initial altitude. The simulation is run for 30s.

The screenshots shown in Figure 7.11 were extracted from the simulation video of the 3D CAD model of the quadcopter, in which it is possible to observe the salient moments of the entire manoeuvre and the pose of the quadcopter itself.

Figure 7.12 illustrates the evolution of the position components during the complex manoeuvre. The quadrotor is able to reach the reference position $\boldsymbol{p}_r$ and maintain it for the remainder of the simulation, despite the increased difficulty of the task.

The time histories of the linear and angular velocity components are shown in Figure 7.13. Both sets of variables converge to zero, as required for static hovering at the target location.

Figure 7.14 shows the evolution of the components of the attitude tracking error $\boldsymbol{e}_R$ and the attitude error function $\Psi(\boldsymbol{R}, \boldsymbol{R}_d)$. Both quantities converge to zero as the maneuver progresses. In particular, the error function Ψ remains below 1 throughout the simulation, thus satisfying the stability condition, but reaches relatively high values at the beginning of the maneuver. This initial peak reflects the significant discrepancy between the initial and desired attitude of the quadcopter, as the vehicle must tilt significantly to generate the horizontal thrust necessary to move quickly toward the target position.

Figure 7.15 presents the control inputs over time. In this more challenging scenario, the inputs remain at the saturation limits for a significant portion of the manoeuvre, reflecting the increased effort required from the actuators. Nevertheless, the controller is still able to achieve the desired objective.

Figure 7.16 shows the projection of the reference control force $\boldsymbol{f}_r$ onto the heading direction $\boldsymbol{R}_r \boldsymbol{e}_1$ during the complex maneuver. Initially, this projection reaches a

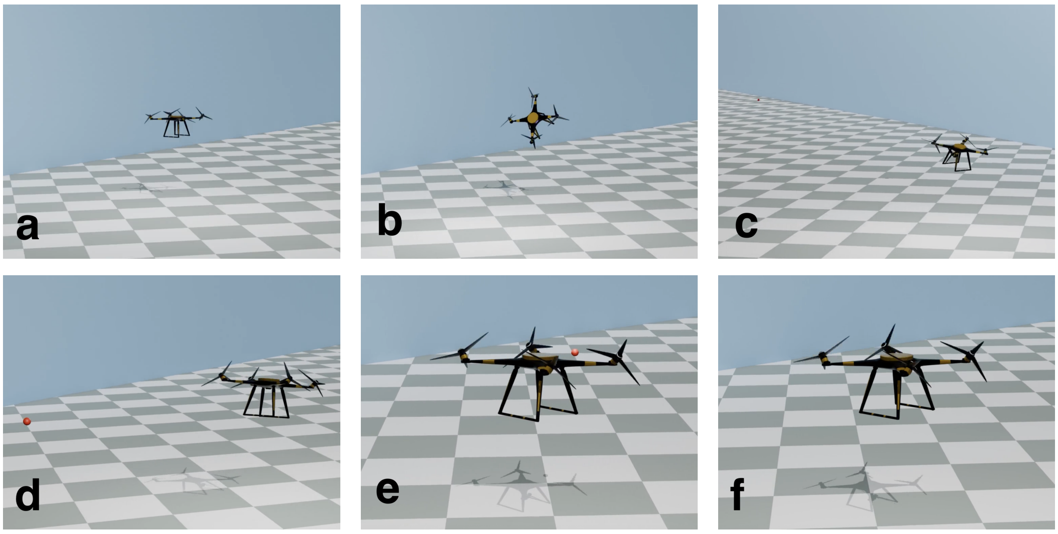

Figure 7.11. Sequence of screenshots from the 3D CAD model of the quadrotor at six distinct instants during the complex manoeuvre. The images should be read from left to right. **(a)**: The quadrotor starts from $\boldsymbol{p}(0)$. **(b)**: The quadrotor tilts significantly as it accelerates towards $\boldsymbol{p}_{\mathrm{r}}$. **(c)**: The quadrotor is approaching $\boldsymbol{p}_{\mathrm{r}}$. **(d)**: Camera changes; the quadrotor has almost reached $\boldsymbol{p}_{\mathrm{r}}$, and its tilt indicates it is braking. **(e)**: The quadrotor overshoots $\boldsymbol{p}_{\mathrm{r}}$. **(f)**: The quadrotor finally reaches $\boldsymbol{p}_{\mathrm{r}}$ and performs static hovering.

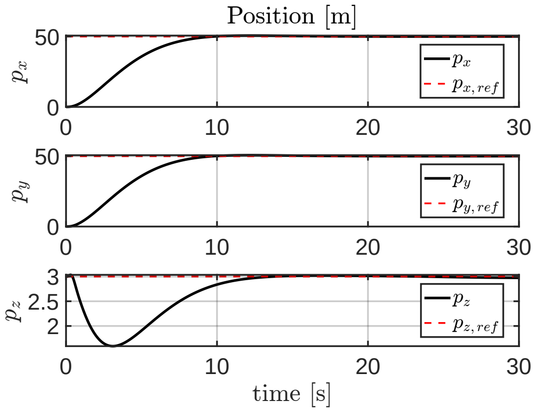

Figure 7.12. Quadrotor position throughout the complex manoeuvre. The position $\boldsymbol{p}$ converges to the reference $\boldsymbol{p}_r$.

value close to 0.6, reflecting the substantial tilt required by the quadcopter to generate the horizontal thrust necessary for rapid acceleration towards the target position. As the vehicle approaches the reference point, the projection decreases and eventually becomes negative (approximately -0.2), indicating that the quadcopter must reorient itself to produce a braking force, thus enabling precise and stable hovering in the final position.

Finally, Figure 7.17 illustrates the evolution of the spurious force and the desired angular velocity during the maneuver. In this complex scenario, the spurious force $\boldsymbol{f}^A$ reaches higher values than in the previous case, particularly at the beginning, due to the larger initial deviation between $\boldsymbol{R}(0)$ and $\boldsymbol{R}_d(0)$. Nevertheless, the control

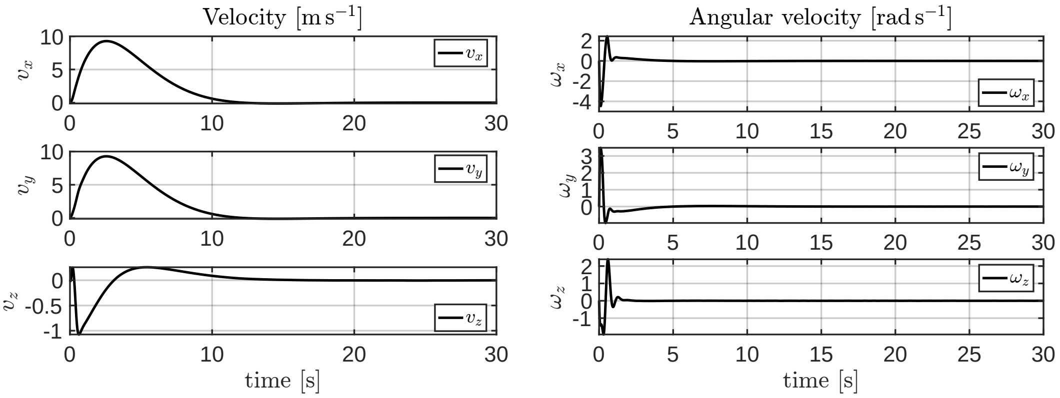

Figure 7.13. Time evolution of the quadrotor's linear and angular velocities during the complex manoeuvre. **(a)**: Linear velocity $\boldsymbol{v}$, **(b)**: Angular velocity $\boldsymbol{\omega}$.

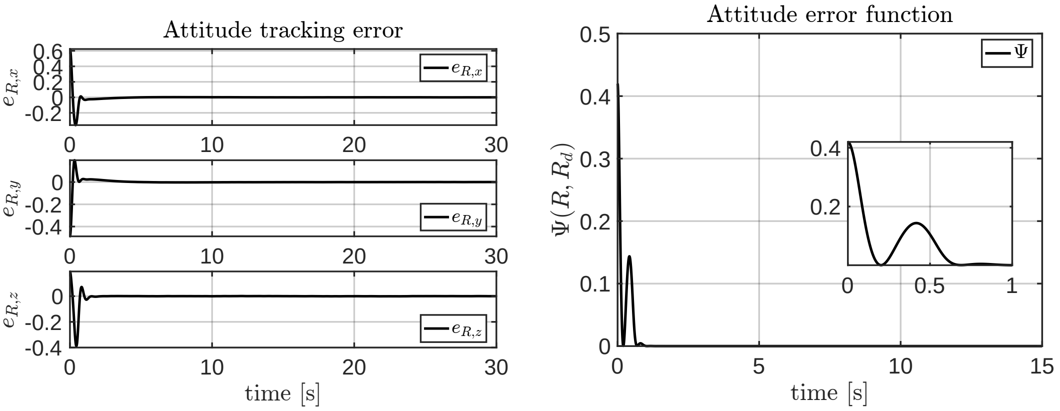

Figure 7.14. Attitude tracking performance during the complex manoeuvre. **(a)**: Attitude error components $\boldsymbol{e}_R$, **(b)**: Attitude error function $\Psi(\boldsymbol{R}, \boldsymbol{R}_d)$. The error function remains below one, satisfying the stability condition; however, in this more challenging scenario, Ψ reaches high values, approaching the stability guarantee limits.

strategy effectively regulates the spurious force to zero as the maneuver progresses. Similarly, the desired angular velocity $\boldsymbol{\omega}_d$ is effectively brought to zero, confirming the effectiveness of the proposed approach.

7.3.3 Reorienting Manoeuvre

In this section, we analyze a reorientation maneuver in which the quadcopter must restore its attitude to maintain a fixed position. The initial conditions are:

$$\boldsymbol{p}(0) = \begin{bmatrix} 0 & 0 & 0 \end{bmatrix}^\top, \quad \boldsymbol{R}(0) = \begin{bmatrix} 1 & 0 & 0 \\ 0 & 0.01745 & -0.99985 \\ 0 & 0.99985 & 0.01745 \end{bmatrix},$$

$$\boldsymbol{v}(0) = \begin{bmatrix} 0 & 0 & 0 \end{bmatrix}^\top, \quad \boldsymbol{\omega}(0) = \begin{bmatrix} 0 & 0 & 0 \end{bmatrix}^\top,$$

where $\boldsymbol{R}(0)$ corresponds to a rotation of 89° about the $\boldsymbol{x}_B$-axis. The quadrotor is commanded to hover at the same position, with the desired heading direction

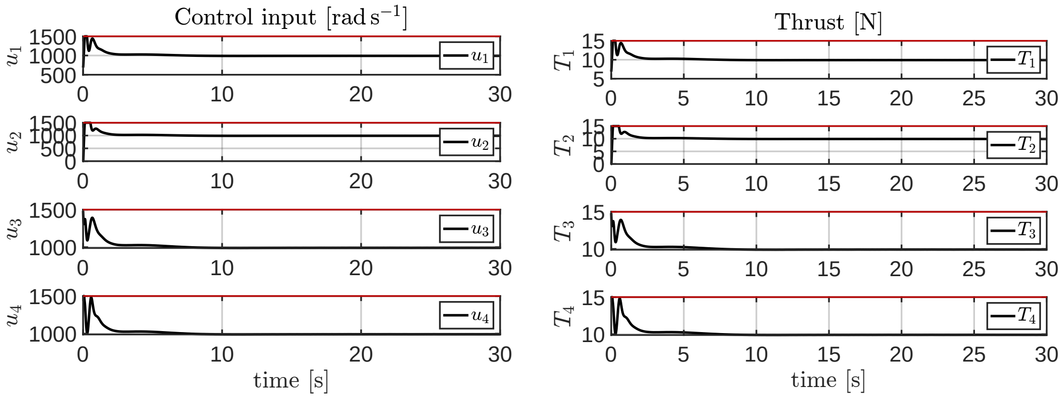

Figure 7.15. Control input evolution during the complex manoeuvre. **(a)**: Spinning rates $\boldsymbol{u}$, **(b)**: Individual rotor thrusts T_i. In this more challenging scenario, the inputs remain at the saturation limits for a significant portion of the manoeuvre, reflecting the increased effort required from the actuators.

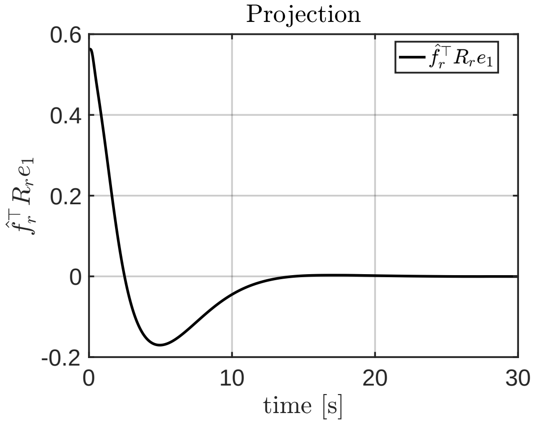

Figure 7.16. Projection of the reference control force direction $\hat{\boldsymbol{f}}_r$ onto the heading direction $\boldsymbol{R}_r\boldsymbol{e}_1$. Notice how this projection varies throughout the manoeuvre from positive to negative values, indicating the need for both acceleration and braking.

$\boldsymbol{R}_r\boldsymbol{e}_1 = \begin{bmatrix}1 & 0 & 0\end{bmatrix}^\top$.

This configuration causes the initial direction of thrust, $\boldsymbol{R}(0)\boldsymbol{d}_\star$, to be almost orthogonal to the direction of the reference control force, $\boldsymbol{R}_d\boldsymbol{d}_\star$, required for stationary flight. As a result, the quadcopter must perform a significant reorientation to align its thrust with the desired direction while maintaining its position unchanged. The simulation lasts 15 s.

The screenshots in Figure 7.18 illustrate the evolution of the reorientation maneuver performed by the quadcopter. It begins with a strong misalignment of the attitude and gradually reorients itself to align the direction of thrust with the direction of the desired force.

Figure 7.19 shows the evolution of the quadcopter's position during the maneuver. The results indicate that, due to the strong initial misalignment of the attitude, the quadcopter temporarily deviates from the reference position. However, once the desired attitude is achieved, the controller recovers the position error and guides it

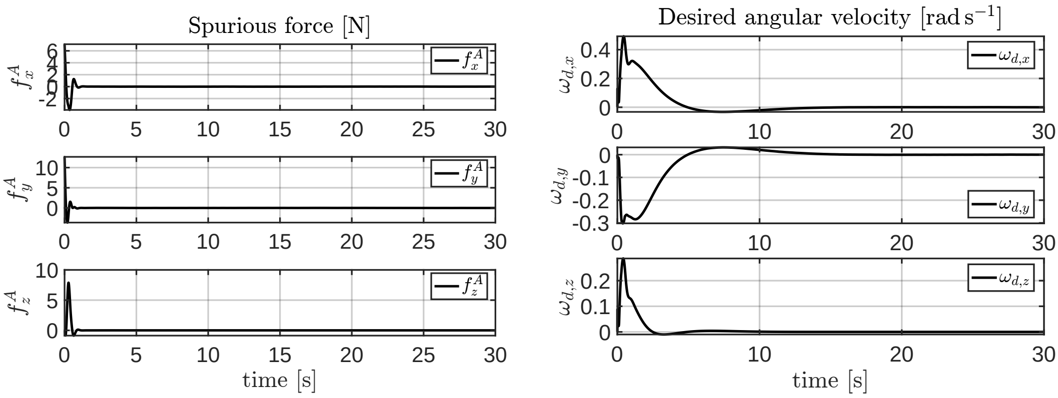

Figure 7.17. Evolution of spurious force and desired angular velocity during the complex manoeuvre. **(a)**: Spurious force $\boldsymbol{f}^A$, **(b)**: Desired angular velocity $\boldsymbol{\omega}_d$. Both quantities are effectively regulated to zero.

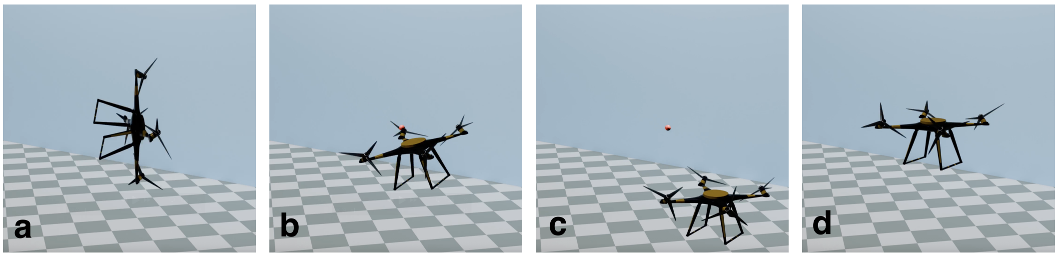

Figure 7.18. Sequence of screenshots from the 3D CAD model of the quadrotor during the reorienting manoeuvre, to be read from left to right: **(a)** The quadrotor starts with an unfavorable orientation at $\boldsymbol{p}_{\text{ref}}$ (the desired static hovering point); **(b)** The quadrotor, unable to counteract the initial orientation, leaves $\boldsymbol{p}_{\text{ref}}$; **(c)** The quadrotor has reoriented itself favorably and begins to recover the gap to $\boldsymbol{p}_{\text{ref}}$; **(d)** The quadrotor has reached $\boldsymbol{p}_{\text{ref}}$ and performs static hovering.

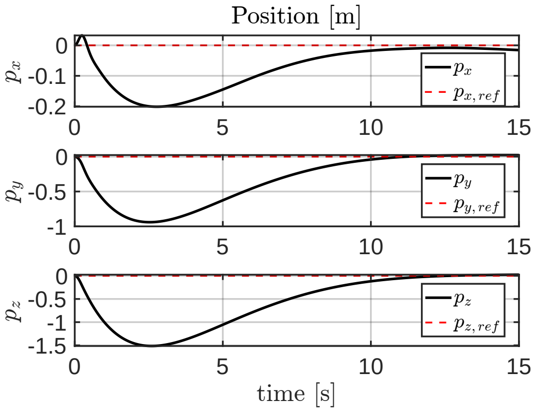

Figure 7.19. Position of the quadrotor during the reorienting manoeuvre. The position $\boldsymbol{p}$ converges to the reference $\boldsymbol{p}_r = \begin{bmatrix}0 & 0 & 0\end{bmatrix}^\top$.

to the reference point.

Figure 7.20 presents the velocity and angular velocity components. The angular

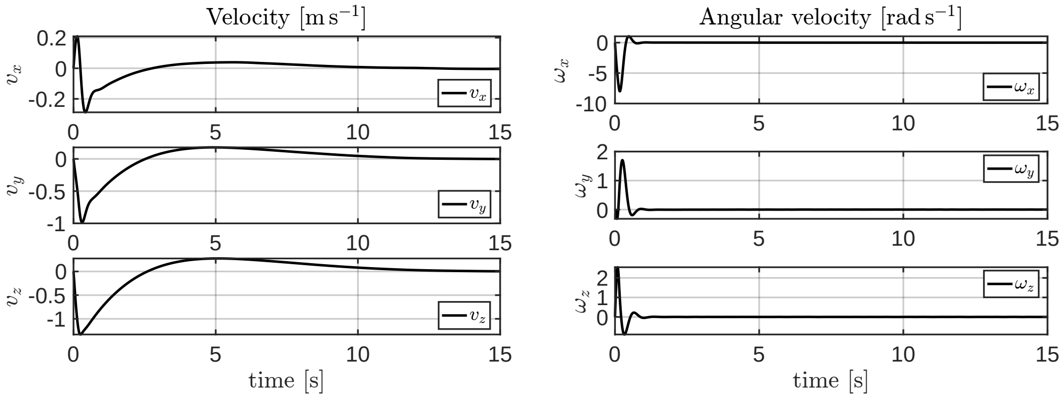

Figure 7.20. Time evolution of the quadrotor's linear and angular velocity components during the reorienting manoeuvre. **(a)**: Velocity components $\boldsymbol{v}$, **(b)**: Angular velocity components $\boldsymbol{\omega}$.

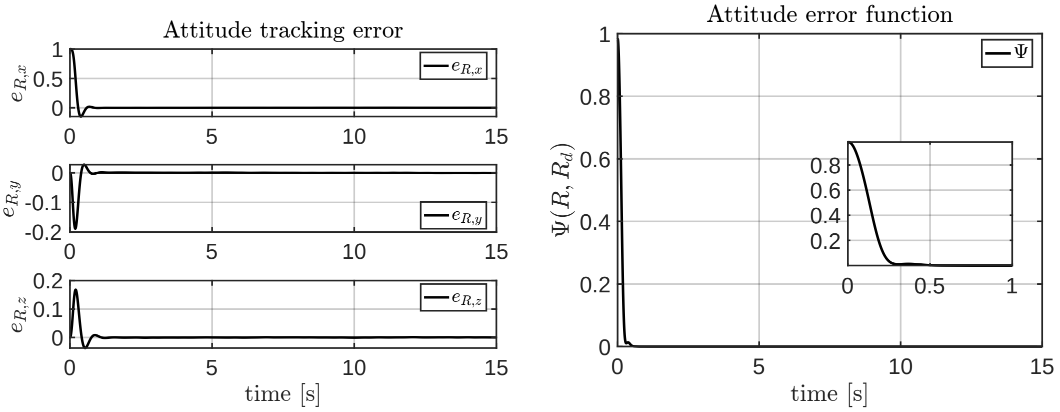

Figure 7.21. Time evolution of the quadrotor's attitude during the reorienting manoeuvre. **(a)**: Attitude tracking error components $\boldsymbol{e}_R$, **(b)**: Attitude error function $\Psi(\boldsymbol{R}, \boldsymbol{R}_d)$.

velocity, especially ω_x, exhibits significant oscillations during the reorientation phase, reflecting the large initial attitude error.

Figure 7.21 shows the evolution of the quadrotor's attitude. Both the attitude error components $\boldsymbol{e}_R$ and the attitude error function $\Psi(\boldsymbol{R}, \boldsymbol{R}_d)$ converge to zero, demonstrating that the quadrotor achieves the desired orientation. This manoeuvre is designed to drive the attitude error function close to its maximum permissible value, as defined by condition (6.7) in Proposition 6.1. The large initial attitude (89° about $\boldsymbol{x}_B$-axis) results in an initial attitude error function value of approximately 0.985.

Figure 7.22 displays the control inputs during the manoeuvre, namely, the spinning rates $\boldsymbol{u}$ for each rotor and the corresponding thrusts T_i. The control inputs remain within actuator saturation limits, except for rotors 2 and 3, which are initially switched off.

Figure 7.10 illustrates the evolution of the spurious force (panel **(a)**) and the desired angular velocity (panel **(b)**). Initially, the spurious force $\boldsymbol{f}^A$ is large due to the significant attitude error. As the manoeuvre progresses, both the spurious force

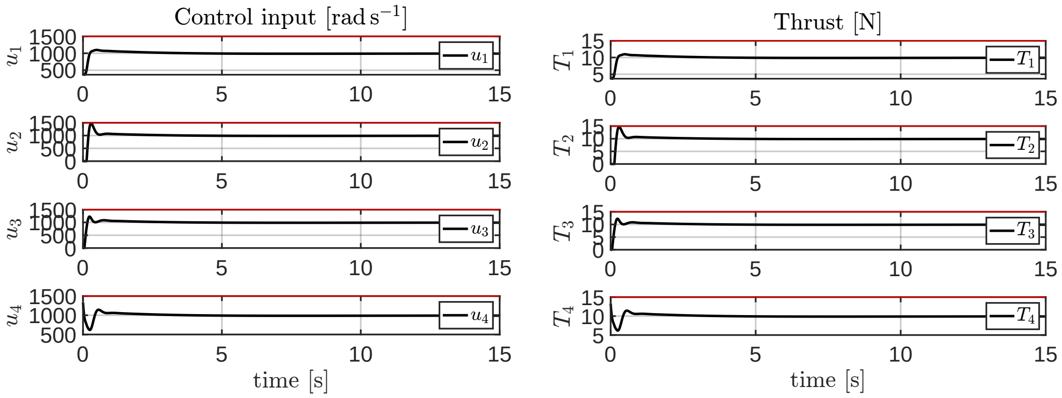

Figure 7.22. Time evolution of the control inputs during the reorienting manoeuvre. **(a)**: Spinning rates $\boldsymbol{u}$, **(b)**: Thrusts T_i generated by each rotor. The control inputs are well within the saturation limits, except for rotors 2 and 3, which are initially switched off.

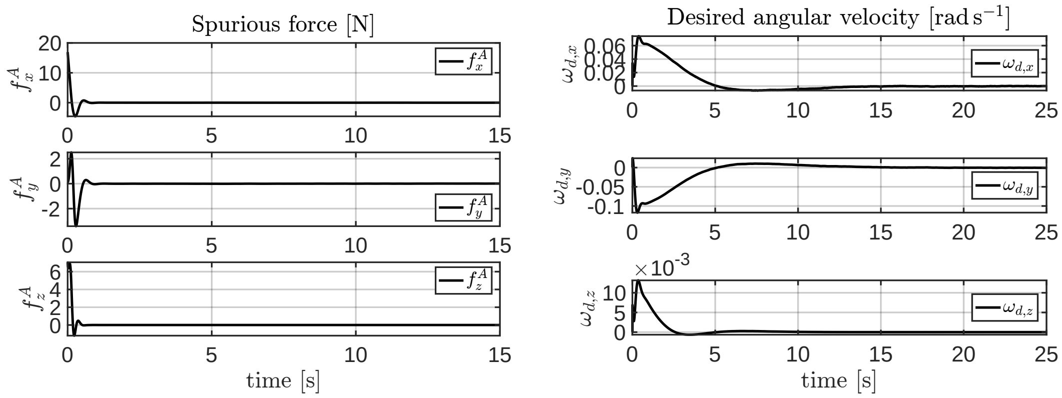

Figure 7.23. Spurious force and desired angular velocity evolution during the manoeuvre. **(a)**: Spurious force $\boldsymbol{f}^A$, **(b)**: Desired angular velocity $\boldsymbol{\omega}_d$. Both signals converge to zero, indicating the efficacy of the control law in mitigating spurious force effects even with large initial attitude misalignment.

and the desired angular velocity decrease and converge to zero, demonstrating the control law's ability to compensate for spurious force effects even under substantial initial misalignment.

During this reorientation maneuver, we saw how the quadcopter successfully aligns the direction of thrust with the desired direction of force, even in the presence of significant initial attitude misalignment. Proposition 6.1 guarantees the local exponential stability of the closed-loop system for attitudes that satisfy condition (6.7), and that it is respected throughout the maneuver. Although it is possible to reorient the quadcopter from a high initial attitude error, in such cases convergence is not guaranteed by proposition 6.1. The simulation results validate the stability properties of the control law and its ability to effectively handle reorientation maneuvers.

Chapter 8

Conclusion

8.1 Summary of Contributions

The ability to achieve static hovering is a fundamental requirement for multirotor aerial vehicles, as it ensures the capability to maintain a fixed position and orientation in space—an essential prerequisite for safe operation in cluttered or sensitive environments. This requirement becomes even more critical for fully-actuated generically tilted multirotors, which, following the failure of one or more rotors, may transition into a *partially coupled* configuration. When full actuation is lost, the craft's control authority drops so sharply that maintaining a steady hover can appear impossible; without that ability, the odds of an uncontrolled fall or collision rise steeply. It is therefore vital to understand—and be able to guarantee—static hovering under partial actuation, especially when a rotor fails, to keep these advanced aerial systems reliable and safe.

In this context, the geometric control law of Michieletto *et al.* in [26] offers a promising solution. This control law is designed to stabilize the platform in static hovering, even when it is partially coupled due to rotor failures. Although that control law had already been validated extensively in both simulation and real-world experiments—conducted in the Laboratory for Analysis and Architecture of Systems (LAAS-CNRS, Université de Toulouse, CNRS, Toulouse, France)—the task of providing a formal stability proof was explicitly left as future work. With this thesis, we have aimed to address this gap by offering a plausible and formal proof of local exponential stability, while acknowledging that further refinements and extensions may still be possible.

We began by identifying the mathematical model describing the dynamics of a generic GTM in a coordinate-free framework based on the Lie group SE(3). The model was then parameterized using three sets of parameters: (α_i, β_i) to generalize the tilt of the spinning axis of the i-th propeller, and λ_i to generalize the position of the i-th propeller on the x_B, y_B plane, thus allowing the possibility to place the propellers in configurations far more general and complex than simply positioning them at the vertices of a regular polygon [34, 27, 22, 42].

This coordinate-free formulation enabled the representation of the entire family of such platforms and allowed for a systematic study of their actuation capabilities through the analysis of the rank of the control input matrices $\boldsymbol{F}_1$ and $\boldsymbol{F}_2$. This made it possible to classify these platforms according to their actuation capabilities, in particular identifying which platforms are *partially coupled* [27].

Subsequently, we formally introduced the concept of *static hovering*, defined as the capability of a platform to maintain constant position and orientation in a stable manner. The conditions for a platform to be *static hoverable* were established in terms of its ability to generate arbitrary control moments and to independently modulate the thrust magnitude along a designated direction. Specifically, these conditions were derived by analyzing the kernel of the control moment input matrix $\boldsymbol{F}_2$ and the image of the control force input matrix $\boldsymbol{F}_1$, thereby providing a systematic criterion to determine whether a given GTM configuration admits static hovering [27, 26].

Then, by considering all the static hoverable platforms within the family of GTMs, we discussed and thoroughly analyzed the control law proposed in [26] that enables the platform to achieve static hovering. Since a formal stability proof was a missing piece in the existing literature, this work humbly attempts to address that gap. In particular, the proof was carried out based on the search for a candidate Lyapunov function that satisfies the conditions for exponential stability theorem. This was achieved by finding an expression for the desired angular velocity that depends linearly on the closed-loop tracking error dynamics.

Finally, we validated the theoretical results through numerical simulations in Matlab-Simulink, demonstrating the platform's ability to perform hovering, reorientation, and aggressive maneuvers, with simulation outcomes closely matching the predicted behavior.

8.2 Future Works

This study paves the way for several further investigations:

i. **Maximizing the region of admissible gains**: The stability analysis identifies a set of conditions ((6.8), (6.9), (6.10) and (6.11)) whose satisfaction ensures local exponential stability of the closed-loop system. These constraints define a region in the gain space, i.e., combinations of $(k_p, k_v, k_R, k_\omega)$ for which suitable c_1 and c_2 exist to guarantee stability. This region (denoted as $\mathcal{G}$), is almost certainly smaller than the true stability region, i.e., there may be additional gain combinations that also ensure stability but are excluded by the current, somewhat conservative, analysis. To address this, one could to revisit the proof with looser assumptions and push the range of allowable gains further out.

   One way forward is to replace the three separate positivity tests on $\boldsymbol{W}_1$, $\boldsymbol{W}_2$ and the extra bound in (6.11) with a single check. Form the block matrix

$$\boldsymbol{M} := \begin{bmatrix} \boldsymbol{W}_1 & -\frac{1}{2}\tilde{\boldsymbol{W}} \\ -\frac{1}{2}\tilde{\boldsymbol{W}}^\top & \boldsymbol{W}_2 \end{bmatrix}$$

   then apply the Schur-complement criterion and ask only that $\boldsymbol{M}$ be positive definite. Such improvements would enlarge the set of admissible gains, potentially enhancing both the performance and robustness of the control law.

ii. **Automatic tuning of c_1 and c_2**: After selecting the main gains so that they fall within the admissible region, it is still necessary to determine appropriate values for the parameters c_1 and c_2. These parameters must be chosen in such a way that the final stability condition (6.11) is satisfied. A sensible route is to pose the task as a constrained nonlinear optimisation, turning the leftover term in the stability inequality into the objective to be minimised and enforcing the limits in (6.8), (6.9) and (6.10) as hard constraints. Any set returned by the solver is therefore both legal and as close as possible to satisfying the stability requirement.

    A different route relies on data-driven search. By training a neural network to roam the (c_1, c_2) plane and flag every pair that clears the stability tests, one can sift through the admissible region much faster than with classical solvers. The advantage becomes clear when the space is wide or the link between the gains and the inequalities is strongly nonlinear, cases that often bog down traditional optimisation.

iii. **Exploiting actuation redundancy**: The control law could be further improved by leveraging the actuation redundancies offered by the platform. In particular, during the implementation of the reference control moment M_r, it is possible to use the kernel of the matrix F_1. In this context, it is possible to select the reference control moment entirely within $ker(F_1)$, thus ensuring the absence of spurious forces. However, this is not always feasible—such as in the case of tilted quadrotors or tilted pentarotors with a rank of $\boldsymbol{F}_1$ less than or equal to two—where the kernel may be trivial or insufficiently large.

    Additionally, the implementation of the reference control force $\boldsymbol{f}_r$ could be enhanced by fully utilizing the platform's translational actuation capabilities. For example, consider a platform that does not possess a single preferential direction, but rather a preferential plane (case $D2$, where $\dim(\mathfrak{F}_B) = 2$). In this situation, it is possible to select two vectors $\hat{\boldsymbol{b}}_1$ and $\hat{\boldsymbol{b}}_2$ in the kernel of $\boldsymbol{F}_2$ such that $\boldsymbol{F}_1\hat{\boldsymbol{b}}_i \neq 0$ for $i = 1, 2$. This would require determining two coefficients to implement the control force $\boldsymbol{u}_f$, thereby generalizing the approach from the one-dimensional case discussed in this thesis to a two-dimensional scenario. Extending all the steps and analyses presented here to accommodate such multidimensional cases would represent a significant and valuable generalization.

iv. **Applications to underwater and space vehicles**: The same control architecture could be adapted to autonomous underwater vehicles or microsatellites sharing the same actuation capabilities, where partial force–moment coupling also occurs.

In summary, this thesis has focused on the control law for partially coupled aerial platforms, providing a demonstration of its stability properties, an aspect not yet present in the scientific literature. In conclusion, concrete suggestions for further extensions and optimizations are provided.

Appendix

Appendix A

Properties of the Skew Map

The *skew map* $\boldsymbol{S} : \mathbb{R}^3 \to \mathfrak{so}(3)$ is a linear operator that associates a vector $\boldsymbol{v} = [v_1, v_2, v_3]^\top \in \mathbb{R}^3$ with a 3×3 skew-symmetric matrix as follows:

$$\boldsymbol{S}(\boldsymbol{v}) = \begin{bmatrix} 0 & -v_3 & v_2 \\ v_3 & 0 & -v_1 \\ -v_2 & v_1 & 0 \end{bmatrix}. \tag{A.1}$$

This mapping establishes an isomorphism between the vector space $\mathbb{R}^3$ and the Lie algebra $\mathfrak{so}(3)$, leveraging the properties of the vector cross product. Specifically, for any $\boldsymbol{w} \in \mathbb{R}^3$, the following holds:

$$\boldsymbol{S}(\boldsymbol{v})\boldsymbol{w} = \boldsymbol{v} \times \boldsymbol{w}.$$

The inverse mapping, denoted $\boldsymbol{S}^{-1} : \mathfrak{so}(3) \to \mathbb{R}^3$, retrieves the vector from its skew-symmetric matrix representation.

Key properties of the skew map include:

$$\boldsymbol{S}(\boldsymbol{v} + \boldsymbol{w}) = \boldsymbol{S}(\boldsymbol{v}) + \boldsymbol{S}(\boldsymbol{w}) \tag{A.2}$$

$$\boldsymbol{S}(\boldsymbol{v})\boldsymbol{w} = \boldsymbol{v} \times \boldsymbol{w} = -\boldsymbol{w} \times \boldsymbol{v} = -\boldsymbol{S}(\boldsymbol{w})\boldsymbol{v} \tag{A.3}$$

$$-\frac{1}{2}\operatorname{Tr}\left[\boldsymbol{S}(\boldsymbol{v})\boldsymbol{S}(\boldsymbol{w})\right] = \boldsymbol{v}^\top \boldsymbol{w} \tag{A.4}$$

$$\operatorname{Tr}\left[\boldsymbol{S}(\boldsymbol{v})\boldsymbol{A}\right] = \operatorname{Tr}\left[\boldsymbol{A}\boldsymbol{S}(\boldsymbol{v})\right] = \frac{1}{2}\operatorname{Tr}\left[\boldsymbol{S}(\boldsymbol{v})(\boldsymbol{A} - \boldsymbol{A}^\top)\right] = -\boldsymbol{v}^\top \boldsymbol{S}^{-1}(\boldsymbol{A} - \boldsymbol{A}^\top) \tag{A.5}$$

$$\boldsymbol{S}(\boldsymbol{v})\boldsymbol{A} + \boldsymbol{A}^\top \boldsymbol{S}(\boldsymbol{v}) = \boldsymbol{S}((\operatorname{Tr}[\boldsymbol{A}]\boldsymbol{I}_3 - \boldsymbol{A})\boldsymbol{v}) \tag{A.6}$$

$$\boldsymbol{R}\boldsymbol{S}(\boldsymbol{v})\boldsymbol{R}^\top = \boldsymbol{S}(\boldsymbol{R}\boldsymbol{v}) \tag{A.7}$$

$$\boldsymbol{S}(\boldsymbol{x})\boldsymbol{x} = \boldsymbol{0} \tag{A.8}$$

for all $\boldsymbol{v}, \boldsymbol{w} \in \mathbb{R}^3$, $\boldsymbol{A} \in \mathbb{R}^{3\times3}$, and $\boldsymbol{R} \in \mathbf{SO}(3)$.

For a comprehensive treatment of the skew map and its applications, refer to standard texts such as [23], [37], or [29].

Appendix B

Stability Theory

In this appendix, we provide a brief overview of the stability theory for nonlinear systems. These concepts are fundamental tools used to derive stability properties of the control laws proposed in this thesis. The interested reader should consult a standard text, such as [20] or [29]. Alternatively, the reader can refer to course materials about stability theory for nonlinear systems, such as [18, 17] or [30] for a more detailed treatment of the subject.

Consider a nonlinear system described by the ordinary differential equation (ODE)

$$\dot{\boldsymbol{x}} = \boldsymbol{f}(\boldsymbol{x}), \qquad \boldsymbol{x}(t_0) = \boldsymbol{x}_0, \tag{B.1}$$

in which $\boldsymbol{x} \in \mathbb{R}^n$ is the state of the system, $\boldsymbol{f} : \mathbb{R}^n \to \mathbb{R}^n$ is Lipschitz continuous w.r.t. $\boldsymbol{x}$.

The set of equilibria $\mathcal{E} \subset \mathbb{R}^n$ of the system is defined as the set of points where $\boldsymbol{f}(\boldsymbol{x}) = \boldsymbol{0}$. An equilibrium point $\boldsymbol{x}_e$ is considered locally stable if all solutions starting near $\boldsymbol{x}_e$ (within a neighborhood $\mathcal{I}_\delta(\boldsymbol{x}_e)$ of radius δ around $\boldsymbol{x}_e$) remain close to $\boldsymbol{x}_e$ for all time. On the other hand, an equilibrium point $\boldsymbol{x}_e$ is said to be locally asymptotically stable if it is locally stable and all solutions starting near $\boldsymbol{x}_e$ converge to $\boldsymbol{x}_e$ as $t \to \infty$. It is important to note that a nonlinear system can have finite or infinite equilibrium points, and their stability analysis needs to be performed separately for each of them.

Definition B.1 (Stability in the sense of Lyapunov)**.** *The equilibrium point $\boldsymbol{x}_e$ of* (B.1) *is said to be stable (in the sense of Lyapunov) at $t = t_0$ if, for every $\varepsilon > 0$, there exists a $\delta(\varepsilon) > 0$ such that for all $\boldsymbol{x}_0 \in \mathcal{I}_\delta(\boldsymbol{x}_e)$, the solution $\boldsymbol{x}(t)$ of the system satisfies*

$$\|\boldsymbol{x}(t) - \boldsymbol{x}_e\| < \varepsilon, \quad \forall t \geq t_0. \tag{B.2}$$

The concept of asymptotic stability can be formally defined as follows

Definition B.2 (Asymptotic Stability)**.** *An equilibrium point $\boldsymbol{x}_e$ of* (B.1) *is said to be asymptotically stable if it is stable and there exists a $\delta(\varepsilon) > 0$ such that for all $\boldsymbol{x}_0 \in \mathcal{I}_\delta(\boldsymbol{x}_e)$, the solution $\boldsymbol{x}(t)$ of the system satisfies*

$$\lim_{t \to \infty} \|\boldsymbol{x}(t) - \boldsymbol{x}_e\| = 0. \tag{B.3}$$

Finally, we say that an equilibrium point is *unstable* if it is not stable. Definitions B.1 and B.2 are *local* definitions; they describe the behavior of the system in a neighborhood of the equilibrium point. In general, if we want to study the global stability of the system, we need to consider the behavior of the system in the entire state space. We say that a system is globally asymptotically stable if it is asymptotically stable for all initial conditions in the state space. Notice that a necessary condition for an $\boldsymbol{x}_e$ to be globally asymptotically stable is that it is the only equilibrium point.

Moreover, the definition of asymptotic stability do not quantify the rate at which the solutions converge to the equilibrium point. There is a stronger notion of stability, called exponential stability, which requires that the solutions converge to the equilibrium point exponentially fast.

Definition B.3 (Exponential Stability and rate of convergence)**.** *An equilibrium point* $\boldsymbol{x}_e$ *of* (B.1) *is said to be exponentially stable if there exist constants* $M, \beta > 0$ *such that for all* $\boldsymbol{x}_0 \in \mathcal{I}_\delta(\boldsymbol{x}_e)$*, the solution* $\boldsymbol{x}(t)$ *of the system satisfies*

$$\|\boldsymbol{x}(t) - \boldsymbol{x}_e\| \leq M e^{-\beta(t-t_0)} \|\boldsymbol{x}_0 - \boldsymbol{x}_e\|, \quad \forall t \geq t_0. \tag{B.4}$$

The constant β *is called the rate of convergence of the system.*

Exponential stability is a strong form of stability; in particular, it implies asymptotic stability, but the converse is not true.

The stability, or asymptotic stability, properties of the equilibrium $\boldsymbol{x}_e$ of this system can be rigorously tested using the well-known criterion of Lyapunov. This criterion allows us to determine the stability of a system without explicitly integrating the differential equations (B.1). The Lyapunov's direct method is a powerful generalization of the idea that if there exists a "measure of energy" in a system, we can study the rate of change of the energy to ascertain stability. Furthermore, this method leverages the concept of comparison functions, which are precisely defined in the following definition.

Definition B.4 (Comparison Functions)**.** *A continuous function* $\alpha : [0, a) \to [0, +\infty)$ *is said to be in the class* $\mathcal{K}$ *if it is a continuous strictly increasing function and* $\alpha(0) = 0$*. Moreover, if* $a = +\infty$ *and* $\lim_{r \to +\infty} \alpha(r) = +\infty$*, then* α *is said to be in the class* $\mathcal{K}_\infty$*.*

To define exactly what one means by a "measure of energy" in a system, we introduce the concept of Lyapunov functions. Let $\mathcal{I}_\delta(\boldsymbol{x}_e)$ be an open ball of radius δ centered at $\boldsymbol{x}_e$ defined as

$$\mathcal{I}_\delta(\boldsymbol{x}_e) := \{\boldsymbol{x} \in \mathbb{R}^n : \|\boldsymbol{x} - \boldsymbol{x}_e\| < \delta\}$$

Definition B.5 (Positive Definite Function)**.** *Consider a scalar function* $V : \mathbb{R}^n \to \mathbb{R}$*, continuously differentiable w.r.t.* $\boldsymbol{x} \in \mathcal{I}_\delta(\boldsymbol{x}_e)$ *(i.e.,* $V \in C^1(\mathcal{I}_\delta)$*), and a class* $\mathcal{K}$ *function* $\alpha_1 : [0, a) \to [0, +\infty)$*. We say that* $V(\boldsymbol{x})$ *is locally positive definite if*

$$V(\boldsymbol{x}) \geq \alpha_1(\|\boldsymbol{x}\|), \quad \forall \boldsymbol{x} \in \mathcal{I}_\delta. \tag{B.5}$$

Moreover, if additionally $\alpha_1(\cdot)$ *is a class* $\mathcal{K}_\infty$ *function, then* $V(\boldsymbol{x})$ *is said to be positive definite.*

To bound the energy function from above, we define decrescence as follows

Definition B.6 (Decrescent Function). *Consider a scalar function* $V : \mathbb{R}^n \to \mathbb{R}$*, continuously differentiable w.r.t.* $\boldsymbol{x} \in \mathcal{I}_\delta(\boldsymbol{x}_e)$ *(i.e.,* $V \in C^1(\mathcal{I}_\delta)$*), and a class* $\mathcal{K}$ *function* $\alpha_2 : [0, a) \to [0, +\infty)$*. We say that* $V(\boldsymbol{x})$ *is decrescent if*

$$V(\boldsymbol{x}) \leq \alpha_2(\|\boldsymbol{x}\|), \quad \forall \boldsymbol{x} \in \mathcal{I}_\delta. \tag{B.6}$$

These definitions are crucial for the following theorem, which is the cornerstone of the Lyapunov stability theory. Roughly speaking, the theorem states that if there exists a Lyapunov function $V(\boldsymbol{x})$ that is locally positive definite and its time derivative along the trajectories of the system is a decrescent function, we can assert the stability of the equilibrium point $\boldsymbol{x}_e$. The time derivative of $V(\boldsymbol{x})$ along the trajectories of the system is defined as

$$\dot{V}(\boldsymbol{x}) = \frac{d}{dt} V(\boldsymbol{x}(t)) = \sum_{i=1}^{n} \frac{\partial V}{\partial x_i} \dot{x}_i = \frac{\partial V}{\partial x} \boldsymbol{f}(\boldsymbol{x}),$$

where $\frac{\partial V}{\partial x} = \left[\frac{\partial V}{\partial x_1}, \ldots, \frac{\partial V}{\partial x_n} \right]$ is the gradient of $V(\boldsymbol{x})$.

Theorem B.1 (Direct Method of Lyapunov). *Consider the system* (B.1) *and an equilibrium point* $\boldsymbol{x}_e$*. Let* $V : \mathcal{I}_\delta(\boldsymbol{x}_e) \to \mathbb{R}$ *be a continuously differentiable function such that, for some class* $\mathcal{K}$ *function* $\alpha_1(\cdot)$ *and* $\alpha_2(\cdot)$ *defined on* $[0, d)$*, with* $d > 0$*, satisfies*

$$\alpha_1(\|\boldsymbol{x}\|) \leq V(\boldsymbol{x}) \leq \alpha_2(\|\boldsymbol{x}\|), \quad \forall \boldsymbol{x} \in \mathcal{I}_\delta(\boldsymbol{x}_e). \tag{B.7}$$

If

$$\frac{\partial V}{\partial x} \boldsymbol{f}(\boldsymbol{x}) \leq 0, \quad \forall \boldsymbol{x} \in \mathcal{I}_\delta(\boldsymbol{x}_e), \tag{B.8}$$

then the equilibrium point $\boldsymbol{x}_e$ *is stable. If, for some class* $\mathcal{K}$ *function* $\alpha_3(\cdot)$*, defined on* $[0, d)$*, with* $d > 0$*, we have*

$$\frac{\partial V}{\partial x} \boldsymbol{f}(\boldsymbol{x}) \leq -\alpha_3(\|\boldsymbol{x}\|), \quad \forall \boldsymbol{x} \in \mathcal{I}_\delta(\boldsymbol{x}_e), \tag{B.9}$$

then the equilibrium point $\boldsymbol{x}_e$ *is locally asymptotically stable. Moreover, if the functions* $\alpha_1(\cdot)$*,* $\alpha_2(\cdot)$*, and* $\alpha_3(\cdot)$ *are class* $\mathcal{K}_\infty$ *function, then the equilibrium point* $\boldsymbol{x}_e$ *is globally asymptotically stable.*

Theorem B.1 provides sufficient conditions for the stability of the equilibrium point $\boldsymbol{x}_e$ of the system (B.1). However, it does not offer criteria for determining the existence of a Lyapunov function $V(\boldsymbol{x})$ that establishes the stability of the equilibrium point. The search for such a Lyapunov function could be arduous. However, it is a remarkable fact that the converse of Theorem B.1 holds: if an equilibrium point is stable, then there exists a Lyapunov function that satisfies the conditions of the theorem.

Moreover, Theorem B.1 also stops short of giving explicit rates of convergence of solutions to the equilibrium. If the equilibrium $\boldsymbol{x}_e$ of system (B.1) is globally asymptotically stable and, moreover, satisfies the condition (B.4) it is said that the equilibrium point $\boldsymbol{x}_e$ is globally asymptotically stable and also locally exponentially stable. In this context, the following criterion is useful to determine the exponential stability of the equilibrium point $\boldsymbol{x}_e$.

Theorem B.2 (Exponential Stability Theorem)**.** *Consider the system* (B.1) *and an equilibrium point* $\boldsymbol{x}_e$*. It is globally asymptotically stable and locally exponentially stable if and only if there exists a continuously differentiable function* $V : \mathcal{I}_\delta(\boldsymbol{x}_e) \to \mathbb{R}$*, with* $\delta > 0$*, three class* $\mathcal{K}_\infty$ *functions* $\alpha_1(\cdot)$*,* $\alpha_2(\cdot)$*, and* $\alpha_3(\cdot)$ *defined on* $[0, d)$*, with* $d > 0$*, and two real numbers* $a_1, a_3 > 0$ *such that*

$$\alpha_1(\|\boldsymbol{x}\|) \leq V(\boldsymbol{x}) \leq \alpha_2(\|\boldsymbol{x}\|), \quad \forall \boldsymbol{x} \in \mathcal{I}_\delta(\boldsymbol{x}_e), \tag{B.10}$$

$$\frac{\partial V}{\partial x}\boldsymbol{f}(\boldsymbol{x}) \leq -\alpha_3(\|\boldsymbol{x}\|), \quad \forall \boldsymbol{x} \in \mathcal{I}_\delta(\boldsymbol{x}_e), \tag{B.11}$$

and

$$\alpha_1(\|\boldsymbol{x}\|) = a_1\|\boldsymbol{x}\|^2, \quad \alpha_3(\|\boldsymbol{x}\|) = a_3\|\boldsymbol{x}\|^2, \quad \forall \boldsymbol{x} \in \mathcal{I}_\delta(\boldsymbol{x}_e). \tag{B.12}$$

Another important concept exploited during the stability analysis of nonlinear controller is the concept of *exponential attractiveness* here defined.

Definition B.7 (Exponential Attractiveness)**.** *Consider the system* (B.1) *and an equilibrium point* $\boldsymbol{x}_e$*. It is said to be exponentially attractive if there exist constants* $\delta, M, \beta > 0$ *such that for all* $\boldsymbol{x}_0 \in \mathcal{I}_\delta(\boldsymbol{x}_e)$*, the solution* $\boldsymbol{x}(t)$ *of the system satisfies*

$$\|\boldsymbol{x}(t) - \boldsymbol{x}_e\| \leq M e^{-\beta(t-t_0)}, \quad \forall t \geq t_0. \tag{B.13}$$

It is important to notice that the concept of exponential attractiveness is weaker than the concept of exponential stability, in which the above inequality is replaced by $\|\boldsymbol{x}(t) - \boldsymbol{x}_e\| \leq M e^{-\beta(t-t_0)}\|\boldsymbol{x}_0 - \boldsymbol{x}_e\|$.

Appendix C

Attitude Tracking Errors

In this appendix, we present several results of the attitude tracking errors, which are essential for the stability analysis of the hierarchical control law presented in Section 5.3. In particular, we derive the time derivative of the attitude error function $\Psi(\boldsymbol{R}, \boldsymbol{R}_d)$, as defined in (5.8), and the time derivative of the attitude tracking error vector $\boldsymbol{e}_R$ from (5.9). These results are crucial for understanding the dynamics of the attitude tracking errors and their implications for stability. Finally, we show how the attitude error function $\Psi(\boldsymbol{R}, \boldsymbol{R}_d)$ is related to the attitude tracking error vector $\boldsymbol{e}_R$ and how to derive the angular velocity tracking error vector $\boldsymbol{e}_\omega$. The computations presented in this appendix are based on the work of Lee et al. [22] and are adapted to our specific context.

C.1 Time Derivative of the Attitude Error Function

Recall the attitude kinematics from (2.2). The time derivative of the attitude error function is computed as follows:

$$\begin{aligned}
\dot{\Psi}(\boldsymbol{R}, \boldsymbol{R}_d) &= \frac{1}{2}\mathrm{Tr}\left[-\dot{\boldsymbol{R}}_d^\top \boldsymbol{R} - \boldsymbol{R}_d^\top \dot{\boldsymbol{R}}\right] \\
&= -\frac{1}{2}\mathrm{Tr}\left[-\boldsymbol{S}(\boldsymbol{\omega}_d)\boldsymbol{R}_d^\top \boldsymbol{R} + \boldsymbol{R}_d^\top \boldsymbol{R}\boldsymbol{S}(\boldsymbol{\omega})\right] \\
&= -\frac{1}{2}\mathrm{Tr}\left[\boldsymbol{R}_d^\top \boldsymbol{R}\left(-\boldsymbol{R}^\top \boldsymbol{R}_d \boldsymbol{S}(\boldsymbol{\omega}_d)\boldsymbol{R}_d^\top \boldsymbol{R} + \boldsymbol{S}(\boldsymbol{\omega})\right)\right].
\end{aligned}$$

By applying properties (A.2) and (A.7) of the skew-symmetric operator, this expression simplifies to

$$\begin{aligned}
\dot{\Psi}(\boldsymbol{R}, \boldsymbol{R}_d) &= -\frac{1}{2}\mathrm{Tr}\left[\boldsymbol{R}_d^\top \boldsymbol{R}\boldsymbol{S}(\boldsymbol{\omega} - \boldsymbol{R}^\top \boldsymbol{R}_d \boldsymbol{\omega}_d)\right] \\
&= -\frac{1}{2}\mathrm{Tr}\left[\boldsymbol{R}_d^\top \boldsymbol{R}\boldsymbol{S}(\boldsymbol{e}_\omega)\right] \\
&= \frac{1}{2}\boldsymbol{e}_\omega^\top \boldsymbol{S}^{-1}\left(\boldsymbol{R}_d^\top \boldsymbol{R} - \boldsymbol{R}^\top \boldsymbol{R}_d\right) \\
&= \boldsymbol{e}_\omega^\top \boldsymbol{e}_R,
\end{aligned}$$

where we have used the definitions of the attitude tracking errors $\boldsymbol{e}_R$ and $\boldsymbol{e}_\omega$ from (5.9) and (C.7), as well as property (A.5) of the skew-symmetric map.

In summary, the time derivative of the attitude error function is given by

$$\dot{\Psi}(\boldsymbol{R}, \boldsymbol{R}_d) = \langle \boldsymbol{e}_\omega, \boldsymbol{e}_R \rangle. \tag{C.1}$$

C.2 Time Derivative of the Attitude Tracking Error

Next, we derive the time derivative of the attitude tracking error vector $\boldsymbol{e}_R$ as defined in (5.9). Using the identity $\frac{d}{dt}(\boldsymbol{R}_d^\top \boldsymbol{R}) = \boldsymbol{R}_d^\top \boldsymbol{R}\boldsymbol{S}(\boldsymbol{e}_\omega)$, we obtain

$$\begin{aligned}
\dot{\boldsymbol{e}}_R &= \frac{1}{2}\frac{d}{dt}\boldsymbol{S}^{-1}\left(\boldsymbol{R}_d^\top \boldsymbol{R} - \boldsymbol{R}^\top \boldsymbol{R}_d\right) \\
&= \frac{1}{2}\boldsymbol{S}^{-1}\left(\frac{d}{dt}(\boldsymbol{R}_d^\top \boldsymbol{R}) - \left(\frac{d}{dt}(\boldsymbol{R}_d^\top \boldsymbol{R})\right)^\top\right) \\
&= \frac{1}{2}\boldsymbol{S}^{-1}\left(\boldsymbol{R}_d^\top \boldsymbol{R}\boldsymbol{S}(\boldsymbol{e}_\omega) + \boldsymbol{S}(\boldsymbol{e}_\omega)\boldsymbol{R}^\top \boldsymbol{R}_d\right).
\end{aligned}$$

Applying property (A.6) of the skew-symmetric operator, we further simplify

$$\begin{aligned}
\dot{\boldsymbol{e}}_R &= \frac{1}{2}\boldsymbol{S}^{-1}\left(\boldsymbol{S}\left((\mathrm{Tr}[\boldsymbol{R}^\top \boldsymbol{R}_d]\boldsymbol{I} - \boldsymbol{R}^\top \boldsymbol{R}_d)\boldsymbol{e}_\omega\right)\right) \\
&= \frac{1}{2}\left(\mathrm{Tr}[\boldsymbol{R}^\top \boldsymbol{R}_d]\boldsymbol{I} - \boldsymbol{R}^\top \boldsymbol{R}_d\right)\boldsymbol{e}_\omega.
\end{aligned}$$

Defining the matrix

$$\boldsymbol{C}(\boldsymbol{R}_d^\top \boldsymbol{R}) \coloneqq \frac{1}{2}\left(\mathrm{Tr}[\boldsymbol{R}^\top \boldsymbol{R}_d]\boldsymbol{I} - \boldsymbol{R}^\top \boldsymbol{R}_d\right), \tag{C.2}$$

we conclude that

$$\dot{\boldsymbol{e}}_R = \boldsymbol{C}(\boldsymbol{R}_d^\top \boldsymbol{R})\boldsymbol{e}_\omega. \tag{C.3}$$

We now show that the Euclidean norm of this matrix is less than or equal to one, i.e., $\|\boldsymbol{C}(\boldsymbol{R}_d^\top \boldsymbol{R})\|_2 \leq 1$ for any $\boldsymbol{R}_d^\top \boldsymbol{R} \in \mathbf{SO}(3)$. This property is crucial for the stability analysis, as it ensures that the attitude tracking error grows at most linearly with respect to the angular velocity error $\boldsymbol{e}_\omega$.

To establish this bound, we analyze the spectral properties of $\boldsymbol{C}^\top \boldsymbol{C}$. Specifically, we seek its maximum eigenvalue. For this purpose, it is convenient to represent the matrix $\boldsymbol{C}(\boldsymbol{R}_d^\top \boldsymbol{R})$ using the Rodrigues formula

$$\boldsymbol{C}(e^{\boldsymbol{S}(\boldsymbol{x})}) = \frac{1}{2}(\mathrm{Tr}[(e^{\boldsymbol{S}(\boldsymbol{x})})^\top]\boldsymbol{I}_3 - (e^{\boldsymbol{S}(\boldsymbol{x})})^\top),$$

where $\boldsymbol{x} \in \mathbb{R}^3$ is such that $\boldsymbol{R}_d^\top \boldsymbol{R} = e^{\boldsymbol{S}^\top(\boldsymbol{x})}$. The matrix $\boldsymbol{C}(e^{\boldsymbol{S}(\boldsymbol{x})})$ can be further analyzed using the Rodrigues rotation formula

$$e^{\boldsymbol{S}(\boldsymbol{x})} = \hat{\boldsymbol{x}}\hat{\boldsymbol{x}}^\top + \left(\boldsymbol{I}_3 - \hat{\boldsymbol{x}}\hat{\boldsymbol{x}}^\top\right)\cos(\|\boldsymbol{x}\|) + \boldsymbol{S}(\hat{\boldsymbol{x}})\sin(\|\boldsymbol{x}\|),$$

where $\hat{\boldsymbol{x}} = \boldsymbol{x}/\|\boldsymbol{x}\|$ for $\boldsymbol{x} \neq \boldsymbol{0}$. Noting that the trace of a rotation matrix is $1 + 2\cos(\|\boldsymbol{x}\|)$, we obtain

$$\boldsymbol{C}(e^{\boldsymbol{S}(\boldsymbol{x})}) = \frac{1}{2}(2\cos(\|\boldsymbol{x}\|)\boldsymbol{I}_3 + \sin(\|\boldsymbol{x}\|)\boldsymbol{S}(\hat{\boldsymbol{x}}) - (1 - \cos(\|\boldsymbol{x}\|))\boldsymbol{S}^2(\hat{\boldsymbol{x}})).$$

Therefore, the matrix $\boldsymbol{C}^\top(\boldsymbol{R}_d^\top \boldsymbol{R})\boldsymbol{C}(\boldsymbol{R}_d^\top \boldsymbol{R})$ can be expressed as

$$\boldsymbol{C}^\top(\boldsymbol{R}_d^\top \boldsymbol{R})\boldsymbol{C}(\boldsymbol{R}_d^\top \boldsymbol{R}) = \cos^2(\|\boldsymbol{x}\|)\boldsymbol{I}_3 - (\frac{1}{2} + \frac{1}{2}\cos(\|\boldsymbol{x}\|) - \cos^2(\|\boldsymbol{x}\|))\boldsymbol{S}^2(\hat{\boldsymbol{x}}).$$

The eigenvalues of this matrix are given by

$$\lambda_1 = \cos^2(\|\boldsymbol{x}\|), \quad \lambda_{2,3} = \frac{1}{2} + \frac{1}{2}\cos(\|\boldsymbol{x}\|).$$

In conclusion, we derive the bound for the Euclidean norm of the matrix $\boldsymbol{C}(\boldsymbol{R}_d^\top \boldsymbol{R})$ as follows

$$\|\boldsymbol{C}(\boldsymbol{R}_d^\top \boldsymbol{R})\|_2 = \sqrt{\lambda_{\max}(\boldsymbol{C}^\top(\boldsymbol{R}_d^\top \boldsymbol{R})\boldsymbol{C}(\boldsymbol{R}_d^\top \boldsymbol{R}))} \leq 1, \quad \forall \boldsymbol{R}_d^\top \boldsymbol{R} \in \mathbf{SO}(3). \tag{C.4}$$

C.3 Relation Between the Attitude Error Function and the Attitude Tracking Error

Finally, we show that the attitude error function $\Psi(\boldsymbol{R}, \boldsymbol{R}_d)$ is related to the attitude tracking error vector $\boldsymbol{e}_R$. In particular, starting from the definition of the attitude error function in (5.8), and writing $\boldsymbol{R}_d^\top \boldsymbol{R} = e^{\boldsymbol{S}(\boldsymbol{x})}$, for $\boldsymbol{x} \in \mathbb{R}^3$, we get

$$\Psi(\boldsymbol{R}, \boldsymbol{R}_d) = \frac{1}{2}(3 - 1 - 2\cos(\|\boldsymbol{x}\|)) = 1 - \cos(\|\boldsymbol{x}\|). \tag{C.5}$$

Using the latter expression, we have derived the following relation

$$0 \leq \Psi(\boldsymbol{R}, \boldsymbol{R}_d) = 1 - \cos(\|\boldsymbol{x}\|) \leq 2, \quad \forall \boldsymbol{R}_d^\top \boldsymbol{R} \in \mathbf{SO}(3).$$

Let us now relate the attitude error function $\Psi(\boldsymbol{R}, \boldsymbol{R}_d)$ to the attitude tracking error vector $\boldsymbol{e}_R$. To this end, we compute the square of the Euclidean norm of the attitude tracking error vector $\boldsymbol{e}_R$ as follows

$$\|\boldsymbol{e}_R\|^2 = \frac{1}{4}\boldsymbol{S}^{-\top}(\boldsymbol{R}_d^\top \boldsymbol{R} - \boldsymbol{R}^\top \boldsymbol{R}_d)\boldsymbol{S}^{-1}(\boldsymbol{R}_d^\top \boldsymbol{R} - \boldsymbol{R}^\top \boldsymbol{R}_d).$$

Writing the rotation matrix $\boldsymbol{R}_d^\top \boldsymbol{R}$ as $e^{\boldsymbol{S}(\boldsymbol{x})}$, we get

$$\boldsymbol{R}_d^\top \boldsymbol{R} - \boldsymbol{R}^\top \boldsymbol{R}_d = e^{\boldsymbol{S}(\boldsymbol{x})} - \left(e^{\boldsymbol{S}(\boldsymbol{x})}\right)^\top = 2\sin(\|\boldsymbol{x}\|)\boldsymbol{S}(\hat{\boldsymbol{x}}).$$

Thus, we can express the square of the Euclidean norm of the attitude tracking error vector as

$$\|\boldsymbol{e}_R\|^2 = \frac{1}{4}4\sin^2(\|\boldsymbol{x}\|) = \sin^2(\|\boldsymbol{x}\|).$$

Using the relation in (C.5), we can express $\|\boldsymbol{e}_R\|^2$ in terms of the attitude error function as follows

$$\begin{aligned}\|\boldsymbol{e}_R\|^2 &= \sin^2(\|\boldsymbol{x}\|) = 1 - \cos^2(\|\boldsymbol{x}\|) = (1 + \cos(\|\boldsymbol{x}\|))(1 - \cos(\|\boldsymbol{x}\|)) \\ &= (1 + \cos(\|\boldsymbol{x}\|))\Psi(\boldsymbol{R}, \boldsymbol{R}_d) = (2 - \Psi(\boldsymbol{R}, \boldsymbol{R}_d))\Psi(\boldsymbol{R}, \boldsymbol{R}_d).\end{aligned} \tag{C.6}$$

C.4 Angular Velocity Tracking Error

For completeness, we also derive the expression for the angular velocity tracking error $\boldsymbol{e}_\omega$ as defined in (C.7).

It is essential to account for the difference between the desired angular velocity and the actual angular velocity. This difference is captured by the angular velocity tracking error $\boldsymbol{e}_\omega$. To define this error, we have to compare $\dot{\boldsymbol{R}} \in \mathbf{T}_{\boldsymbol{R}}\mathbf{SO}(3)$ with $\dot{\boldsymbol{R}}_d \in \mathbf{T}_{\boldsymbol{R}_d}\mathbf{SO}(3)$. Since they belong to different tangent spaces, we cannot directly compare them. However, we can map $(\boldsymbol{R}_d, \dot{\boldsymbol{R}}_d) \in \mathbf{SO}(3) \times \mathbf{T}_{\boldsymbol{R}_d}\mathbf{SO}(3)$ to the tangent boundle $\mathbf{SO}(3) \times \mathbf{T}_{\boldsymbol{R}}\mathbf{SO}(3)$ by the right-translation map $\mathcal{R}_{\boldsymbol{R}_d^\top \boldsymbol{R}} : \mathbf{SO}(3) \times \mathbf{T}_{\boldsymbol{R}_d}\mathbf{SO}(3) \to \mathbf{SO}(3) \times \mathbf{T}_{\boldsymbol{R}}\mathbf{SO}(3)$, which is defined as

$$(\boldsymbol{R}_d, \dot{\boldsymbol{R}}_d) \xrightarrow{\mathcal{R}_{\boldsymbol{R}_d^\top \boldsymbol{R}}} (\boldsymbol{R}, \dot{\boldsymbol{R}}).$$

Once $\dot{\boldsymbol{R}}_d$ is transformed into a vector in $\mathbf{T}_{\boldsymbol{R}}\mathbf{SO}(3)$, we can compare it with $\dot{\boldsymbol{R}}$ as follows

$$\begin{aligned}
\dot{\boldsymbol{R}} - \dot{\boldsymbol{R}}_d(\boldsymbol{R}_d^\top \boldsymbol{R}) &= \boldsymbol{R}\boldsymbol{S}(\boldsymbol{\omega}) - \boldsymbol{R}_d\boldsymbol{S}(\boldsymbol{\omega}_d)\boldsymbol{R}_d^\top \boldsymbol{R} \\
&= \boldsymbol{R}(\boldsymbol{S}(\boldsymbol{\omega}) - \boldsymbol{R}^\top \boldsymbol{R}_d\boldsymbol{S}(\boldsymbol{\omega}_d)\boldsymbol{R}_d^\top \boldsymbol{R}) \\
&= \boldsymbol{R}\boldsymbol{S}(\boldsymbol{e}_\omega),
\end{aligned}$$

where in the last equality we have exploited two properties of the $\boldsymbol{S}(\cdot)$ map[1]. The quantity $\boldsymbol{e}_\omega$ is the angular velocity tracking error and it is defined as

$$\boldsymbol{e}_\omega = \boldsymbol{\omega} - \boldsymbol{R}^\top \boldsymbol{R}_d \boldsymbol{\omega}_d. \tag{C.7}$$

We can show that the angular velocity tracking error $\boldsymbol{e}_\omega$ is the angular velocity related to the rotation matrix $\boldsymbol{R}_d^\top \boldsymbol{R}$, represented in the body-fixed reference frame, since

$$\begin{gathered}
\frac{d}{dt}(\boldsymbol{R}_d^\top \boldsymbol{R}) = \dot{\boldsymbol{R}}_d^\top \boldsymbol{R} + \boldsymbol{R}_d^\top \dot{\boldsymbol{R}} = (\boldsymbol{R}_d S(\boldsymbol{\omega}_d))^\top \boldsymbol{R} + \boldsymbol{R}_d^\top \boldsymbol{R} S(\boldsymbol{\omega}) = \\
\boldsymbol{R}_d^\top \boldsymbol{R} S(\boldsymbol{\omega}) - S(\boldsymbol{\omega}_d)\boldsymbol{R}_d^\top \boldsymbol{R} = \boldsymbol{R}_d^\top \boldsymbol{R} S(\boldsymbol{e}_\omega).
\end{gathered}$$

---

[1] Properties (A.2) and (A.8). For more details see Appendix A

Appendix D

Desired Angular Velocity

In this appendix, we derive an explicit expression for the desired angular velocity $\boldsymbol{\omega}_d$ as a function of the tracking errors: attitude error $\boldsymbol{e}_R$, angular velocity error $\boldsymbol{e}_\omega$, position error $\boldsymbol{e}_p$, and velocity $\boldsymbol{v}$.

The desired angular velocity $\boldsymbol{\omega}_d$ arises from the time variation of the reference rotation matrix $\boldsymbol{R}_d$, defined in (5.6). Differentiating $\boldsymbol{R}_d$ with respect to time yields a skew-symmetric matrix, from which $\boldsymbol{\omega}_d$ can be extracted:

$$\dot{\boldsymbol{R}}_d = \boldsymbol{R}_d \boldsymbol{S}(\boldsymbol{\omega}_d) \quad \Longrightarrow \quad \boldsymbol{\omega}_d = \boldsymbol{S}^{-1}(\boldsymbol{R}_d^\top \dot{\boldsymbol{R}}_d).$$

Assuming $\boldsymbol{R}_b$ is constant, the time derivative of $\boldsymbol{R}_d = \boldsymbol{R}_w \boldsymbol{R}_b$ simplifies to

$$\dot{\boldsymbol{R}}_d = \dot{\boldsymbol{R}}_w \boldsymbol{R}_b.$$

Substituting into the previous expression gives

$$\boldsymbol{\omega}_d = \boldsymbol{S}^{-1}(\boldsymbol{R}_b^\top \boldsymbol{R}_w^\top \dot{\boldsymbol{R}}_w \boldsymbol{R}_b). \tag{D.1}$$

Let $\boldsymbol{\omega}_w$ denote the angular velocity associated with $\boldsymbol{R}_w$, expressed in the inertial frame $\mathcal{F}_W$. By definition,

$$\dot{\boldsymbol{R}}_w = \boldsymbol{S}(\boldsymbol{\omega}_w) \boldsymbol{R}_w. \tag{D.2}$$

Substituting (D.2) into (D.1) yields

$$\boldsymbol{\omega}_d = \boldsymbol{S}^{-1}(\boldsymbol{R}_b^\top \boldsymbol{R}_w^\top \boldsymbol{S}(\boldsymbol{\omega}_w) \boldsymbol{R}_w \boldsymbol{R}_b) = \boldsymbol{S}^{-1}(\boldsymbol{R}_d^\top \boldsymbol{S}(\boldsymbol{\omega}_w) \boldsymbol{R}_d) = \boldsymbol{R}_d^\top \boldsymbol{\omega}_w,$$

where the last equality uses the identity $\boldsymbol{S}^{-1}(\boldsymbol{R}^\top \boldsymbol{S}(\boldsymbol{x}) \boldsymbol{R}) = \boldsymbol{R}^\top \boldsymbol{x}$ for any rotation matrix $\boldsymbol{R}$ and vector $\boldsymbol{x}$.

To compute $\boldsymbol{\omega}_d$, we need an explicit expression for $\boldsymbol{\omega}_w$ in terms of the columns of $\boldsymbol{R}_w$ and their derivatives. Let

$$\boldsymbol{R}_w = \begin{bmatrix} \boldsymbol{w}_1 & \boldsymbol{w}_2 & \boldsymbol{w}_3 \end{bmatrix},$$

where $\boldsymbol{w}_3 = \hat{\boldsymbol{f}}_r$ is the unit vector along the desired control force, and $\boldsymbol{w}_1$, $\boldsymbol{w}_2$ complete the orthonormal frame with a given unit vector $\hat{\boldsymbol{r}}_1$. Specifically,

$$\boldsymbol{w}_2 = \frac{\boldsymbol{w}_3 \times \hat{\boldsymbol{r}}_1}{\|\boldsymbol{w}_3 \times \hat{\boldsymbol{r}}_1\|}, \quad \boldsymbol{w}_1 = \boldsymbol{w}_2 \times \boldsymbol{w}_3.$$

The time derivative of $\boldsymbol{R}_w$ is

$$\dot{\boldsymbol{R}}_w = \begin{bmatrix} \dot{\boldsymbol{w}}_1 & \dot{\boldsymbol{w}}_2 & \dot{\boldsymbol{w}}_3 \end{bmatrix},$$

with

$$\begin{aligned}
\dot{\boldsymbol{w}}_3 &= \dot{\hat{\boldsymbol{f}}}_r, \\
\dot{\boldsymbol{w}}_2 &= \frac{1}{\|\boldsymbol{w}_3 \times \hat{\boldsymbol{r}}_1\|} \left[\boldsymbol{I}_3 - \boldsymbol{w}_2 \boldsymbol{w}_2^\top \right] (\dot{\boldsymbol{w}}_3 \times \hat{\boldsymbol{r}}_1), \\
\dot{\boldsymbol{w}}_1 &= \dot{\boldsymbol{w}}_2 \times \boldsymbol{w}_3 + \boldsymbol{w}_2 \times \dot{\boldsymbol{w}}_3,
\end{aligned}$$

assuming $\hat{\boldsymbol{r}}_1$ is constant. Here, we have used the time derivative of a unit vector $\hat{\boldsymbol{k}}$:

$$\dot{\hat{\boldsymbol{k}}} = \frac{1}{\|\boldsymbol{k}\|} \left[\boldsymbol{I}_3 - \hat{\boldsymbol{k}} \hat{\boldsymbol{k}}^\top \right] \dot{\boldsymbol{k}}.$$

Each unit vector $\boldsymbol{w}_i$ in $\boldsymbol{R}_w$ satisfies

$$\dot{\boldsymbol{w}}_i = \boldsymbol{\omega}_w \times \boldsymbol{w}_i, \quad i = 1, 2, 3. \tag{D.3}$$

For $i = 3$,

$$\dot{\boldsymbol{w}}_3 = \boldsymbol{\omega}_w \times \boldsymbol{w}_3.$$

Premultiplying by $\boldsymbol{w}_3 \times$ and applying the vector triple product identity,

$$\boldsymbol{w}_3 \times \dot{\boldsymbol{w}}_3 = \boldsymbol{\omega}_w - (\boldsymbol{w}_3^\top \boldsymbol{\omega}_w) \boldsymbol{w}_3.$$

Thus, $\boldsymbol{\omega}_w$ decomposes as

$$\boldsymbol{\omega}_w = \underbrace{\boldsymbol{w}_3 \times \dot{\boldsymbol{w}}_3}_{\boldsymbol{\omega}_{w_\perp}} + \underbrace{(\boldsymbol{w}_3^\top \boldsymbol{\omega}_w) \boldsymbol{w}_3}_{\boldsymbol{\omega}_{w_\|}}, \tag{D.4}$$

where $\boldsymbol{\omega}_{w_\perp}$ is the component orthogonal to $\boldsymbol{w}_3$, and $\boldsymbol{\omega}_{w_\|}$ is the component parallel to $\boldsymbol{w}_3$.

The orthogonal component $\boldsymbol{\omega}_{w_\perp} = \boldsymbol{w}_3 \times \dot{\boldsymbol{w}}_3$ is directly computable. The parallel component requires further development. Since $\boldsymbol{w}_3 = \boldsymbol{w}_1 \times \boldsymbol{w}_2$,

$$\boldsymbol{w}_3^\top \boldsymbol{\omega}_w = (\boldsymbol{w}_1 \times \boldsymbol{w}_2)^\top \boldsymbol{\omega}_w = \boldsymbol{w}_2^\top (\boldsymbol{\omega}_w \times \boldsymbol{w}_1) = \boldsymbol{w}_2^\top \dot{\boldsymbol{w}}_1.$$

Expanding $\dot{\boldsymbol{w}}_1$ and simplifying using orthogonality,

$$\begin{aligned}
\boldsymbol{w}_2^\top \dot{\boldsymbol{w}}_1 &= \boldsymbol{w}_2^\top (\dot{\boldsymbol{w}}_2 \times \boldsymbol{w}_3) \\
&= \frac{1}{\|\boldsymbol{w}_3 \times \hat{\boldsymbol{r}}_1\|} \boldsymbol{w}_2^\top \left((\boldsymbol{I}_3 - \boldsymbol{w}_2 \boldsymbol{w}_2^\top)(\dot{\boldsymbol{w}}_3 \times \hat{\boldsymbol{r}}_1) \right) \times \boldsymbol{w}_3 \\
&= \frac{1}{\|\boldsymbol{w}_3 \times \hat{\boldsymbol{r}}_1\|} \left(\boldsymbol{w}_2^\top (\dot{\boldsymbol{w}}_3 \times \hat{\boldsymbol{r}}_1) \times \boldsymbol{w}_3 \right).
\end{aligned}$$

Using the vector triple product,

$$\boldsymbol{w}_2^\top \dot{\boldsymbol{w}}_1 = \frac{1}{\|\boldsymbol{w}_3 \times \hat{\boldsymbol{r}}_1\|} \left((\dot{\boldsymbol{w}}_3^\top \boldsymbol{w}_3)(\hat{\boldsymbol{r}}_1^\top \boldsymbol{w}_2) - (\hat{\boldsymbol{r}}_1^\top \boldsymbol{w}_3)(\dot{\boldsymbol{w}}_3^\top \boldsymbol{w}_2) \right).$$

Since $\hat{\boldsymbol{r}}_1^\top \boldsymbol{w}_2 = 0$,

$$\boldsymbol{w}_2^\top \dot{\boldsymbol{w}}_1 = -\frac{(\hat{\boldsymbol{r}}_1^\top \boldsymbol{w}_3)(\dot{\boldsymbol{w}}_3^\top \boldsymbol{w}_2)}{\|\boldsymbol{w}_3 \times \hat{\boldsymbol{r}}_1\|} = \frac{(\hat{\boldsymbol{r}}_1^\top \boldsymbol{w}_3)(\hat{\boldsymbol{r}}_1^\top (\boldsymbol{w}_3 \times \dot{\boldsymbol{w}}_3))}{\|\boldsymbol{w}_3 \times \hat{\boldsymbol{r}}_1\|^2}.$$

Thus, the parallel component is

$$\boldsymbol{\omega}_{w_\parallel} = \frac{(\hat{\boldsymbol{r}}_1^\top \boldsymbol{w}_3)(\hat{\boldsymbol{r}}_1^\top (\boldsymbol{w}_3 \times \dot{\boldsymbol{w}}_3))}{\|\boldsymbol{w}_3 \times \hat{\boldsymbol{r}}_1\|^2} \boldsymbol{w}_3.$$

Combining both components, the desired angular velocity $\boldsymbol{\omega}_w$ is

$$\begin{aligned} \boldsymbol{\omega}_w &= \boldsymbol{w}_3 \times \dot{\boldsymbol{w}}_3 + \frac{(\hat{\boldsymbol{r}}_1^\top \boldsymbol{w}_3)(\hat{\boldsymbol{r}}_1^\top (\boldsymbol{w}_3 \times \dot{\boldsymbol{w}}_3))}{\|\boldsymbol{w}_3 \times \hat{\boldsymbol{r}}_1\|^2} \boldsymbol{w}_3 \\ &= \left[\boldsymbol{I}_3 + \frac{\hat{\boldsymbol{r}}_1^\top \boldsymbol{w}_3}{\|\boldsymbol{w}_3 \times \hat{\boldsymbol{r}}_1\|^2} \boldsymbol{w}_3 \hat{\boldsymbol{r}}_1^\top \right] (\boldsymbol{w}_3 \times \dot{\boldsymbol{w}}_3) . \end{aligned} \tag{D.5}$$

Finally, substituting (D.5) into the expression for $\boldsymbol{\omega}_d$ gives:

$$\boldsymbol{\omega}_d = \boldsymbol{R}_d^\top \left[\boldsymbol{I}_3 + \frac{\hat{\boldsymbol{r}}_1^\top \boldsymbol{w}_3}{\|\boldsymbol{w}_3 \times \hat{\boldsymbol{r}}_1\|^2} \boldsymbol{w}_3 \hat{\boldsymbol{r}}_1^\top \right] (\boldsymbol{w}_3 \times \dot{\boldsymbol{w}}_3) . \tag{D.6}$$

Remark 5 (Time-varying Heading Direction)**.** *The expression for $\boldsymbol{\omega}_d$ in* (D.6) *assumes a constant heading direction $\hat{\boldsymbol{r}}_1$. If $\hat{\boldsymbol{r}}_1$ varies with time, the desired angular velocity becomes*

$$\boldsymbol{\omega}_d = \boldsymbol{R}_d^\top \left(\left[\boldsymbol{I}_3 + \frac{\hat{\boldsymbol{r}}_1^\top \boldsymbol{w}_3}{\|\boldsymbol{w}_3 \times \hat{\boldsymbol{r}}_1\|^2} \boldsymbol{w}_3 \hat{\boldsymbol{r}}_1^\top \right] (\boldsymbol{w}_3 \times \dot{\boldsymbol{w}}_3) + \dot{\boldsymbol{r}}_1^\top (\boldsymbol{w}_3 \times \hat{\boldsymbol{r}}_1) \boldsymbol{w}_3 \right), \tag{D.7}$$

where $\dot{\boldsymbol{r}}_1$ is the time derivative of the heading direction.

D.1 Bounding the Desired Angular Velocity

We now establish an upper bound for $\boldsymbol{\omega}_d$ as given in (D.6). By the sub-multiplicative property of matrix norms,

$$\begin{aligned} \|\boldsymbol{\omega}_d\| &= \left\| \boldsymbol{R}_d^\top \left[\boldsymbol{I}_3 + \frac{\hat{\boldsymbol{r}}_1^\top \boldsymbol{w}_3}{\|\boldsymbol{w}_3 \times \hat{\boldsymbol{r}}_1\|^2} \boldsymbol{w}_3 \hat{\boldsymbol{r}}_1^\top \right] (\boldsymbol{w}_3 \times \dot{\boldsymbol{w}}_3) \right\| \\ &\le \|\boldsymbol{R}_d^\top\| \left\| \boldsymbol{I}_3 + \frac{\hat{\boldsymbol{r}}_1^\top \boldsymbol{w}_3}{\|\boldsymbol{w}_3 \times \hat{\boldsymbol{r}}_1\|^2} \boldsymbol{w}_3 \hat{\boldsymbol{r}}_1^\top \right\| \|\boldsymbol{w}_3 \times \dot{\boldsymbol{w}}_3\|. \end{aligned}$$

Since $\boldsymbol{R}_d$ is a rotation matrix, $\|\boldsymbol{R}_d^\top\| = 1$. Therefore,

$$\|\boldsymbol{\omega}_d\| \le \left\| \boldsymbol{I}_3 + \frac{\hat{\boldsymbol{r}}_1^\top \boldsymbol{w}_3}{\|\boldsymbol{w}_3 \times \hat{\boldsymbol{r}}_1\|^2} \boldsymbol{w}_3 \hat{\boldsymbol{r}}_1^\top \right\| \|\boldsymbol{w}_3 \times \dot{\boldsymbol{w}}_3\|.$$

To bound the first term, observe that for any vectors $\boldsymbol{a}, \boldsymbol{b} \in \mathbb{R}^3$ with $\|\boldsymbol{a}\| = \|\boldsymbol{b}\| = 1$, the matrix $\boldsymbol{a}\boldsymbol{b}^\top$ has operator norm 1. Thus,

$$\begin{aligned}\left\| \boldsymbol{I}_3 + \frac{\hat{\boldsymbol{r}}_1^\top \boldsymbol{w}_3}{\|\boldsymbol{w}_3 \times \hat{\boldsymbol{r}}_1\|^2} \boldsymbol{w}_3 \hat{\boldsymbol{r}}_1^\top \right\|_2 &\leq \|\boldsymbol{I}_3\|_2 + \left| \frac{\hat{\boldsymbol{r}}_1^\top \boldsymbol{w}_3}{\|\boldsymbol{w}_3 \times \hat{\boldsymbol{r}}_1\|^2} \right| \|\boldsymbol{w}_3 \hat{\boldsymbol{r}}_1^\top\|_2 \\ &= 1 + \frac{|\hat{\boldsymbol{r}}_1^\top \boldsymbol{w}_3|}{\|\boldsymbol{w}_3 \times \hat{\boldsymbol{r}}_1\|^2}.\end{aligned}$$

To ensure the denominator is bounded away from zero, assume $\hat{\boldsymbol{r}}_1$ is never parallel to $\boldsymbol{w}_3$, i.e., $|\hat{\boldsymbol{r}}_1^\top \boldsymbol{w}_3| \leq \delta < 1$ for all $t \geq 0$. Since

$$\|\boldsymbol{w}_3 \times \hat{\boldsymbol{r}}_1\|^2 = 1 - (\hat{\boldsymbol{r}}_1^\top \boldsymbol{w}_3)^2 \geq 1 - \delta^2,$$

we obtain the uniform bound

$$\left\| \boldsymbol{I}_3 + \frac{\hat{\boldsymbol{r}}_1^\top \boldsymbol{w}_3}{\|\boldsymbol{w}_3 \times \hat{\boldsymbol{r}}_1\|^2} \boldsymbol{w}_3 \hat{\boldsymbol{r}}_1^\top \right\|_2 \leq 1 + \frac{\delta}{1 - \delta^2}. \tag{D.8}$$

Combining this with the previous inequality, we have

$$\|\boldsymbol{\omega}_d\| \leq \left(1 + \frac{\delta}{1 - \delta^2}\right) \|\boldsymbol{w}_3 \times \dot{\boldsymbol{w}}_3\|.$$

To bound $\|\boldsymbol{w}_3 \times \dot{\boldsymbol{w}}_3\|$, we use the fact that $\|\boldsymbol{w}_3\| = 1$ and the norm of the cross product:

$$\|\boldsymbol{w}_3 \times \dot{\boldsymbol{w}}_3\| = \|\boldsymbol{w}_3\| \|\dot{\boldsymbol{w}}_3\| \sin(\theta) \leq \|\dot{\boldsymbol{w}}_3\| = \|\dot{\hat{\boldsymbol{f}}}_r\|.$$

Thus, we obtain the final bound:

$$\|\boldsymbol{\omega}_d\| \leq \left(1 + \frac{\delta}{1 - \delta^2}\right) \|\dot{\hat{\boldsymbol{f}}}_r\|. \tag{D.9}$$

This shows that the desired angular velocity $\boldsymbol{\omega}_d$ is bounded by a constant factor times the rate of change of the reference force direction $\hat{\boldsymbol{f}}_r$.

The bound in (D.9) can be sharpened by explicitly relating $\dot{\hat{\boldsymbol{f}}}_r$ to the system dynamics. Recall that for any differentiable vector $\boldsymbol{f}_r \neq \boldsymbol{0}$,

$$\dot{\hat{\boldsymbol{f}}}_r = \frac{1}{\|\boldsymbol{f}_r\|} \left(\boldsymbol{I}_3 - \hat{\boldsymbol{f}}_r \hat{\boldsymbol{f}}_r^\top\right) \dot{\boldsymbol{f}}_r, \tag{D.10}$$

where $\boldsymbol{f}_r$ is the reference control force defined in (5.4). This yields

$$\|\dot{\hat{\boldsymbol{f}}}_r\| \leq \frac{\|\dot{\boldsymbol{f}}_r\|}{\|\boldsymbol{f}_r\|}.$$

Assuming $\|\boldsymbol{f}_r\| \geq f_r^{\min} := mg > 0$ for all t, we have

$$\|\dot{\hat{\boldsymbol{f}}}_r\| \leq \frac{\|\dot{\boldsymbol{f}}_r\|}{mg}.$$

Since

$$\dot{\boldsymbol{f}}_r = -\boldsymbol{K}_p \dot{\boldsymbol{e}}_p - \boldsymbol{K}_v \dot{\boldsymbol{v}},$$

and

$$\dot{\boldsymbol{v}} = \frac{1}{m}\left(-\boldsymbol{K}_p \boldsymbol{e}_p - \boldsymbol{K}_v \boldsymbol{v} + \boldsymbol{X} + \boldsymbol{P}_\star^\perp \boldsymbol{R}\boldsymbol{F}_1 \boldsymbol{F}_2^\dagger \boldsymbol{\tau}_r\right),$$

we get

$$\dot{\boldsymbol{f}}_r = \frac{1}{m}\boldsymbol{K}_v \boldsymbol{K}_p \boldsymbol{e}_p + (\frac{1}{m}\boldsymbol{K}_v^2 - \boldsymbol{K}_p)\boldsymbol{v} - \frac{1}{m}\boldsymbol{K}_v \boldsymbol{X} - \frac{1}{m}\boldsymbol{K}_v \boldsymbol{P}_\star^\perp \boldsymbol{R}\boldsymbol{F}_1 \boldsymbol{F}_2^\dagger \boldsymbol{\tau}_r.$$

Therefore, we can bound $\|\dot{\boldsymbol{f}}_r\|$ as follows:

$$\|\dot{\boldsymbol{f}}_r\| \leq \frac{k_v k_p}{m}\|\boldsymbol{e}_p\| + |\frac{k_v^2}{m} - k_p|\|\boldsymbol{v}\| + \frac{k_v}{m}\|\boldsymbol{X}\| + \frac{k_v}{m}\gamma\|\boldsymbol{\tau}_r\|.$$

Substituting into the previous bound, the desired angular velocity satisfies

$$\|\boldsymbol{\omega}_d\| \leq \left(1 + \frac{\delta}{1-\delta^2}\right)\frac{1}{mg}\left(\frac{k_v k_p}{m}\|\boldsymbol{e}_p\| + |\frac{k_v^2}{m} - k_p|\|\boldsymbol{v}\| + \frac{k_v}{m}\|\boldsymbol{X}\| + \frac{k_v}{m}\gamma\|\boldsymbol{\tau}_r\|\right). \tag{D.11}$$

This expression makes explicit how the bound on $\|\boldsymbol{\omega}_d\|$ depends on the system's tracking error dynamics and control gains.

Appendix E

Positive Definiteness Conditions

This appendix presents a rigorous derivation of the conditions required for the positive definiteness of the matrices involved in the stability analysis, as well as the admissible bounds for the parameters c_1 and c_2.

E.1 Positive Definiteness Conditions for Translational Dynamics

We first establish the conditions under which the matrices $\boldsymbol{M}_{11}$, $\boldsymbol{M}_{12}$, and $\boldsymbol{W}_1$ are positive definite. These conditions are derived by applying the Sylvester criterion to 2×2 matrices and are summarized as follows:

- **Matrices $\boldsymbol{M}_{11}$ and $\boldsymbol{M}_{12}$:** Positive definiteness is ensured if and only if

  $$k_p > 0 \quad \text{and} \quad c_1 < \sqrt{m\, k_p}, \tag{E.1}$$

  where k_p denotes the translational proportional gain and m is the mass.

- **Matrix $\boldsymbol{W}_1$:** Positive definiteness is guaranteed if and only if

  $$c_1 < k_v(1 - e_R^{\max}), \qquad c_1 < \frac{4k_p k_v m (e_R^{\max} - 1)^2}{k_v^2 (e_R^{\max} + 1)^2 + 4k_p m (1 - e_R^{\max})}, \tag{E.2}$$

  where k_v is the translational derivative gain and $e_R^{\max}$ is the maximum attitude error.

By consolidating the requirements in (E.1) and (E.2), the admissible range for the parameter c_1 is given by

$$c_1 < \min\left\{ \sqrt{m\, k_p},\ k_v(1 - e_R^{\max}),\ \frac{4k_p k_v m (e_R^{\max} - 1)^2}{k_v^2 (e_R^{\max} + 1)^2 + 4k_p m (1 - e_R^{\max})} \right\}.$$

This condition ensures the positive definiteness of all relevant matrices, thereby guaranteeing the stability properties required for the subsequent analysis.

E.2 Positive Definiteness Conditions for Attitude Dynamics

Similarly, we derive the conditions for the positive definiteness of the matrices $\boldsymbol{M}_{21}$, $\boldsymbol{M}_{22}$, and $\boldsymbol{W}_2$ using the Sylvester criterion. The admissible bounds for the parameter c_2 are summarized below:

- **Matrix $\boldsymbol{M}_{21}$:** Positive definiteness is achieved if and only if

$$k_R > 0 \quad \text{and} \quad c_2 < \sqrt{\lambda_{\min}(\boldsymbol{J})\, k_R}, \tag{E.3}$$

  where k_R is the attitude proportional gain and $\lambda_{\min}(\boldsymbol{J})$ denotes the minimum eigenvalue of the inertia matrix $\boldsymbol{J}$.

- **Matrix $\boldsymbol{M}_{22}$:** Positive definiteness holds if and only if

$$k_R > 0 \quad \text{and} \quad c_2 < \sqrt{\lambda_{\max}(\boldsymbol{J}) k_R \frac{2}{2-\psi}}, \tag{E.4}$$

  where $\lambda_{\max}$ is the maximum eigenvalue of $\boldsymbol{J}$ and ψ is a parameter related to the attitude error.

- **Matrix $\boldsymbol{W}_2$:** Positive definiteness is ensured if and only if

$$\begin{aligned} &c_2 > k_v\, \lambda_{\max}(\boldsymbol{J})\, \alpha\, (mg + k_R \gamma)\,, \\ &c_2 < \frac{k_\omega}{1 + k_v\, \gamma\, \alpha\, (\beta + k_\omega)}, \\ &\det(\boldsymbol{W}_2) > 0, \end{aligned} \tag{E.5}$$

  where k_ω is the derivative gain for the attitude dynamics, α, β, and γ are auxiliary parameters expressed in (6.38) and (6.26), and g is the gravitational acceleration.

Before combining the conditions in (E.3), (E.4), and (E.5), we analyze the values of c_2 for which the determinant of $\boldsymbol{W}_2$ is positive. This leads to the following second-order inequalities:

$$-A\, c_2^2 + B\, c_2 - C > 0, \tag{E.6}$$

where

$$A = \frac{1}{4}\Big(\frac{k_\omega}{\lambda_{\min}(\boldsymbol{J})} + k_v \gamma \alpha (mg + k_R \gamma)\Big)^2 + \frac{k_R}{\lambda_{\max}(\boldsymbol{J})}\Big[1 + k_v \gamma \alpha (\beta + k_\omega)\Big], \tag{E.7}$$

$$\begin{aligned} B = {} & k_R k_v \alpha (mg + k_R \gamma)\Big[1 + k_v \gamma \alpha (\beta + k_\omega)\Big] + \frac{k_R k_\omega}{\lambda_{\max}(\boldsymbol{J})} \\ & - \frac{1}{2}\Big(\frac{k_\omega}{\lambda_{\min}(\boldsymbol{J})} + k_v \gamma \alpha (mg + k_R \gamma)\Big)\big[k_R k_v \gamma \alpha (\beta + k_\omega)\big], \end{aligned} \tag{E.8}$$

$$C = k_R k_v \alpha \Big(\tfrac{1}{4} k_R k_v \gamma^2 \alpha (\beta + k_\omega)^2 + k_\omega (mg + k_R \gamma)\Big). \tag{E.9}$$

Since $A > 0$, the parabola in (E.6) opens downward with respect to the variable c_2. Therefore, the condition for the determinant to be positive is satisfied if and only if c_2 lies strictly between the roots of the associated quadratic equation:

$$c_{2,-} = \frac{B - \sqrt{\Delta}}{2A}, \qquad c_{2,+} = \frac{B + \sqrt{\Delta}}{2A}, \qquad \Delta = B^2 - 4AC > 0.$$

If $B > 0$, then both $c_{2,-}$ and $c_{2,+}$ are positive, and (E.6) holds if and only if

$$c_2 \in \left(c_{2,-},\, c_{2,+}\right). \tag{E.10}$$

Remark 6. *If $\Delta \leq 0$, the quadratic polynomial in* (E.6) *is nonpositive for all c_2, and thus the matrix $\boldsymbol{W}_2$ cannot be positive definite for the given parameters. Furthermore, even if $\Delta > 0$, it is necessary that $B > 0$ to ensure that both roots $c_{2,-}$ and $c_{2,+}$ are positive, which is a prerequisite for the existence of a positive admissible interval for c_2. Therefore, both conditions must be verified to guarantee the positive definiteness of $\boldsymbol{W}_2$.*

Put together (E.3), (E.5) and (E.10), the conditions for the positive definiteness of the matrices $\boldsymbol{M}_{21}$, $\boldsymbol{M}_{22}$, and $\boldsymbol{W}_2$ can be summarized as follows:

$$\begin{aligned} c_2 &< \min\left\{\sqrt{\lambda_{\min}(\boldsymbol{J})\, k_R},\ \frac{k_\omega}{1 + k_v \gamma \alpha(\beta + k_\omega)},\ c_{2,+}\right\}, \\ c_2 &> \max\left\{k_v \lambda_{\max}(\boldsymbol{J}) \alpha (mg + k_R \gamma)\,,\ c_{2,-}\right\}, \end{aligned}$$

where we have noticed that $\sqrt{\lambda_{\min}(\boldsymbol{J})\, k_R}$ is always strictly less than $\sqrt{\lambda_{\max}(\boldsymbol{J}) k_R \frac{2}{2-\psi}}$ for any admissible value of k_R.

Bibliography

[1] V. G. Adîr, A. M. Stoica, and J. F. Whidborne. “Modelling and Control of a Star–Shaped Octorotor”. In: *Applied Mechanics and Materials* 325 (2013), pp. 994–998. DOI: 10.4028/www.scientific.net/AMM.325-326.994.

[2] Karen Bodie et al. “Active Interaction Force Control for Contact-Based Inspection with a Fully Actuated Aerial Vehicle”. In: *IEEE Transactions on Robotics* 37.3 (2021), pp. 709–722. DOI: 10.1109/TRO.2020.3036623.

[3] Samir Bouabdallah, André Noth, and Roland Siegwart. “PID vs LQ Control Techniques Applied to an Indoor Micro Quadrotor”. In: *Proc. IEEE/RSJ Int. Conf. on Intelligent Robots and Systems (IROS)*. Vol. 3. Sendai, Japan, 2004, pp. 2451–2456. DOI: 10.1109/IROS.2004.1389776.

[4] D. Brescianini and R. D’Andrea. “Design, Modeling and Control of an Omni–Directional Aerial Vehicle”. In: *Proc. IEEE Int. Conf. on Robotics and Automation (ICRA)*. Stockholm, Sweden, 2016, pp. 3261–3266. DOI: 10.1109/ICRA.2016.7487497.

[5] Guang-Xun Du et al. “Controllability Analysis for Multirotor Helicopter Rotor Degradation and Failure”. In: *Journal of Guidance, Control, and Dynamics* 38.5 (2015), pp. 978–985. DOI: 10.2514/1.G000731.

[6] Vishakh Duggal et al. “Plantation Monitoring and Yield Estimation Using Autonomous Quadcopter for Precision Agriculture”. In: *Proc. 2016 IEEE Int. Conf. on Robotics and Automation (ICRA)*. Stockholm, Sweden, 2016, pp. 5121–5127. DOI: 10.1109/ICRA.2016.7487716.

[7] Zixuan Fang and Andrey V. Savkin. “Strategies for Optimized UAV Surveillance in Various Tasks and Scenarios: A Review”. In: *Drones* 8.5 (2024), p. 193. DOI: 10.3390/drones8050193.

[8] Philipp Foehn and Davide Scaramuzza. “Onboard State Dependent LQR for Agile Quadrotors”. In: *Proc. IEEE Int. Conf. on Robotics and Automation (ICRA)*. Brisbane, Australia, 2018, pp. 6566–6572. DOI: 10.1109/ICRA.2018.8460885.

[9] C. Gabellieri and A. Franchi. *Control for UAVs 2023–2024*. Lecture notes, University of Twente. 2024.

[10] Sajjad A. Ghauri et al. “A Review of Multi-UAV Task Allocation Algorithms for a Search and Rescue Scenario”. In: *Journal of Sensor and Actuator Networks* 13.5 (2024), p. 47. DOI: 10.3390/jsan13050047.

[11] Juan I. Giribet, Ricardo S. Sanchez-Pena, and Alejandro S. Ghersin. “Analysis and Design of a Tilted Rotor Hexacopter for Fault Tolerance”. In: *IEEE Transactions on Aerospace and Electronic Systems* 52.4 (2016), pp. 1555–1567. DOI: `10.1109/TAES.2016.140885`.

[12] Anne Goodchild and Jordan Toy. “Delivery by Drone: An Evaluation of Unmanned Aerial Vehicle Technology in Reducing CO2 Emissions in the Delivery Service Industry”. In: *Transportation Research Part D: Transport and Environment* 61 (2018), pp. 58–67. DOI: `10.1016/j.trd.2017.02.017`.

[13] Xiaofeng Guo et al. *Aerial Interaction with Tactile Sensing*. 2023. arXiv: `2310.00142 [cs.RO]`. URL: `https://arxiv.org/abs/2310.00142`.

[14] S. J. Haddadi and P. Zarafshan. “Design and Fabrication of an Autonomous Octorotor Flying Robot”. In: *Proc. 3rd RSI Int. Conf. on Robotics and Mechatronics (ICRoM)*. Tehran, Iran, 2015, pp. 702–707. DOI: `10.1109/ICRoM.2015.7367868`.

[15] Mahmoud Hamandi et al. “Design of Multirotor Aerial Vehicles: A Taxonomy Based on Input Allocation”. In: *The International Journal of Robotics Research* 40.8-9 (2021), pp. 1015–1044. DOI: `10.1177/02783649211025998`.

[16] Mahmoud Hamandi et al. “Omni-Plus-Seven (O7+): An Omnidirectional Aerial Prototype with a Minimal Number of Unidirectional Thrusters”. In: *Proceedings of the 2020 International Conference on Unmanned Aircraft Systems (ICUAS)*. Athens, Greece, 2020, pp. 754–761. DOI: `10.1109/ICUAS.2020.9213950`.

[17] A. Isidori. *Nonlinear Control Systems*. Springer London, 1995. ISBN: 9783540199168.

[18] A. Isidori and A. Cristofaro. *Robust Control*. Lecture notes, Sapienza University of Rome. n.d.

[19] Mina Kamel et al. “Voliro: An Omnidirectional Hexacopter with Tiltable Rotors”. In: *IEEE Robotics and Automation Magazine* 25.3 (2018), pp. 34–45. DOI: `10.1109/MRA.2018.2866758`.

[20] H. K. Khalil. *Nonlinear Systems*. Prentice Hall, 2002. ISBN: 9780130673893.

[21] Won Jun Kim et al. “Design and Control of a Central-Rotor Type Pentacopter Capable of Wall Contact and Surface Traversal”. In: *International Journal of Advanced Robotic Systems* 21.5 (2024), pp. 1–18. DOI: `10.1177/17298806241278167`.

[22] T. Lee, M. Leok, and N. H. McClamroch. “Geometric Tracking Control of a Quadrotor UAV on SE(3)”. In: *Proceedings of the 49th IEEE Conference on Decision and Control*. Atlanta, GA, USA, 2010, pp. 5420–5425. DOI: `10.1109/CDC.2010.5717652`.

[23] Kevin M. Lynch and Frank C. Park. *Modern Robotics: Mechanics, Planning, and Control*. Cambridge University Press, 2017. ISBN: 9781107156302.

[24] Mingyang Lyu et al. “Unmanned Aerial Vehicles for Search and Rescue: A Survey”. In: *Remote Sensing* 15.13 (2023), p. 3266. DOI: `10.3390/rs15133266`.

[25] Daniel Mellinger et al. “Cooperative Grasping and Transport Using Multiple Quadrotors”. In: *Distributed Autonomous Robotic Systems*. 2013, pp. 545–558. ISBN: 978-3-642-32722-3. DOI: `10.1007/978-3-642-32723-0_39`.

[26] G. Michieletto, M. Ryll, and A. Franchi. “Control of Statically Hoverable Multi-Rotor Aerial Vehicles and Application to Rotor-Failure Robustness for Hexarotors”. In: *2017 IEEE International Conference on Robotics and Automation (ICRA)*. Singapore, Singapore, 2017, pp. 2747–2752. DOI: `10.1109/ICRA.2017.7989320`.

[27] G. Michieletto, M. Ryll, and A. Franchi. “Fundamental Actuation Properties of Multirotors: Force–Moment Decoupling and Fail–Safe Robustness”. In: *IEEE Transactions on Robotics* 34.3 (2018), pp. 702–715.

[28] Almodather Mohamed and Mohammed Mohamed. “Unmanned Aerial Vehicles in Last-Mile Parcel Delivery: A State-of-the-Art Review”. In: *Drones* 9.6 (2025), p. 413. DOI: `10.3390/drones9060413`.

[29] Richard M. Murray, Shankar Sastry, and Zexiang Li. *A Mathematical Introduction to Robotic Manipulation*. Boca Raton, FL: CRC Press, 1994.

[30] G. Oriolo. *Autonomous and Mobile Robotics*. Lecture notes, Sapienza University of Rome. 2024.

[31] Jongho Park and Youdan Kim. “Horizontal–Vertical Guidance of Quadrotor for Obstacle Shape Mapping”. In: *IEEE Transactions on Aerospace and Electronic Systems* 52.6 (2016), pp. 3024–3035. DOI: `10.1109/TAES.2016.150727`.

[32] S. Park et al. “Design, Modeling and Control of Omni–Directional Aerial Robot”. In: *Proc. IEEE/RSJ Int. Conf. on Intelligent Robots and Systems (IROS)*. Daejeon, South Korea, 2016, pp. 1570–1575. DOI: `10.1109/IROS.2016.7759254`.

[33] Lukman Rabiu and Ahmad Ahmad. “Unmanned Aerial Vehicle Photogrammetric Products Accuracy Assessment: A Review”. In: *International Archives of the Photogrammetry, Remote Sensing and Spatial Information Sciences* XLVIII-4/W6-2022 (2023), pp. 279–288. DOI: `10.5194/isprs-archives-XLVIII-4-W6-2022-279-2023`.

[34] S. Rajappa et al. “Modeling, Control and Design Optimization for a Fully-actuated Hexarotor Aerial Vehicle with Tilted Propellers”. In: *2015 IEEE International Conference on Robotics and Automation (ICRA)*. Seattle, WA, USA, 2015, pp. 4006–4013. DOI: `10.1109/ICRA.2015.7139759`.

[35] Fabio Ruggiero, Vincenzo Lippiello, and Aníbal Ollero. “Aerial Manipulation: A Literature Review”. In: *IEEE Robotics and Automation Letters* 3.3 (2018), pp. 1957–1964. DOI: `10.1109/LRA.2018.2808541`.

[36] Hazim Shakhatreh et al. “Unmanned Aerial Vehicles (UAVs): A Survey on Civil Applications and Key Research Challenges”. In: *IEEE Access* 7 (2019), pp. 48572–48634. DOI: `10.1109/ACCESS.2019.2909530`.

[37] B. Siciliano et al. *Robotics: Modelling, Planning and Control*. Springer London, 2010. ISBN: 9781846286414.

[38] Riccardo Spica et al. “Aerial Grasping of a Moving Target with a Quadrotor UAV”. In: *Proceedings of the 2012 IEEE/RSJ International Conference on Intelligent Robots and Systems (IROS)*. Vilamoura, Portugal, 2012, pp. 4985–4992. ISBN: 978-1-4673-1737-5. DOI: `10.1109/IROS.2012.6385771`.

[39] M. Tognon and A. Franchi. “Omnidirectional Aerial Vehicles with Unidirectional Thrusters: Theory, Optimal Design, and Control”. In: *IEEE Robotics and Automation Letters* 3.3 (2018), pp. 2277–2282. DOI: `10.1109/LRA.2018.2802544`.

[40] Dimosthenis C. Tsouros, Stamatia Bibi, and Panagiotis G. Sarigiannidis. “A Review on UAV-Based Applications for Precision Agriculture”. In: *Information* 10.11 (2019), p. 349. DOI: `10.3390/info10110349`.

[41] Samuel Ubellacker et al. “High-Speed Aerial Grasping Using a Soft Drone with Onboard Perception”. In: *npj Robotics* 2 (2024). DOI: `10.1038/s44182-024-00012-1`.

[42] M. Vendittelli. *Modeling and Control of Multi-Rotor UAVs.* Lecture notes, Sapienza University of Rome. 2024.

[43] Sonia Waharte and Niki Trigoni. “Supporting Search and Rescue Operations with UAVs”. In: *Proc. Int. Conf. on Emerging Security Technologies.* 2010, pp. 142–147. DOI: `10.1109/EST.2010.31`.